Title
Developing Nanomaterial Platforms for Gene Delivery and Transgene-Free Plant Genetic Engineering

Author
Demirer, Gozde S

Publication Date
2020

Developing Nanomaterial Platforms for Gene Delivery and Transgene-Free Plant Genetic Engineering

By

Gozde S Demirer

A dissertation submitted in partial satisfaction of the
requirements for the degree of
Doctor of Philosophy
in
Chemical Engineering
in the
Graduate Division
of the
University of California, Berkeley

Committee in charge:

Professor Markita P Landry, Chair
Professor David Schaffer
Professor Wenjun Zhang
Professor Brian Staskawicz

Spring 2020

Abstract

Developing Nanomaterial Platforms for Gene Delivery and Transgene-Free Plant Genetic Engineering

by

Gozde S Demirer

Doctor of Philosophy in Chemical Engineering
University of California, Berkeley
Professor Markita P Landry, Chair

Plant biotechnology is an essential component of agricultural engineering, small molecule synthesis, and bioenergy efforts. Maximizing the throughput of producing and testing genetically engineered plants is important for both academic research and the agro-industry, and requires a toolset that is (i) plant species-independent, and (ii) capable of high performance despite the physical barriers presented in intact plant tissues, such as the plant cell wall. Currently used plant biotic delivery tools limit the range of plant species that can be transformed, and in the case of biolistic delivery, exhibit low transformation efficiencies and tissue damage due to the use of high force. Furthermore, both methods yield uncontrolled and random transgene integration into the plant nuclear genome, which then elicits strict genetically modified organism (GMO) regulatory purview and public concern for consumption. To-date, there has yet to be a plant transformation method that enables high-efficiency gene delivery, without transgene integration, in a plant species-independent manner.

I have recently shown it is possible to introduce DNA and RNA into intact plant cells without external force with engineered nanomaterials that are below the plant cell wall size-exclusion limit of ~20 nm. Among these nanomaterials, carbon nanotubes (CNTs) possess several optimal criteria for gene delivery into intact plants: high aspect ratio, exceptional tensile strength, biocompatibility, and biomolecular cargo protection from cellular degradation. In this dissertation, I describe a CNT-based gene delivery platform which can efficiently deliver plasmid or linear DNA into both model and agriculturally-relevant crop plants, without mechanical aid, in a non-toxic and non-integrating manner. Notably, this combination of features is not attainable with existing plant transformation approaches. CNT gene delivery enables strong transient expression of reporter and functional proteins without DNA integration in dicot species *Nicotiana benthamiana*

(model), *Eruca sativa* (arugula, non-model), *Gossypium hirsutum* (cotton, non-model, hard to transform), and in monocot species *Triticum aestivum* (wheat, non-model). This technology can be used to deliver CRISPR/Cas9 gene editing plasmids as a method to achieve stable genome editing in plants while circumventing GMO labeling, through the transient expression of a nuclease protein and guide RNA in model and crop plants.

Moreover, CNTs with different surface chemistries are developed and used to deliver other important biomolecules, such as small interfering RNAs, for efficient DNA-free gene knock-down applications in intact plants. In a separate study, I systematically investigated the effect of certain nanomaterial parameters (shape, size, aspect ratio, stiffness, and cargo attachment loci) on plant cell internalization, and gene silencing pathways and efficiencies using easily programmable DNA nanostructures as nanomaterial scaffolds. Additionally, in this dissertation, I demonstrate how these nanomaterials not only facilitate biomolecule transport into plant cells but also protect polynucleotides from nuclease degradation inside the cells, which increase their efficiencies and permit the usage of a lower cargo dose.

CNT-based plant transformation is a breakthrough for biotechnology applications where transient protein expression without gene integration is desired, such as the delivery of CRISPR/Cas9 cargoes to achieve permanent genome editing. Furthermore, CNT-based gene delivery is rapid, cost-effective, amenable to multiplexing and can aid high-throughput screening in mature plants. This enables (i) rapid identification of genotypes that result in desired phenotypes, (ii) mapping and optimization of plant biosynthetic pathways, and (iii) maximization of plant-mediated therapeutics synthesis. Therefore, nanomaterials promise to overcome the long-standing plant genome engineering limitations in a species-independent and non-integrating manner and can newly enable variety of different life sciences applications.

Table of Contents

List of Figures

List of Tables

Acknowledgements

I thank my advisor Prof. Markita P. Landry for helping me get to this point in my academic career. I am especially grateful for her continuous support of my interest in plant gene delivery technologies, and her encouragement of my creativity and independency in the pursuit of my research projects. Her endless positivity and confidence in me enabled me to seek and obtain awards and positions that without her encouragement I would otherwise not consider applying to. I would also like to thank Profs. Brian Staskawicz, David Schaffer and Wenjun Zhang for being on my dissertation committee and for all their career and research-related advice over the past years. In addition, I owe it to Prof. Seda Kizilel for giving me a chance to work in her lab as an inexperienced undergraduate student, and for introducing me to the field of bionanotechnology.

The members of the Landry lab, both past and present, have been a great source of help academically as well as personally. Chapter 2 of this dissertation presents parts from a previously published work, originally cited as: Demirer G.S., Zhang H., Matos J.L., Goh N.S., Cunningham F.J. *et al.* High aspect ratio nanomaterials enable delivery of functional genetic material without DNA integration in mature plants. *Nature Nanotechnology* 14 (5), 2019, 456-464. Similarly, Chapter 3 presents sections from the previously published work, originally cited as: Demirer G.S., Zhang H., Goh N.S., Pinals R.L, Chang R., Landry M.P. Carbon Nanocarriers Deliver siRNA to Intact Plant Cells for Efficient Gene Knockdown. *Science Advances*, 2020 (In press, currently can be found in bioRxiv). Lastly, Chapter 4 discusses the previously published work, originally cited as: Demirer G.S.*, Zhang H.*, Zhang H., Ye T., Goh N.S. *et al.* DNA nanostructures coordinate gene silencing in mature plants. *Proceedings of the National Academy of Sciences* 116 (15), 2019, 7543-7548. I am grateful to all authors of these publications and collaborators for their help with experiments and reviewing the manuscripts. I also thank the undergraduate students, Roger Chang and Abhishek Aditham, for their help in lab. Abhishek has been very reliable over the past couple of years, and progress would have been much slower without his hard work and diligence.

Lastly, I would like to thank all my family members and friends, who are both across the world in Turkey and here in the United States for their continuing love, support and understanding. My PhD and any other accomplishment would not have been possible without them and their endless support.

CHAPTER 1. INTRODUCTION

1.1. Traditional Plant Breeding for Food Security

World Food Summit defined food security as: "Food security exists when all people, at all times, have physical, social and economic access to sufficient, safe and nutritious food which meets their dietary needs and food preferences for an active and healthy life"[1]. According to this definition, over centuries, the world faced many threats to food security and so far plant breeding has provided a means for a sustainable agriculture. Plant breeding has been utilized since ancient times (about 5,000 years ago) to domesticate crops and to improve the quality of nutrition and crop yields. In those ancient times, our ancestors did not have the knowledge of genetics, chromosomes or molecular techniques that we use nowadays to breed improved plants. Before modern plant breeding, farmers used to simply select the crops with desirable traits for propagation. However, modern plant breeding takes advantage of many approaches of molecular biology to create genetic variations, select desirable traits, control plant pollination, and to improve seed multiplication.

To demonstrate the immense positive impact of plant breeding on food security, we can take a look at the 1960s. 1960s was a decade of despair with regards to our ability to deal with the food-population imbalance, as global population growth rates were accelerating rapidly[2]. To address this problem, International Rice Research Institute (IRRI) was founded in 1960 in Philippines to create improved varieties of rice, which is the most widely consumed staple food globally, especially in Asia and Africa. After 6 years of very involved plant breeding efforts, IRRI released a high-yielding semi-dwarf rice variety that is called IR8. IR8 had significantly improved yield compared to previous rice varieties and was resistant to the disease GLH - caused by green leafhoppers which was a big problem in the area where IR8 was discovered. IRRI continued breeding rice over decades and identified varieties that are resistant to even more diseases, such as bacterial blight and blast. These developments were named as "Green revolution" and resulted in the increase of rice production from 200 million tons in 1961 to 1500 million tons in 2002, which triggered the rice price reduction from 300 to 75 dollars per ton[2]. In the meantime, there was not a significant increase in the rice farm global footprint to provide this production increase, as otherwise predicted before the green revolution.

Green revolution and improved rice varieties developed by IRRI through breeding prevented famine in numerous countries during the period of 1960-2000. In 2002, the gene that is responsible for the semi-dwarf phenotype in rice was identified, and it codes for an enzyme gibberellin 20-oxidase that is crucial for the synthesis of plant hormone gibberellin[3]. Remarkably, the semi-dwarf rice phenotype and its yield and disease resistance benefits can be obtained through a *single* nucleotide polymorphism in the gibberellin 20-oxidase gene, which results in the amino acid change from Leucine to Phenylalanine that makes this gene inactive[4]. In summary, advances in plant breeding have been revolutionary to prevent famines and provide food security. However, breeding requires massive time and labor input, in addition to being genetically non-targeted, and resulting in potential plant fitness reduction under certain circumstances. Additionally, breeding to obtain plants with preferred genotypes requires crossing and selection of multiple plant generations, which disallows introduction of traits that are not currently existing in the species. Furthermore, breeding is a coarse method, since crossing two plants results in the transfer of multiple genes aside from the gene of interest. Therefore, a technique that broadly enables targeted horizontal gene transfer to obtain a stable or transient change in plant gene expression stands to greatly benefit the agricultural industry.

1.2. Plant Genetic Engineering and Genome Editing

Today, 1 in 9 people is undernourished around the globe, and every day the world population keeps increasing by more than 180,000 people. However, the farmland is highly limited and there are significant adverse effects of climate change on our global agricultural production levels. It is estimated that there will be approximately 9.7 billion people on Earth by 2050, and even if we neglect the negative effects of climate change, we must still increase our food production by 70% to meet global food security needs. Given the urgency of our need for significant crop improvement, targeted and fast approaches combined with the plant breeding technologies may prove useful to achieve food security. Plant genetic engineering is a precise, targeted and rapid technology that has immense potential to provide food security for a growing global population under changing climate. Genetic engineering of plants can be employed to create crops that have higher yields[5] and nutritional value[6], and are resistant to biotic and abiotic stresses such as herbicides[7], diseases[8], drought[9], and high temperature[10]. Engineered plants can also improve biosynthesis of valuable products, such as therapeutics[11] and recombinant proteins[12], and enable clean energy production from non-food plant biomass[13].

Genetic engineering refers broadly to manipulating a cell's genome and gene expression profile. Techniques for genetic engineering may cause recombinant protein expression, up or down regulation of a gene, permanent gene knockout, targeted mutations in the host gene, or insertion of large foreign DNA segments into the host genome. Modifications may be transient or permanent (*i.e.* may or may not cause heritable transgene integration) and involve many types of biomolecules - most commonly RNA, DNA, and proteins which are sometimes taken up passively by cells, but often require enhanced delivery techniques such as gene gun, microinjection, electroporation, sonoporation, nanoparticle-assisted delivery, and engineered bacteria or viruses. In plants, current genetic engineering techniques cause transgene integration, or are limited to *in vitro* systems such as plant protoplasts and calli.

Nuclease-enabled genome editing refers to techniques where genes are removed or changed with engineered nucleases, a class of enzymes that perform targeted double-stranded breaks (DSBs) at specific locations in the host genome. When nucleases perform DSBs, the cell undergoes homology-directed repair (HDR) or non-homologous end-joining (NHEJ) to repair the break. NHEJ is a random, error-prone repair process that involves realignment of a few bases such that the high error frequency provides a simplistic pathway for gene knockout. HDR is a non-random repair process requiring large stretches of sequence homology, allowing for precise edits by introducing customized homologous recombination sequences for gene knockout, knock-in, and targeted mutations. Prominent tools in genome editing are zinc finger nucleases (ZFNs), transcription activator-like effector nucleases (TALENs), and CRISPR (clustered regularly interspaced short palindromic repeat)-Cas (CRISPR associated) systems.

In the 1990s, ZFNs became the first nuclease system engineered for selectable genome editing in bacteria[14]. TALEN and CRISPR-Cas genome editing systems were developed for bacteria and eukaryotes more recently, around 2009 and 2012, respectively[15,16]. Composed of protein complexes containing a DNA-binding domain and a DNA-cleaving domain, ZFNs and TALENs rely on protein/DNA recognition to induce endogenous DNA repair. CRISPR-Cas systems are composed of a nuclease protein (Cas) and a guide RNA (gRNA) with sequence homology to the genomic target, and therefore rely on the formation of a ribonucleoprotein (RNP) complex to induce HDR or NHEJ. While all three systems have their drawbacks, CRISPR-Cas has revolutionized the field of genome editing owing to its relatively superior simplicity, efficiency, and ability to perform multiplex genome editing (*i.e.* simultaneous editing of different genes *via* codelivery of several gRNAs) over ZFNs and TALENs.

1.3. Current Cargo Delivery Methods for Plant Genetic Engineering

Genetic engineering has recently seen major advances in animal systems, though progress has lagged in plants. Broadly, modern genetic transformation of plants entails two major steps: genetic cargo delivery and regeneration of the transformed plant, the difficulty of the latter being highly dependent on what delivery method is used and whether stable or transient transformation is desired. Generating transgenic plants inevitably involves regeneration protocols, compared to transient transformations which mainly serve as a rapid way to assay genotype-phenotype relationships and do not require regenerative techniques. The challenge of gene delivery to plants is attributed to the presence of the multilayered and rigid plant cell wall, otherwise absent in animal cells, poses an additional physical barrier for intracellular delivery of biomolecules and is one of the key reasons for the slower implementation and employment of genetic engineering tools to plants[17]. Compared to gene and protein delivery methods developed for animal systems, significantly fewer methods exist for efficient biomolecule delivery to plants.

Amongst conventional plant biomolecule delivery approaches, *Agrobacterium*-mediated and biolistic particle delivery are the two most established and preferred tools for plant genetic transformations (Fig. 1). *Agrobacterium tumefaciens* is a soil bacterium that infects a wide range of dicotyledonous plants (dicots), causing crown gall disease. The formation of a gall on the host plant is achieved *via* the stable transfer, integration, and expression of bacterial DNA in infected plants. Engineering of the *Agrobacterium* plasmid by substitution of the gall-inducing virulence genes with genes of interest confers the ability of *Agrobacterium* to transform the host plant. For this reason, *Agrobacterium* has been harnessed as a tool for plant genetic transformation since its discovery in early 1980s[18].

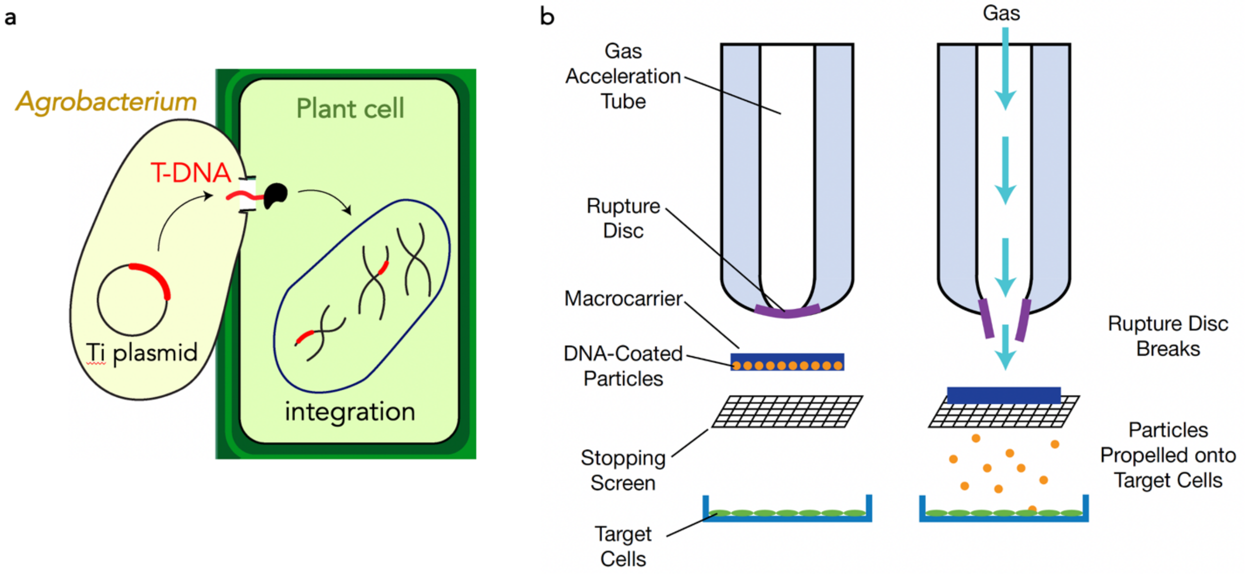

Figure 1. Conventional plant biomolecule delivery approaches.

a, *Agrobacterium*-mediated DNA delivery into intact plant cells and random T-DNA integration into the plant nuclear genome. **b,** Gene gun-mediated biolistic DNA delivery into *ex vivo* plant cells, calli or embryo in a petri dish.

Genetic transformation occurs through a process involving T-DNA (transfer DNA) export, targeting, and insertion into the plant nuclear genome (Fig. 1a). The export of T-DNA from the bacterium to the plant cell is facilitated by the activity of virulence genes present in the tumor inducing-plasmid of *Agrobacterium* but are not themselves transferred. These virulence genes are expressed in the presence of phenolic inducers such as acetosyringone produced by wounded plant cells. *Agrobacterium* attaches to plant cells, where border sequences on either side of the T-DNA (a single-stranded copy of the T-DNA sequence) are cleaved. The T-DNA is then carried by a transporter with a nuclear localization sequence and integrated into the plant nuclear genome. Integration occurs at random positions in the genome *via* non-homologous recombination (NHR), a repair pathway for double-stranded breaks in DNA.

A form of biolistic particle delivery (also called particle bombardment), the gene gun is a physical method that is commonly applied for plant genetic transformations. Developed in 1982 by Sanford *et al.*[19], the process involves gold or tungsten microparticles (or microcarriers) coated with genetic cargo that are accelerated by pressurized helium (He) gas into plant cells, rupturing cell walls and membranes (Fig. 1b). The gene gun consists of three main parts: a rupture disk, macrocarrier (holding microcarrier particles), and stopping screen. The rupture disk is a membrane designed to burst at a critical pressure of He gas. When He gas is accelerated to the desired pressure, the rupture disk bursts, creating a shock wave that propels the macrocarrier towards the plant cells. The macrocarrier's momentum is stopped by the stopping screen, which allows genetic cargo-loaded microcarriers to pass and enter the plant cells. Unlike *Agrobacterium*-mediated transformation, biolistic delivery can result in transformation of the nuclear, plastid, or mitochondrial genomes due to the non-specific localization of genetic cargo in plant cells. Consequently, significantly more DNA needs to be delivered with biolistic delivery than *Agrobacterium*-mediated delivery when targeting the nuclear genome.

While most studies concern DNA plasmid delivery to plants, recent work has broadened delivery attempts to RNA interference (RNAi) cargoes and proteins as well. Most notably, Cas9 protein and single-guide RNA (sgRNA) can be delivered as a protein/RNA complex (ribonucleoprotein, RNP) with polyethylene-glycol (PEG)-mediated[20] and biolistic particle delivery[21], whereby the same complex can also be delivered as an expression vector with *Agrobacterium*[22] and viruses[23], advancing the RNP's utility in plant biotechnology applications.

Current biomolecule delivery methods to plants experience challenges that hinder their scope of use. Methods such as electroporation, biolistics, *Agrobacterium*-mediated delivery, or cationic delivery typically target immature plant tissue (protoplasts, calli, meristems, or embryos). The targeting of immature plant tissues requires tissue culture to generate genetically modified progeny plants post-delivery, if stably transformed plants are desired. Regeneration can be time-consuming, challenging, and efficient protocols have only been developed for a narrow range of plant species. Furthermore, regeneration from transformed cells may lead to somaclonal and phenotypical variations[24]. Biolistic particle delivery involves micrometer-sized carriers accelerated towards tissue at high speeds, circumventing the cell wall *via* mechanical force, but often damaging portions of target tissue in the process. *Agrobacterium*-mediated delivery is subject to orthogonal challenges, the largest of which being that *Agrobacterium* displays narrow host and tissue specificity, even between specific cultivars of the same species[25]. *Agrobacterium* generally experiences lower transformation efficiency for both delivery and regeneration in monocotyledonous plants (monocots) over dicotyledonous plants (dicots), which limits its usefulness as a platform tool. Additionally, *Agrobacterium* yields random DNA integration, which can cause disruption of important genes, or insertion into sections of the genome with poor or unstable expression[26]. Random DNA integration, however, can be prevented by utilizing magnifection with non-integrating viruses[27], or by using a plasmid deficient in T-DNA insertion[28].

In sum, plant genetic engineering progress has lagged behind compared to animal systems; conventional methods of biomolecule delivery to plants remain challenged by intracellular transport through cell walls, and in turn limit plant genetic transformation efficacy. Traditional delivery techniques circumvent the cell wall in two ways: using methods that enable gene editing reagents to traverse the cell wall (*Agrobacterium* and biolistics) or methods that involve cell wall removal. The former procedures can only carry certain cargo types to a restricted host range of plant species or may damage the target tissue. Methods involving protoplasts require regeneration and progeny segregation to obtain stably transformed entities, protocols to which a limited range of plant species are amenable. To date, plant biotechnology lacks a method that allows passive delivery of diverse biomolecules into a broad range of plant phenotypes and species without the aid of external force and without causing tissue damage. I posit nanotechnology as a key driver in the creation of a transformational tool to address delivery challenges and enhance the utility of plant genetic engineering (Fig. 2).

1.4. Nanoparticle-Mediated Biomolecule Delivery to Plants

1.4.1. Nanoparticle-plant interactions

To date, most literature on nanoparticle (NP)-plant systems focuses on plant-based metallic nanomaterial synthesis[29], agrochemical delivery[30], and NP uptake showing both valuable[31] and deleterious effects[32] on plant growth. Dicot and monocot plants exhibit variable degrees of direct uptake of many NP types, including mesoporous silica NPs (MSNs)[33], carbon nanotubes (CNTs)[34], quantum dots[35], and metal/metal oxide NPs[36]. Once uptaken, certain types of NPs exhibit phytotoxicity *via* vascular blockage, oxidative stress, or DNA structural damage[32]. Conversely, certain NPs have been shown to improve root and/or leaf growth and chloroplast production[31]. Tradeoffs between phytotoxicity and growth enhancement as a function of species, growth conditions, NP properties, and dosage are not well-understood and call for more studies with a focus on nanoparticle physical and chemical properties. The research to close this knowledge gap in physiological response to NP properties and plant uptake will need to be performed in parallel to efforts for enhancing plant science using engineered nanomaterials, as the nanorevolution in targeted delivery to animals suggests tremendous potential for analogous progress in plants.

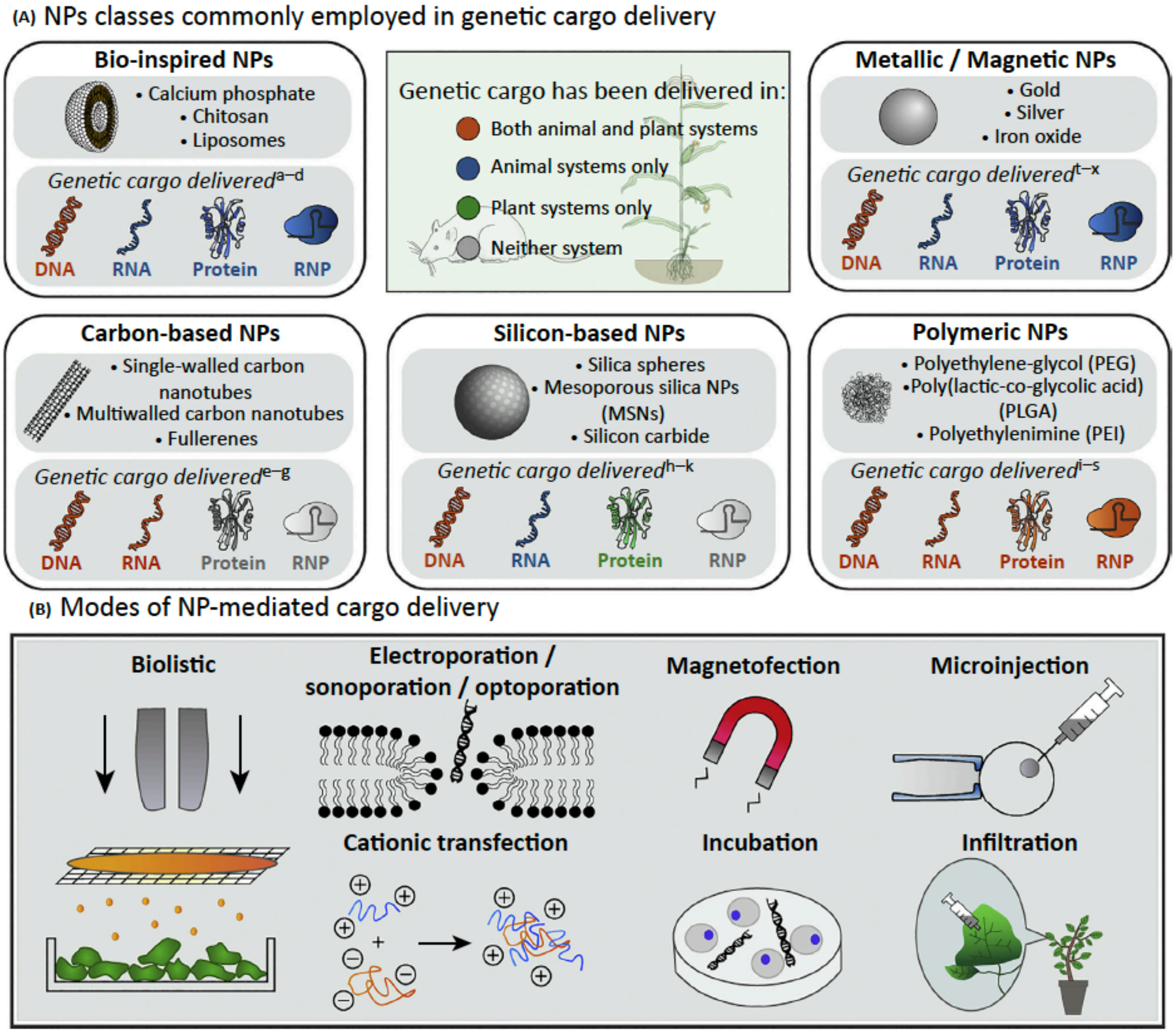

Figure 2. Nanoparticle (NP)-mediated genetic cargo delivery to animals and plants.

a, Nanoparticles that are commonly used in both animal and plant systems cover four major categories: carbon-based, polymeric, bio-inspired, and metallic / magnetic. We include an illustration of the delivery of various genetic cargo DNA, RNA, ribonucleoprotein (RNP) with each of the four NP types across animal and plant systems. It is evident that NP-mediated delivery has been utilized with a greater variety of genetic cargo in animals than in plants. **b,** NP-mediated cargo delivery is conducted *via* various means. Physical methods include creating transient pores in the cell membrane with electric fields, soundwaves, or light, microinjection, magnetofection, and biolistic particle delivery. Non-physical methods include cationic carriers, incubation, and infiltration. a[37], b[38], c[39], d[40], e[41], f[42], g[43], h[44], i[45], j[46], k[47], l[48], m[49], n[50], o[51], p[52], q[53], r[54], s[20], t[55], u[56], v[57], w[58], x[59].

1.4.2. Heuristics for nanoparticle design

While a complete structure-function landscape of physical and chemical NP properties that drive cargo loading and cellular internalization remains elusive, a heuristic approach to nanocarrier design is a useful starting point for NP implementation in plants. Passive uptake and transport of NPs throughout plant tissue is primarily limited by pore diameters, setting size exclusion limits (SELs) for epidermal, endodermal, parenchymal, and vascular transport[60]. The cell wall, the main barrier to NP-mediated delivery in plants, is commonly thought to exclude particles >5-20 nm, although recently NPs up to 50 nm in diameter have been reported as cell wall-permeable through transport mechanisms yet unknown[61]. For genetic engineering applications, where cytosolic or nuclear localization is necessary, the cell and/or nuclear membrane(s) are additional barriers. Cellular uptake can occur through both energy-dependent (endocytosis) and energy-independent (direct penetration) pathways. NP charge, size, and shape greatly influence these pathways, the most common being clathrin-dependent endocytosis[62]. For delivery to walled plant cells, the cell wall is the practical concern for cellular uptake as the cell membrane SEL (>500 nm) is much larger than the cell wall's (<50 nm). It is commonly reported that internalization is faster and more efficient for cationic NPs *vs.* anionic due to binding with the negatively-charged cell membrane[63]; this charge preference effect has been demonstrated in plant cell membranes as well[64].

In animal cells, rod-like NPs show appreciably higher uptake *vs.* spherical NPs due to increased propensity for clathrin-independent pathways[65], while these comparisons have not been made in plants. Serag and colleagues report CNT internalization through both direct penetration[66] and endocytosis[67] in protoplasts, supporting conclusions in animals that high aspect ratio NPs undergo vesicle-free internalization. However, in those studies, CNT internalization has only been shown for cell wall-impermeable multi-walled CNTs in protoplasts. Furthermore, it is well established that endogenous proteins adsorb to NPs *in vivo* to create a protein corona that alters the effective NP chemistry and geometry, thus mediating NP-cell interactions and uptake pathways[68]. To-date, the effect of protein corona composition on NP-plant interactions has not been explored.

Endosomal escape is critical for cytosolic, nuclear, or organelle-specific targeting, as vesicle-entrapped NPs can be trafficked for degradation or exocytosis. Cationic, pH-buffering polymers are well known endosome disruption agents[69] that can function as ligands to improve endosomal escape for NPs commonly used in plants (CNTs, gold, MSNs). Subcellular localization of NPs in plants is not well-understood but will depend on the uptake pathway, as endocytic proteins play a role in endosome fate, whereby direct cell penetration bypasses endocytosis entirely. Notably, endocytosed single-walled-CNTs in plants are trafficked to vacuoles but localize in the cytosol when loaded with DNA. Chang and colleagues report energy-independent internalization to walled cells by organically-functionalized MSNs[70], suggesting that surface chemistry, secondary to geometry, is critical to designing nanocarriers within the cell wall SEL.

Most NPs allow direct physical adsorption (physisorption) of biomolecules as a simple, reversible conjugation strategy. However, depending on the specific NP and cargo, direct physisorption may be unstable, and thus electrostatic interactions are preferable for non-covalent cargo loading. Conveniently, cationic surface chemistry not only enhances endocytic uptake and escape, but it is also amenable for electrostatic loading *via* attraction to the anionic phosphate backbone in DNA/RNA or anionic residues on protein surfaces. Covalent NP surface functionalization is typically achieved *via* a suite of 'click' chemistries[71]. Notably, covalent attachment of thiolated DNA to gold NPs has shown recent success[59] but the field remains open to novel, non-toxic strategies for surface bioconjugation, especially for applications in plants (Fig. 2). Alternatively, porous NPs such as MSNs can be internally loaded with macromolecules or small chemicals alike for controlled intracellular release[72].

NPs with some or all of the properties mentioned above have demonstrated successful biomolecule delivery in plants and they are good starting points for choosing the appropriate NP, ligand, and cargo for a given application. However, it should be noted that nanocarrier design is a complex, multivariable optimization process such that success will likely require tweaking of these heuristics for different systems until a complete NP structure-function relationship is established for plant systems.

1.4.3. Nanomaterials for plant genetic engineering

NPs are valuable materials for intracellular biomolecule delivery owing to their ability to cross biological membranes, protection and release of diverse cargoes, and multifaceted targeting *via* chemical and physical tunability. Such properties have enabled NPs to revolutionize targeted delivery and controlled release in mammalian systems. However, nanocarrier delivery in plants remains largely underexplored. In 2007, Torney and colleagues were the first to demonstrate NP delivery of DNA and chemicals to *Nicotiana tabacum* plants *via* biolistic-delivery of 100-200 nm gold-capped MSNs[45]. In this study, a chemical expression inducer was loaded into MSN pores (~3 nm) that were subsequently covalently-capped with gold NPs. The capped MSNs were then coated with GFP plasmids and delivered by gene gun to *Nicotiana tabacum* cotyledons, wherein GFP expression was triggered upon uncapping and release of the expression inducer. This seminal paper demonstrates proof of concept that NP delivery strategies common for mammalian systems can be adapted to plants. Currently, only a handful of studies have been published on NP-mediated genetic engineering in plants (Table 1).

Table 1: Select summary of NP-mediated genetic engineering in plants

	NP type	Cargo	Plant	Delivery	Notes
With external aid	Gold capped MSN[45]	GFP plasmid, expression inducer	*N. tabacum* cotyledons; *Z. mays* embryos	Biolistic	Co-delivery and controlled release
	Poly-L-lysine coated starch[73]	GFP plasmid	*Dioscorea zingiberensis*, Wright calli	Sono-poration	5% transient expression, some integration occurs
	Gold plated MSN[47]	GFP & mCherry plasmids, GFP protein	*Z. mays* embryos, *Allium cepa* epidermis	Biolistic	DNA and protein co-delivery
	Magnetic gold[74]	GUS plasmid	*Brassica napus* protoplasts	Magnetic field	Transient GUS expression
	DMAEM polymer[75]	YFP and GFP plasmids	*N. tabacum* and *C. purpureus* protoplasts	PEG	Both transient and stable expression
	Magnetic Fe_3O_4[56]	Selectable marker gene plasmids	*Gossypium hirsutum* pollen	Magnetic field	1% stable transformation
	NP type	**Cargo**	**Plant**	**Delivery**	**Notes**
***In vitro* no external aid**	PAMAM dendrimer[76]	GFP plasmid	*Agrostis stolonifera* calli	Passive	48.5% transient expression
	Calcium phosphate[37]	GUS plasmid	*Brassica juncea* hypocotyl	Passive	80.7% stable transformation
	Organically functionalized CNTs[77]	YFP plasmid	*N. tabacum* protoplasts, leaf explants	Passive	Both transient & stable expression
***In vivo* no external aid**	Organically functionalized MSNs[70]	mCherry plasmid	*A. thaliana* roots	Passive	46.5% transient expression
	PAMAM dendrimer[78]	dsDNA for RNAi	*A. thaliana* roots	Passive	Developmental gene silencing
	Polymer functionalized CNTs[42]	GFP plasmid and siRNA	*E. sativa*, *N. benthamiana*, *T. aestivum leaves*	Passive	95% silencing, transient expression

Many NP delivery strategies still require a gene gun, electromagnetic field, or protoplast PEG-transfection as NP geometry, size, and functionalization has not yet been fully optimized to bypass the cell wall. However, for these systems where mechanical or chemical aid is necessary for internalization, the small size and high surface area of nanocarriers offers superior performance over conventional methods. For instance, Torney and colleagues' pioneering MSN study achieved transgene expression with 1,000 times less DNA than required by conventional PEG-transfection in protoplasts[45].

A few recent examples show promise for NP-mediated passive delivery to plants *in vitro*[37] and *in vivo*[78], for example, *N. tabacum* protoplasts[77] and *Arabidopsis thaliana* roots[70], respectively. Passive biomolecule delivery to plants is promising for minimally invasive, species-independent *in vivo* genetic engineering of plants, especially for transient expression. Currently, stable transformation requires progeny regeneration from edited protoplasts or explants and thus regeneration protocols should be improved alongside the optimization of NP delivery methods. The potential of NP-based plant delivery methods is underscored by the limitations of *in vitro* plant studies in general, wherein regeneration capacity varies widely across species, genotype, and even within a single plant depending on developmental age of source tissue[79]. Delivery *in vivo* to plants is inherently difficult compared to *in vitro* protoplasts or calli due to the higher density of transport barriers in whole tissue.

While many more studies are needed to optimize NP properties and functionalization, these early results are promising for further exploration of NPs as a plant biomolecule delivery platform that addresses shortcomings of conventional methods. Furthermore, with the advent of nuclease-based gene editing technologies, it is of great interest to optimize the delivery of these revolutionary genetic engineering tools by exploring NP-based delivery strategies for these diverse biomolecular cargoes.

1.5. Genome Editing Has Enabled a New Era of Plant Science

Engineered nuclease systems, namely ZFNs, TALENs, and CRISPR-Cas, have emerged as a breakthrough genome editing tool due to their high genetic engineering specificity and efficiency, whereby CRISPR-Cas has shown increased simplicity, affordability, and multiplexing capabilities over TALENs and ZFNs in plants. Since 2012, CRISPR-Cas has shown success for genome editing in both model and crop species[80] including *A. thaliana*, *N. benthamiana*, *N. tabacum* (tobacco), *O. sativa* (rice), *Triticum aestivum* (wheat), *Zea mays* (corn), *Solanum lycopersicum* (tomato), and *Sorghum bicolor*, among others[9]. Notably, CRISPR-Cas mutations as small as 1 bp have been conserved through three plant generations[81], which is promising for stable transgene-free modified crops[82]. As with traditional genetic engineering of plants, many of the limitations for implementing gene editing tools in plants (low editing efficiency, tissue damage, species limitations, cargo-type limitations) originate in biomolecular transport challenges into plant cells. As such, NP-based biomolecule delivery to plants stands to enable higher-throughput plant genome editing *via* both DNA, sgRNA, and RNP delivery, and thus warrants a discussion on the state of the plant genome editing field.

1.5.1. Global landscape of regulatory uncertainty toward genetically engineered crops

Genetic engineering of crops has evolved to overcome limitations in traditional breeding, because breeding is relatively slow, laborious, and lacks precise control over plant genotype and phenotype generation. Modern biotechnology enables rapid development of crop variants with disease and pest resistance, stress tolerance, higher yield, and enhanced nutritional value. Since 1996, global GMO cultivation has increased 110-fold to 185 megahectares in 2016[83] (Fig. 3). The U.S. is a leader in GMO commercialization but highly regulates production of modified crops which poses, among other challenges, significant financial barriers to the production and commercialization of new crop variants[84]. The USDA defines GMOs as organisms engineered to contain transgenes, while genome editing without transgene integration may be considered indistinguishable from natural mutations or breeding lines. Regulatory review is automatically triggered by the use of *Agrobacterium* in the U.S. while organisms transformed by other methods may be exempted by voluntary inquiry.

The European Union, on the other hand, has a stricter definition of a GMO: an organism whose genome has been altered by any method other than mating or natural recombination[85], which includes mutations made using site-directed nucleases. Given the difficulty in implementing genome sequencing to identify edited – as opposed to genetically engineered – plants, it remains unclear how enforcement of GMO status will proceed for gene edited plants. In light of ambiguous or restrictive legislation, it is important to bring attention to the benefits of nuclease-based gene editing *versus* traditional genetic engineering. While conventional gene editing and breeding in plants offers some control over transgene integration, nuclease-based techniques can introduce precise, transgene-free genome edits more efficiently and at a much faster rate. To date, five CRISPR-edited plants have gone to market in the U.S. without regulatory oversight, bypassing the GMO pipeline of several years and tens of millions of dollars[86]. The global regulatory landscape of modern genome editing in plants is heterogeneous and constantly evolving (Fig. 3). Therefore, non-transgenic crops enhanced *via* nuclease-based techniques could provide a pragmatic approach to overcome regulatory restrictions and ensure scientific progress as well as commercial implementation of engineered crop variants.

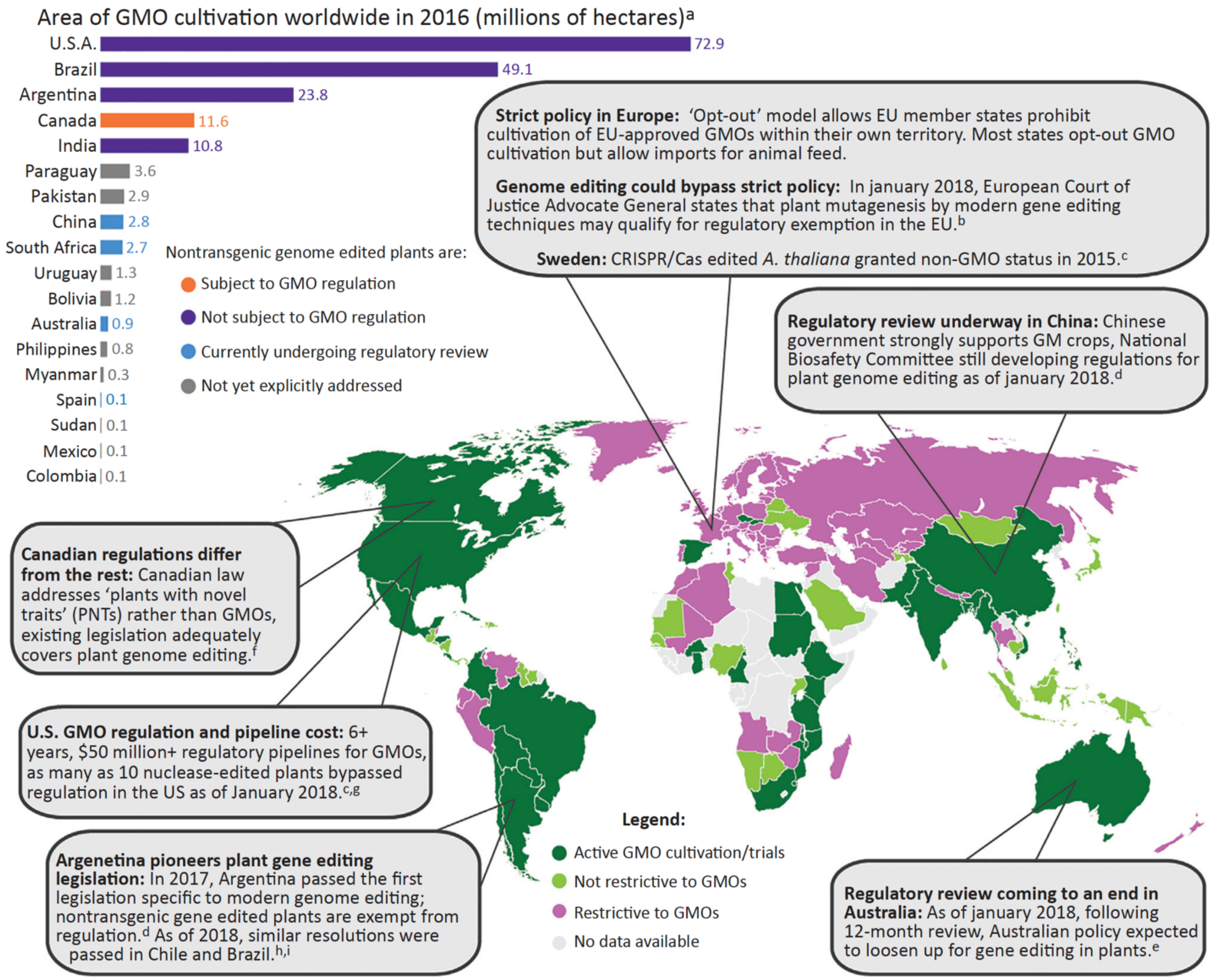

Figure 3. GMO cultivation and regulatory attitudes worldwide.
Despite a long, expensive regulatory pipeline, the U.S. is a leader for GMO cultivation worldwide, followed by Brazil and Argentina, with Argentina being the first to directly address modern genome editing techniques in GMO legislation. European and Australian regulatory attitudes are strict but have recently evolved as of January 2018, suggesting that regulations for genome edited plants will soon be relaxed in these regions. Nuclease-based edits without transgene integration escape regulation even in countries with large agricultural GMO industries and complex regulatory systems.

1.5.2. Nanocarriers hold promise for increasing throughput of plant genome editing

Genome editing tools may increase the throughput of plant molecular biology and genetic studies, and may shift the paradigm in regulatory oversight of transgenic plants. Species, amenable tissue, expression strategy, and delivery method contribute to the efficacy of transgene expression or modification, and to the propensity of transgene integration into the host genome. RNP delivery is often preferred, as DNA-free methods fully circumvent the possibility of transgene integration, and RNP delivery has been demonstrated to be more efficient over plasmid delivery, all while reducing off-target effects. Recently, RNP delivery has been demonstrated in *A. thaliana* and *O. sativa* protoplasts *via* PEG-transfection[20] and *Z. mays* embryos *via* gene gun delivery[21]; the methods used in both of these studies are primarily throughput-limited by regeneration of stable progeny from genome-edited parent cells. The challenge to realizing efficient, stable gene editing in plants is two-fold. First, plant germline cells cannot be transformed by any current method (with the exception of *Arabidopsis* floral dip) and therefore progeny must be regenerated from parent tissue. Second, the cell wall imposes a rigid transport barrier to biomolecule delivery such that conventional delivery in plants is either destructive and inefficient, or host-specific. Thus, the foremost limitation for broad-scale implementation of plant genome editing originates from an inability to target germline cells, and the absence of an efficient and species-independent bio-cargo delivery strategy. While engineered nuclease systems have begun to reveal remarkable potential for the future of plant genome engineering, novel carriers are required to overcome the restrictions of conventional delivery methods but could also begin to pave the way for efficient progeny regeneration or direct germline editing in plants.

NPs have begun to facilitate and enhance genome editing through efficient and targeted delivery of plasmids, RNA, and RNPs[87]. In mammalian cells, NPs are routinely used for efficient, direct cytosolic/nuclear delivery of Cas-RNPs in many cell types[58], and RNP delivery has been shown to greatly reduce off-target effects in comparison to plasmid-based CRISPR systems. However, in plants, the cell wall has hindered the development of an analogous system that can passively deliver genome editing cargo to mature plants. Thus, there remains much potential for designing NP carriers with diverse cargo loading capabilities (DNA, RNA, proteins, ribonucleoproteins) and optimal geometry/chemistry to efficiently bypass the cell wall and membrane in dense plant tissue without external aid. Previous work shows that some NP formulations are capable of passive internalization *in planta* with DNA, RNA, or protein cargo. These NP scaffolds - namely CNTs, MSNs, and polymeric NPs - should be further explored for delivering engineered nuclease systems to plants.

This dissertation studies the nanoparticle system carbon nanotubes (CNTs) for efficient biomolecule delivery into intact and mature plant leaf cells for many impactful applications of plant biotechnology and bioengineering. Chapter 2 details the development, characterization and impact of polymer-functionalized CNTs to deliver plasmid DNA into plant cells for genetic engineering applications. Next, Chapter 3 discusses the usage of pristine single walled carbon nanotubes (SWNTs) for the delivery of small interfering RNA for efficient gene knock-down in plants. Chapter 4 studies the effect of important nanoparticle parameters that dictate plant cell entry and efficient gene silencing using programmable DNA nanostructures. Lastly, Chapter 5 presents the concluding remarks, and short- and long-term future directions of the work presented in this dissertation.

CHAPTER 2. CARBON NANOTUBES ENABLE DELIVERY OF GENETIC MATERIAL IN MATURE PLANTS

2.1. Summary

Genetic engineering of plants is at the core of sustainability efforts, natural product synthesis and crop engineering. The plant cell wall is a barrier that limits the ease and throughput of exogenous biomolecule delivery to plants. Current delivery methods either suffer from host-range limitations, low transformation efficiencies, tissue damage or unavoidable DNA integration into the host plant genome. This chapter demonstrates efficient diffusion-based biomolecule delivery into intact plants of several species with pristine and chemically functionalized high aspect ratio nanomaterials. Efficient DNA delivery and strong protein expression without transgene integration is accomplished in *Nicotiana benthamiana* (*Nb*), *Eruca sativa* (arugula), *Triticum aestivum* (wheat) and *Gossypium hirsutum* (cotton) leaves and arugula protoplasts. I find that nanomaterials not only facilitate biomolecule transport into plant cells but also protect polynucleotides from nuclease degradation. This work provides a tool for species-independent and passive delivery of genetic material, without transgene integration, into plant cells for diverse biotechnology applications.

2.2. Introduction

Plant biotechnology is critical to address the world's leading challenges in meeting our growing food and energy demands, and as a tool for scalable pharmaceutical manufacturing. In agriculture, genetic enhancement of plants can be employed to create crops that have higher yields and are resistant to herbicides[88], insects[89], diseases[90] and abiotic stress[91]. In pharmaceuticals and therapeutics, genetically engineered plants can be used to synthesize valuable small-molecule drugs and recombinant proteins[92]. Furthermore, bioengineered plants may provide cleaner and more efficient biofuels[93,94].

Despite several decades of advancements in biotechnology, most plant species remain difficult to transform genetically[95]. A bottleneck facing efficient plant genetic transformation is biomolecule delivery into plant cells through the rigid and multilayered cell wall. Currently, few well-established delivery tools exist that can transfer biomolecules into plant cells, and each has considerable limitations. *Agrobacterium*-mediated delivery[96] is the most commonly used tool for gene delivery into plants, but this technique has limitations in that efficient delivery is limited to a narrow range of plant species and tissue types, and is unable to perform DNA- and transgene-free editing[97].

The one other commonly used tool for plant transformation is biolistic particle delivery (also called the gene gun)[19], which can deliver biomolecules into a wider range of plant species but faces the limitations of providing only bombarded-site expression, causing plant tissue damage when high bombardment pressures are used[95], being subject to possible limitations of specimen size and positioning in the biolistic chamber, and the requirement of using a substantial amount of DNA to achieve the desired delivery efficiency. For transient expression of heterologous proteins in plants, the use of plant viral vectors such as tobacco mosaic virus-based Geneware technology, potato virus X and cowpea mosaic virus[98] is beneficial for large-scale production of industrially relevant proteins. However, viral vectors are only compatible with select plant species and expression cassette sizes, which limits the plant host and hinders expression of large or multiple proteins simultaneously. Additionally, the use of viral vectors, even if used for transient expression of gene editing systems, are usually subject to regulatory purview because of the pathogenic origin of viruses and because some viruses integrate portions of their genetic material into the plant host genome[99].

While nanomaterials have been studied for gene delivery into animal cells[100,101], their potential for plant systems remains understudied[102]. Several reports describe the uptake of nanomaterials by plant cells; however, most of these foundational studies deliver only non-functional cargoes[33], are carried out in protoplast cell culture[51] or use mechanical aids (gene gun[103] or ultrasound[73]) to enable nanoparticle entry into the walled plant cells. Mesoporous silica nanoparticles[70] (MSNs), DNA nanostructures and DNA origami[104], silicon carbide whiskers[105] (SCWs) and layered double hydroxide (LDH) clay nanosheets[106] have demonstrated the possibility of nanoscale internalization into walled plant cells without strong mechanical aid to deliver functional biological cargoes. In the MSN study, researchers demonstrated passive delivery of plasmid DNA loaded MSNs into *Arabidopsis* roots by co-culture, an important initial development for passive nanoparticle transport in model plant species root cells[70]. SCWs have enabled delivery of genes into undifferentiated plant tissues and explants suspended in solution *via* incubation and vortexing of whiskers together with plant cells and DNA, enabling stable transformation and selection of transgenic plants in tissue culture[105]. Vortexing the large and stiff SCWs (micrometer-sized) is hypothesized to pierce or rupture the cell wall and enable DNA entry into cells. In this manner, SCWs permeabilize the cell wall to enable entry of free solution-phase DNA; however, this delivery mechanism is not amenable for subcellular/tissue targeting or intact-plant testing and may compromise transformation efficiency and cell health. Important developments with LDHs have shown effective delivery of RNAi molecules (double-stranded RNAs) for gene silencing in the model species *Nicotiana tabacum*[106], paving the way towards future developments in plant bionanotechnology; however, to my knowledge, LDH has yet to be implemented for plasmid DNA delivery to enable gene expression studies.

So far, there has yet to be a plant transformation method that enables high-efficiency plasmid DNA delivery, without transgene integration, in a plant species-independent manner. This chapter addresses the long-standing challenge of DNA delivery to mature model and non-model plants with nanomaterials, filling a key void in the plant transformation toolkit. With certain surface chemistries, high aspect ratio nanomaterials such as carbon nanotubes (CNTs) have been observed to passively traverse extracted chloroplast[107] and plant membranes[108] as a result of several figures of merit: high aspect ratio, exceptional tensile strength, high surface area-to-volume ratio and biocompatibility. When bound to CNTs, biomolecules are protected from cellular metabolism and degradation[109], exhibiting superior biostability compared to free biomolecules. Moreover, single-walled carbon nanotubes (SWCNTs) have strong intrinsic near-infrared (NIR) fluorescence[110,111] within the tissue transparency window and thus benefit from reduced photon scattering, allowing for tracking of cargo–nanoparticle complexes deep in plant tissues. However, previous incorporation of CNTs in plant systems is limited to exploratory studies of CNT biocompatibility[34,112] and sensing of small molecules in plant tissues[113] by introducing CNTs complexed to synthetic fluorescent dyes or polymers.

This chapter details the development of a CNT-based platform, which further advances the aforementioned field of nanoparticle-directed plant transformation. I generated and validated a platform that can deliver plasmid DNA into both model and crop plants with high efficiency, no toxicity, without mechanical aid and without transgene integration – a combination of features that is not attainable with existing plant transformation approaches. Covalently functionalized or pristine CNTs were used to deliver DNA into mature *Nicotiana benthamiana*, *Eruca sativa* (arugula), *Triticum aestivum* (wheat) and *Gossypium hirsutum* (cotton) leaves, generating strong protein expression. I also showed CNT-based protein expression in arugula protoplasts, a common plant tissue culture, with 85% transformation efficiency. This study establishes that CNTs, which are below the size exclusion limit of the plant cell wall (at least one dimension at or below ~20 nm), could be a promising solution for overcoming plant biomolecule delivery limitations in a species-independent and non-integrating manner, and could enable high-throughput plant genetic transformations for a variety of plant biotechnology applications.

2.3. Grafting DNA on CNT Scaffolds

For the transgene expression study, I developed two distinct grafting methods to load green fluorescent protein (GFP)-encoding plasmids or their linear PCR amplicon fragments on SWCNTs and multi-walled carbon nanotubes (MWCNTs). The first DNA grafting method involves direct adsorption of DNA on CNTs *via* dialysis. Initially, CNTs are coated with a surfactant – sodium dodecyl sulfate (SDS). During dialysis, SDS desorbs from the CNT surface and exits the dialysis membrane, while DNA adsorbs onto the surface of CNTs in a dynamic ligand exchange process (Fig. 4a). With this method, double-stranded DNA vectors graft on CNTs through π–π stacking interactions. The adsorption of DNA on CNTs is confirmed through a solvatochromic shift in the CNT NIR fluorescence emission spectra, which is characteristic of a DNA adsorption-induced change in the CNT dielectric environment[114] (Fig. 4a). Control dialysis aliquots of SDS-coated CNTs, in the absence of DNA, show rapid CNT precipitation and lack NIR fluorescence (Fig. 4b), confirming SDS desorption and replacement by DNA in dialysis aliquots with DNA. Additionally, at the end of the dialysis procedure, I confirmed that there is no SDS left in the cartridge by using Stains-all dye. The complete characterization (zeta potential, atomic force microscopy (AFM) height and DNA loading efficiency) of CNTs prepared *via* dialysis is summarized in Fig. 5.

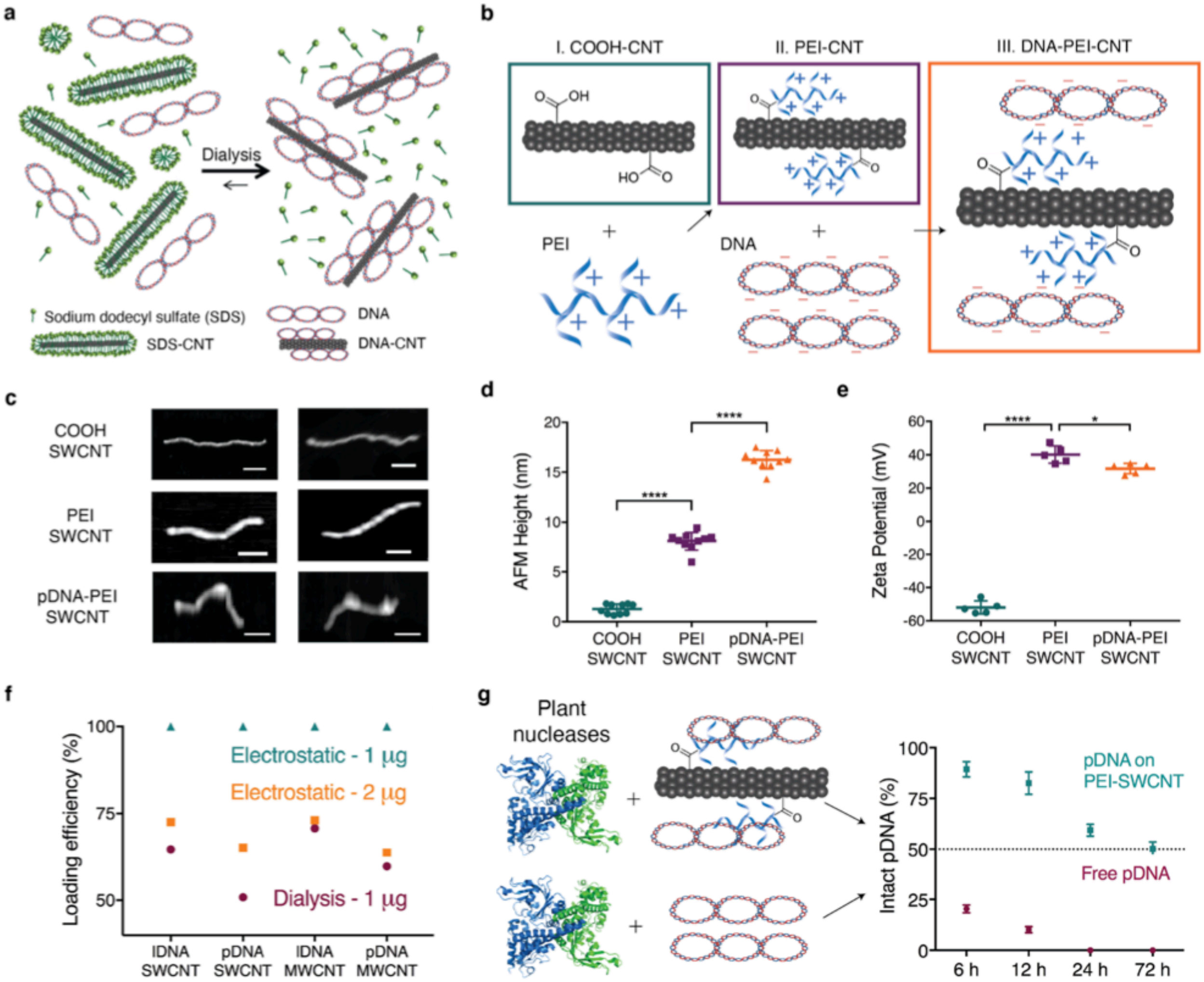

Figure 4. Strategies for grafting DNA on CNT scaffolds and characterization of DNA - CNT conjugates.
a, DNA grafting on surfactant suspended CNTs through π–π stacking *via* the dialysis method. **b,** DNA grafting on PEI-modified carboxylated CNTs through electrostatic attachment. **c**, Representative AFM images of carboxylated SWCNTs, PEI-modified SWCNTs and plasmid DNA-loaded PEI-modified SWCNTs. Scale bars, 100 nm. **d**, Average height profile of SWCNTs before and after PEI reaction and pDNA loading measured *via* AFM. ****P < 0.0001 in one-way analysis of variance (ANOVA). Error bars indicate s.d. (n = 10). **e**, Zeta potential measurements of SWCNTs before and after PEI reaction and pDNA loading measured *via* dynamic light scattering (DLS). *P = 0.0191 and ****P < 0.0001 in one-way ANOVA. Error bars indicate s.d. (n = 5). **f**, Agarose gel electrophoresis quantification (Figs. 2 and 3) demonstrates a loading efficiency of 1 μg DNA onto 1 μg electrostatically modified and dialysis-made CNTs, and a loading efficiency of 2 μg DNA onto 1 μg electrostatically modified CNTs. **g**, Degradation of free pDNA versus pDNA on PEI–CNTs by plant nucleases obtained from a leaf lysate solution suggests pDNA protection on CNT scaffolds. Error bars indicate s.d. (n = 3).

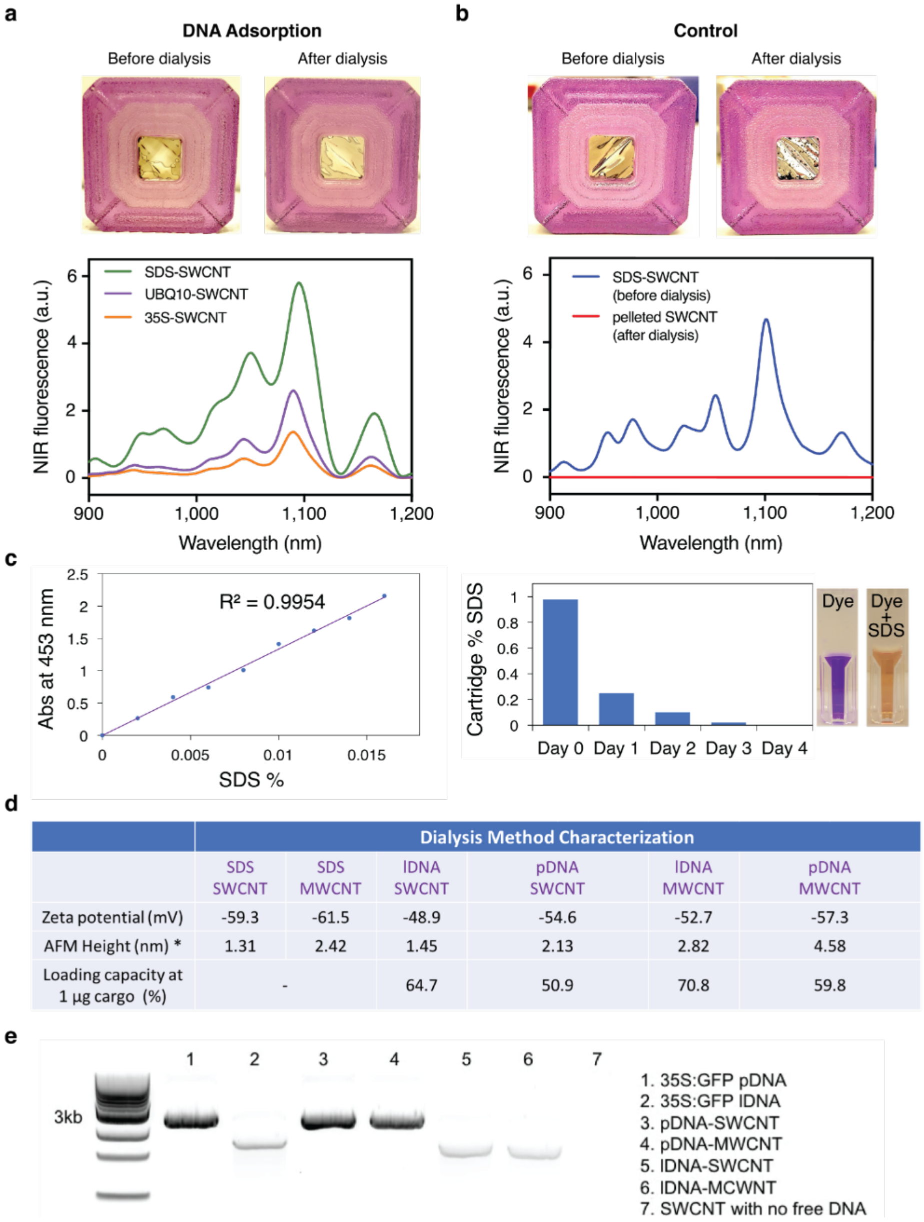

	Dialysis Method Characterization					
	SDS SWCNT	SDS MWCNT	lDNA SWCNT	pDNA SWCNT	lDNA MWCNT	pDNA MWCNT
Zeta potential (mV)	-59.3	-61.5	-48.9	-54.6	-52.7	-57.3
AFM Height (nm) *	1.31	2.42	1.45	2.13	2.82	4.58
Loading capacity at 1 μg cargo (%)	-		64.7	50.9	70.8	59.8

Figure 5. Confirmation of DNA adsorption on CNTs through dialysis and loading efficiency characterization.
a, Adsorption of DNA on CNTs is confirmed through a 5-nm wavelength shift in the SWCNT nIR fluorescence emission spectra. No CNT precipitation is observed after dialysis with DNA, confirming that DNA adsorption follows SDS desorption from CNTs. **b**, Control dialysis aliquots of SDS coated CNTs in the absence of DNA show rapid CNT precipitation and lack nIR fluorescence, confirming DNA adsorption and SDS desorption in the sample 'a' dialysis. **c**, Stains-all dye changes color from purple to yellow in the presence

of SDS. A standard curve correlates absorbance of dye at 453 nm to %SDS concentration. The standard curve is used to detect %SDS left in the dialysis cartridge at Day 0, 1, 2, 3 and 4. At day 4, when dialysis is terminated, there is no SDS left in the cartridge. **d**, Characterization of nanoconjugates prepared *via* dialysis; zeta potential, AFM height, and loading efficiency at 1 g DNA is presented. **e**, Due to their large size, DNA-CNT conjugates do not run into the agarose gel, hence the bands visualized in the gel are free DNA bands. By measuring the intensity of unloaded DNA bands normalized with respect to the intensities of lane 1 and 2, which are loaded with a known amount of pDNA and lDNA, the loading efficiency of lDNA onto SWCNTs is calculated to be 64.7%, pDNA onto SWCNTs is 50.9%, lDNA onto MWCNTs is 70.8%, and pDNA onto MWCNTs is 59.8% with the dialysis method.

The second method for DNA grafting on CNTs is electrostatic grafting, in which carboxylated CNTs (COOH-CNT) are first covalently modified with a cationic polymer (poly-ethylenimine, PEI) to carry a net positive charge. Next, positively charged CNTs (PEI-CNT) are incubated with negatively charged DNA vectors (Fig. 4b). The attachment of PEI and adsorption of DNA on CNTs was verified by AFM *via* CNT height increases after each step (Fig. 4c). Nanoparticle heights before and after reaction with PEI are measured to be 1.3 nm and 8.1 nm for COOH- and PEI-SWCNT, respectively, confirming PEI binding. AFM revealed that the SWCNT height increases from 8.1 nm to 16.3 nm after incubation with DNA vectors, as expected, further confirming DNA grafting on SWCNTs (Fig. 4d). AFM characterization of MWCNT conjugates is provided in Fig. 6a.

The covalent attachment of PEI and electrostatic adsorption of DNA on CNTs was also confirmed through zeta potential measurements (Fig. 4e), after extensive washing of unreacted PEI. The initial zeta potential of −51.9 mV for COOH-SWCNT increases to +40.2 mV after reaction with positively charged PEI, and subsequently decreases to +31.7 mV when incubated with negatively charged DNA. The characterization of electrostatically prepared CNT conjugates is summarized in Fig. 6b. I note that DNA-CNT conjugates prepared *via* electrostatic grafting have higher DNA loading efficiencies compared to the conjugates prepared *via* the dialysis method. I demonstrate that the optimum DNA amount to be loaded on PEI-CNTs has a 1:1 DNA:CNT mass ratio (Fig. 4f, 6c and 6d). Electrostatically grafted CNTs have 100% DNA loading efficiencies, whereas dialysis-loaded DNA-CNTs show 50–70% loading efficiencies when loaded with the same amount of DNA (Fig. 6e).

The intracellular stability of DNA-loaded PEI-CNT conjugates was assessed by incubating conjugates with proteins at a total protein concentration similar to plant intracellular conditions. After 3 days of PEI-CNT incubation with proteins, half of the DNA remains adsorbed on the nanoparticles (Fig. 6f). I also show that DNA adsorbed on PEI-CNTs is partially protected from endonuclease degradation compared to free DNA, when incubated with total proteins extracted from plant leaves. Following a 3-day incubation with plant cell lysate, 100% of free DNA is degraded, whereas 50% of DNA on DNA-PEI-CNTs remains intact (Fig. 4g). DNA protection on CNTs was further validated *via* single-molecule total internal reflection fluorescence (smTIRF) microscopy: upon treatment with S1 nuclease, free DNA is degraded by 81.4%, whereas DNA on CNTs is only degraded by 49.8%, commensurate with the bulk assays (Fig. 7).

a

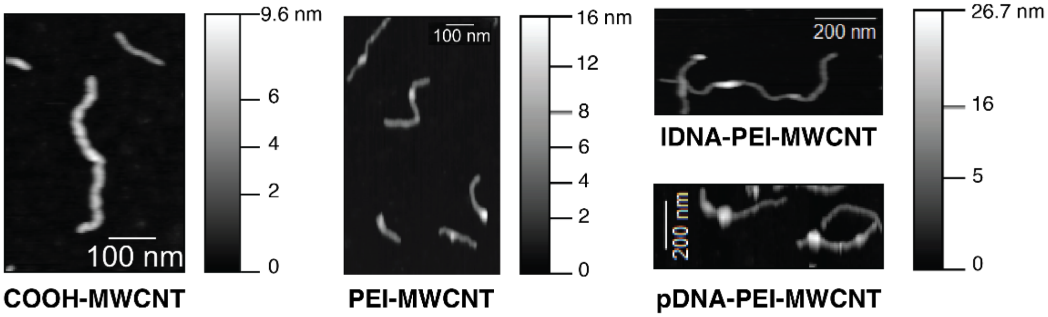

b

	Electrostatic Method Characterization							
	COOH SWCNT	COOH MWCNT	PEI SWCNT	PEI MWCNT	lDNA-PEI SWCNT	pDNA-PEI SWCNT	lDNA-PEI MWCNT	pDNA-PEI MWCNT
Zeta potential (mV)	-54.7	-41.7	+42.4	+46.3	+36.4	+30.7	+38.7	+33.4
AFM Height (nm)	1.37	6	8.3	12.1	14.75	16.43	22.8	26.7
AFM Length (nm)	820	1250	616	785	610	590	725	700
Loading capacity at 1 μg cargo (%)	-				100	100	100	100
Loading capacity at 2 μg cargo (%)	-				72.6	65.2	73.1	63.8

c

1 *μg* cargo

1. 35S:GFP pDNA
2. 35S:GFP lDNA
3. pDNA-PEI-SWCNT
4. pDNA-PEI-MWCNT
5. lDNA-PEI-SWCNT
6. lDNA-PEI-MCWNT
7. MWCNT with no free DNA

d

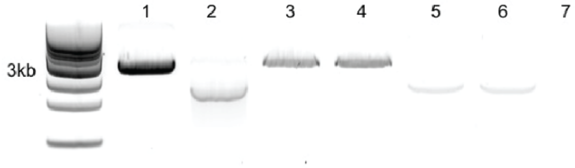

2 *μg* cargo

1. 35S:GFP pDNA
2. 35S:GFP lDNA
3. pDNA-PEI-SWCNT
4. pDNA-PEI-MWCNT
5. lDNA-PEI-SWCNT
6. lDNA-PEI-MCWNT
7. SWCNT with no free DNA

e

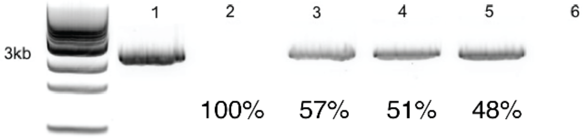

plasma incubation

1. 35S:GFP pDNA
2. pDNA-PEI-SWCNT in plasma 1 h
3. pDNA-PEI-SWCNT in plasma 24 h
4. pDNA-PEI-SWCNT in plasma 48 h
5. pDNA-PEI-SWCNT in plasma 72 h
6. plasma with 0.2 mg/μl protein

f

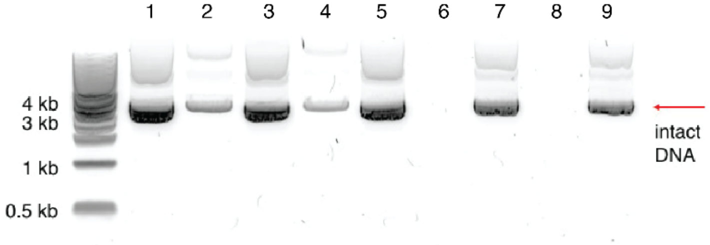

cell lysate treatment

1. pDNA standard
2. Free pDNA 6 h
3. pDNA on PEI-SWCNT 6 h
4. Free pDNA 12 h
5. pDNA on PEI-SWCNT 12 h
6. Free pDNA 24 h
7. pDNA on PEI-SWCNT 24 h
8. Free pDNA 72 h
9. pDNA on PEI-SWCNT 72 h

Figure 6. Confirmation of synthesis and DNA adsorption on PEI-CNTs with loading efficiency characterization.
a, Representative AFM imaging of MWCNTs prepared through electrostatic grafting. AFM imaging of carboxylated MWCNT nanoparticles before and after reaction with PEI confirms covalent PEI attachment. AFM also reveals that MWCNT nanoparticle height increases from 12.1 ± 0.87 to 22.8 ± 2.19 nm after incubation with DNA vectors. **b**, Characterization of nanoconjugates prepared with the electrostatic method of DNA loading on CNTs: zeta potential, AFM height and length, and loading capacity of 1 and 2 g DNA is presented. **c**, As there is no unbound DNA running into the agarose gel when 1 g PEI-CNTs are loaded with 1 g DNA, all loading capacities regardless of DNA conformation or nanotube type are 100% when a 1:1 DNA:CNT mass ratio is used. **d**, When 2 g PEI-CNTs are loaded instead with g DNA, I calculate a 72.6% loading efficiency of lDNA onto SWCNTs, a 65.2% loading efficiency of pDNA onto SWCNTs, a 73.1% loading efficiency of lDNA onto MWCNTs, and a 63.8% loading efficiency of pDNA onto MWCNTs. **e**, pDNA-PEI-CNTs are incubated in plasma containing 0.2 mg/L total protein to approximate the DNA desorption rate in intracellular conditions. Results show that even after a 72-hour incubation in plasma at 21°C, almost half of the DNA is still adsorbed on PEI-CNTs. **f**, Agarose gel electrophoresis of free pDNA and pDNA on PEI-CNTs incubated with plant lysate solution for 6, 12, 24, and 72 hours to determine pDNA protection against nuclease degradation on PEI-CNTs.

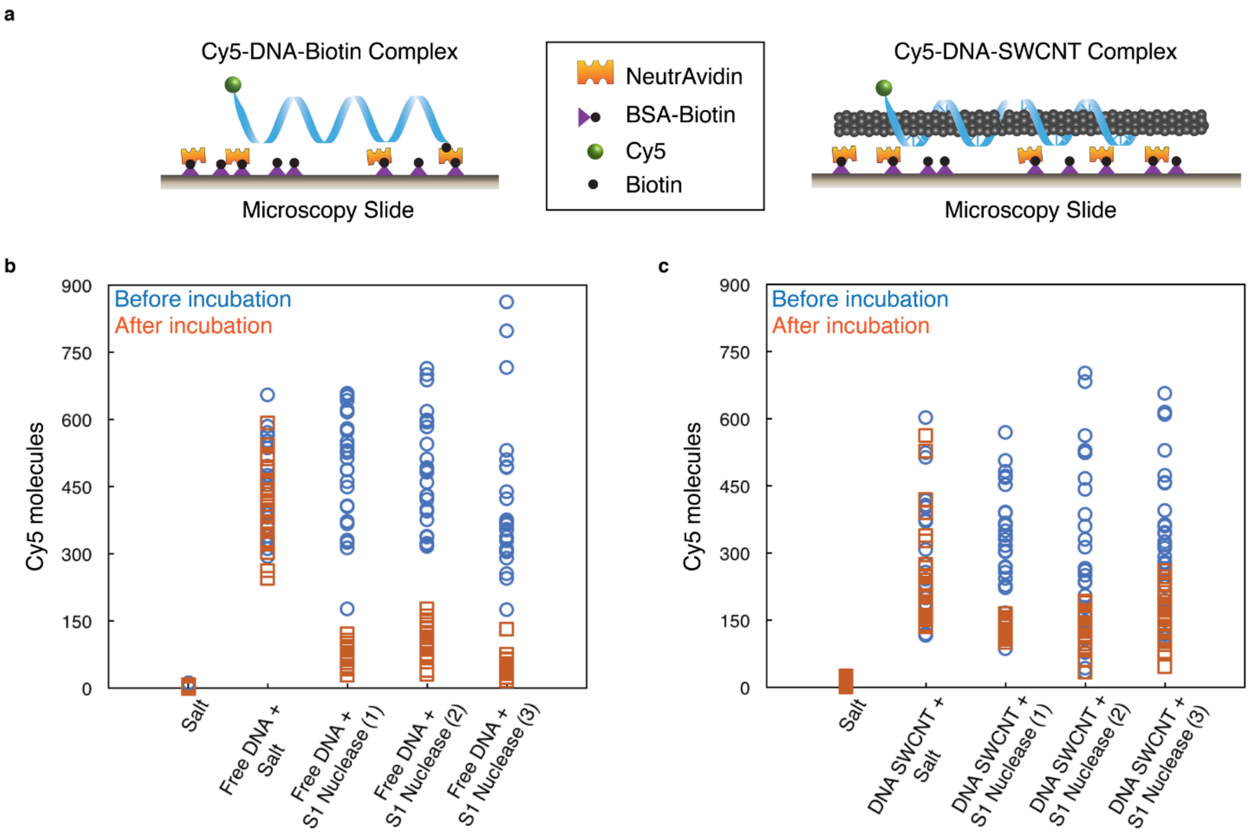

Figure 7. Single molecule TIRF (smTIRF) microscopy demonstrates DNA protection against nuclease degradation when on CNTs.
a, Schematics of microscopy slides for immobilization of Cy5-DNA-Biotin and Cy5-DNA-CNT complexes. The microscopy slide surface is first coated with BSA-Biotin, then incubated with NeutrAvidin. Cy5-DNA-Biotin is immobilized on the surface *via* Biotin-NeutrAvidin attraction, and Cy5-DNA-CNT is next immobilized on the surface *via* non-specific interaction of NeutrAvidin with CNTs. **b**, Raw smTIRF data for empty channel rinsed with salt solution, free DNA incubated with salt solution, and three experimental replicates of free DNA incubated with 2.8U/μL S1 nuclease, blue: before incubation and orange: after incubation. Data from 30 fields of view plotted for each sample before and after nuclease treatment.

2.4. DNA Delivery into Mature Plants with CNTs

Functional gene expression studies were implemented with arugula and cotton plant leaves to demonstrate the applicability of CNT platform to transform crop plants in addition to traditional model laboratory species, such as *N. benthamiana* (*Nb*). Furthermore, gene delivery and protein expression studies were carried out with wheat plants, demonstrating that CNT platform is also applicable to transform monocot plant species in addition to dicot plants.

After preparation of DNA-CNT conjugates with GFP-encoding DNA plasmids or linear PCR amplicons with dialysis or electrostatic grafting, DNA-CNTs were infiltrated into the true leaves of mature plants by introducing a small puncture on the abaxial surface of the leaf lamina with a pipette tip and infiltrating the solution with a needleless syringe. Post-infiltration, I hypothesize that DNA-CNTs traverse the plant cell wall and membrane to enter the plant cell (Fig. 8a). To confirm internalization of nanoparticles into mature leaf cells, Cy3-tagged DNA-CNTs were delivered to plant leaves and the nanoparticle fate was assessed with confocal microscopy of the infiltrated leaf tissue (Fig. 8b). For this experiment, a GFP mutant *Nb* plant was used, which constitutively expresses GFP, so that I could co-localize the Cy3 fluorescence from the DNA-CNTs with GFP fluorescence from inside the cells. When Cy3-DNA is delivered without CNTs, I do not observe co-localization of Cy3 fluorescence with GFP (due to lack of Cy3 fluorescence), suggesting that Cy3-DNA alone does not internalize into cells. However, when Cy3-DNA-CNTs are delivered into the leaves, I observe 62% co-localization between the Cy3 and intracellular GFP channels, which suggests efficient internalization of DNA-CNTs into the plant cell cytoplasm (Fig. 8b).

Internalization of DNA-CNTs into mature leaf cells was also confirmed with transmission electron microscopy (TEM) and direct NIR imaging of CNTs inside the leaf tissue by taking advantage of the intrinsic NIR fluorescence of SWCNTs (Fig. 9). NIR imaging of leaves infiltrated with DNA-CNTs reveals that the amount of CNTs per leaf area decreases by approximately 50% over 21 days, probably due to cell division and leaf expansion, and thus CNT dilution. I also assessed whether DNA-PEI-CNTs can internalize into chloroplasts. Interestingly, DNA-PEI-CNTs, which have a positive zeta potential (+32 mV), internalize into extracted chloroplasts. These DNA-PEI-CNT chloroplast internalization results are in agreement with the lipid exchange envelope penetration model, which predicts internalization of nanoparticles with a smallest dimension at or below ~20 nm and with zeta potential values above or below ~+30 mV or ~−30 mV, respectively[107].

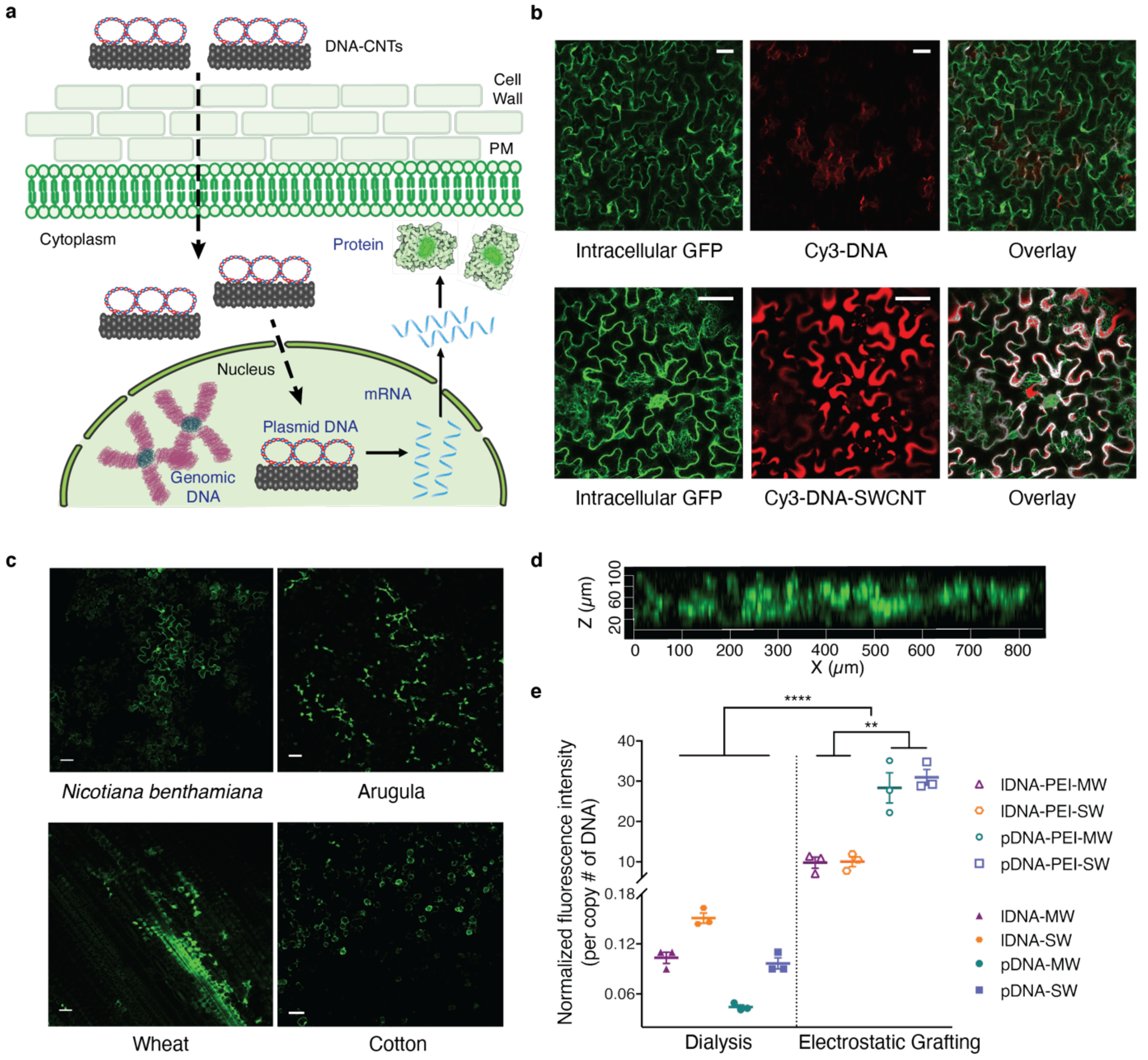

Figure 8. DNA delivery into mature plant leaves with CNTs and subsequent GFP expression.

a, Schematic depicting DNA–CNT trafficking in plant cells and subsequent gene expression (dotted lines represent trafficking steps and the rigid lines represent gene expression steps). PM, plasma membrane. **b**, Nanoparticle internalization into mature plant cells is shown by imaging Cy3-tagged DNA–CNTs with confocal microscopy, compared to a control sample of Cy3-tagged DNA without CNTs, in a transgenic mGFP5 *Nb* plant. **c**, Wild-type *Nb*, arugula, wheat and cotton leaves infiltrated with DNA–CNTs are imaged with confocal microscopy to determine GFP expression levels in the leaf lamina of each plant species. **d**, Z-stack analysis of the fluorescence profile of the DNA–CNT-treated arugula leaf close to the infiltration area. **e**, Quantitative fluorescence intensity analysis of arugula confocal images for all nanomaterial formulations. **P = 0.001 and ****P < 0.0001 in one-way ANOVA. Error bars indicate s.e.m. (n = 3). Scale bars, 50 μm. All experiments were carried out with intact leaves attached to healthy plants.

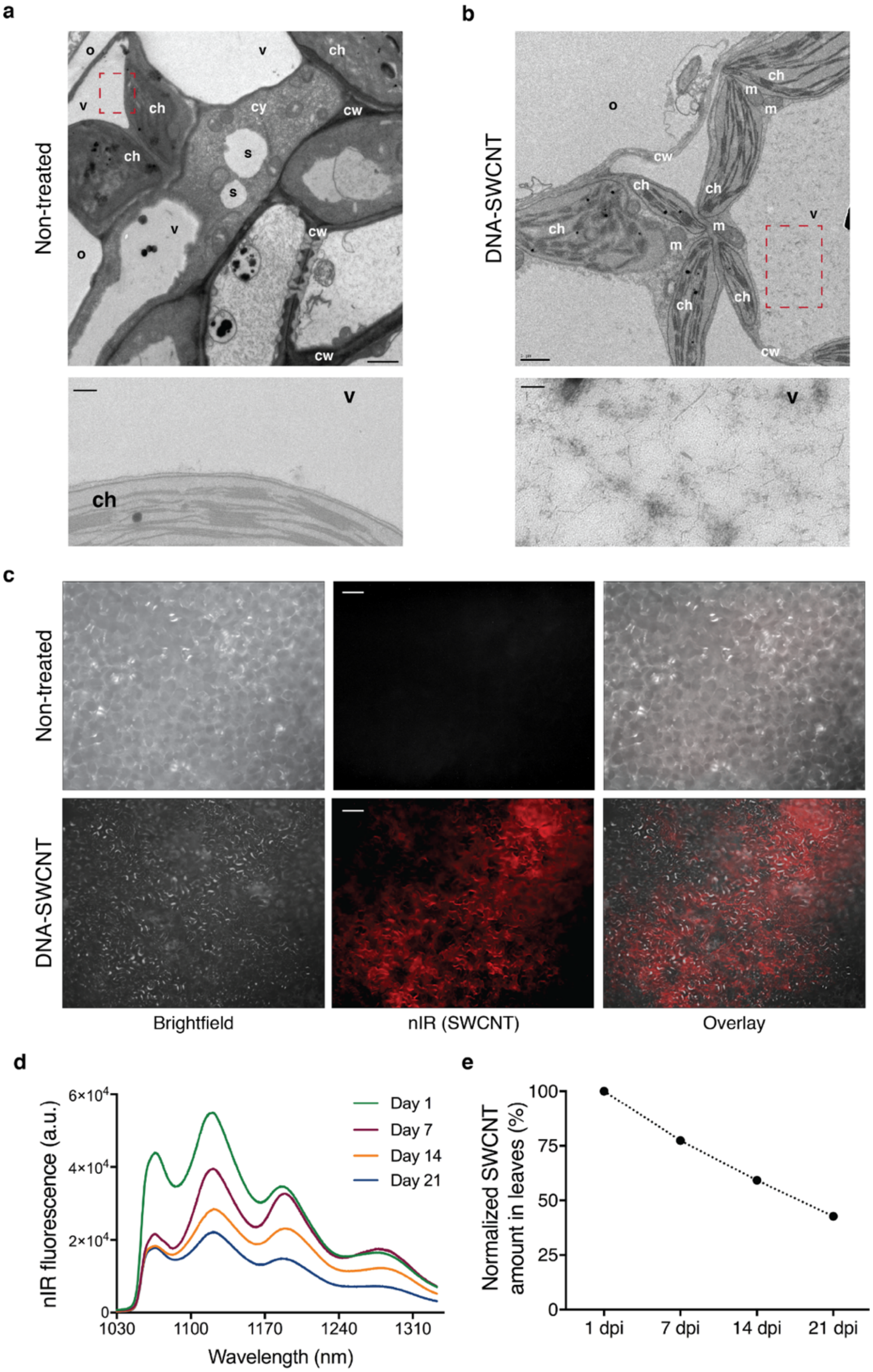

Figure 9. CNT internalization and long-term fate inside plant leaf tissues.

Annotated TEM images of non-treated **a**, and DNA-CNT treated leaves **b**, Nanoparticles are only observed inside the cells of DNA-CNT treated leaves. Scale bar for the full-size image in **a** is 2 µm, and for the zoomed-in image 200 nm. Scale bar for the full-size image in **b** is 1 µm and for the zoomed-in image 100 nm. TEM annotations are o: outside the cell, v: vacuole, ch: chloroplast, cy: cytoplasm, cw: cell wall, s: starch and m: mitochondria. **c**, Near-infrared fluorescence microscopy of DNA-CNTs in mature *Nb* leaves. Plant cell internalization and diffusion of DNA-CNTs is demonstrated *via* near-infrared fluorescence imaging. CNTs are excited with a 350 mW 721 nm laser. Non-treated leaf does not show SWCNT-related near-infrared fluorescence, as expected, whereas the leaf infiltrated with DNA-loaded CNTs demonstrates strong near-infrared fluorescence. Scale bars, 50 µm. **d**, nIR fluorescence spectra of DNA-CNTs inside infiltrated leaves per area 1, 7, 14, and 21-days past infiltration (dpi). **e**, Area under the curve from **d** showing that the amount of CNTs inside the leaf per area decreases gradually from Day 1 to Day 21. All experiments are done with intact leaves attached to healthy plants.

Leaves infiltrated with DNA-CNTs for GFP expression were imaged with confocal microscopy, and expression of GFP was observed in the cells of the leaf lamina 72 h post-infiltration in all plant species tested (*Nb*, arugula, wheat and cotton; Fig. 8c). Z-stack analysis of the fluorescence profile of the DNA-CNT treated leaves shows that GFP fluorescence originates from the full thickness of the leaves, confirming that CNT nanocarriers diffuse and penetrate through the full leaf profile (Fig. 8d). No GFP expression is detected in the leaves when free DNA vectors, PEI-DNA complexes or PEI-CNTs are delivered in control studies (Fig. 10).

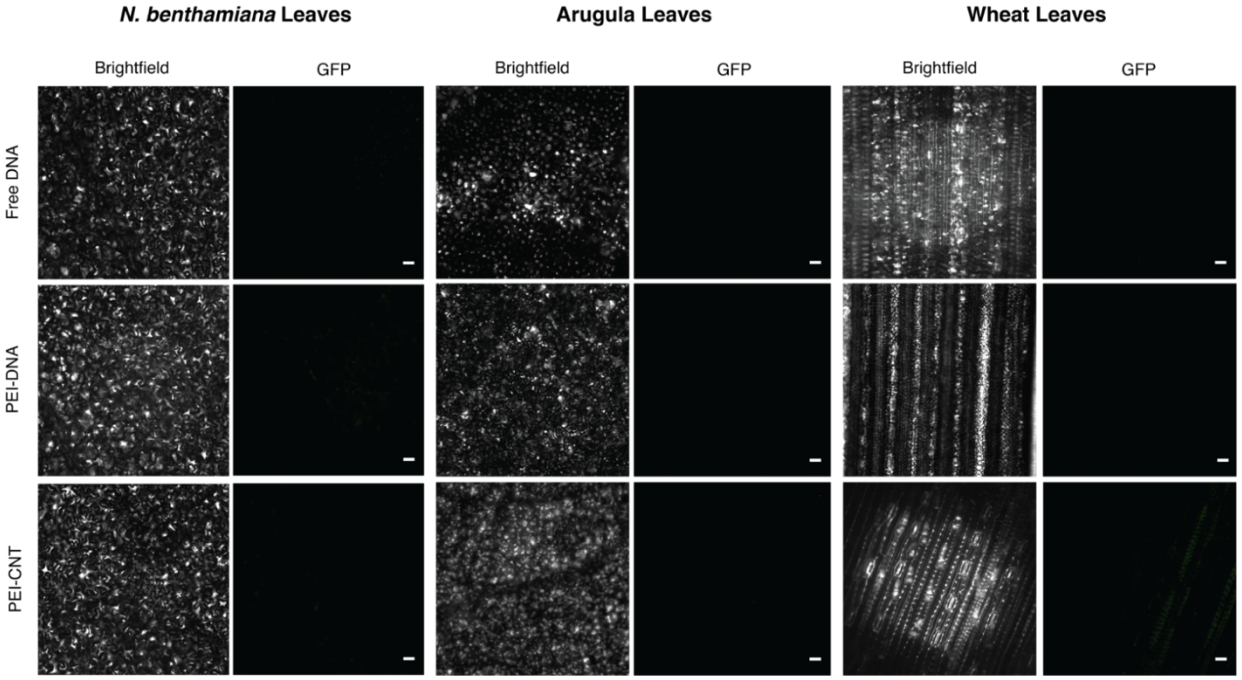

Figure 10. Control studies for DNA-CNT delivery and GFP protein expression in mature *Nicotiana benthamiana*, arugula, and wheat leaves.

When free plasmid DNA, or PEI-DNA, or PEI-CNT is delivered, no GFP expression is detected in any plant species *via* confocal microscopy at 72h post-infiltration, as shown by representative confocal images obtained with the same optical parameters with DNA-CNT induced GFP expression imaging. Scale bars, 50 µm. All experiments are done with intact leaves.

The efficiency of CNT nanocarrier internalization and GFP expression varies substantially for the different nanomaterial formulations I tested. Quantitative fluorescence intensity analysis of confocal images for arugula leaves indicates that GFP expression is significantly higher for DNA-CNTs prepared through electrostatic grafting compared to GFP expression induced by DNA-CNT conjugates prepared *via* π–π grafting with dialysis (Fig. 8e). The most efficient DNA-CNT formulation is plasmid DNA delivered with PEI-functionalized SWCNT (pDNA-PEI-SWCNT), which is over 700 times more efficient than plasmid DNA adsorbed on pristine MWCNT *via* dialysis (pDNA-MWCNT), the least-efficient DNA-CNT formulation. Based on these results, all subsequent mature leaf transformation studies were performed with pDNA-PEI-SWCNTs, unless otherwise noted.

I further demonstrate that CNT-mediated gene expression is transient in mature plant leaves, independent of the plant species. Representative confocal images of pDNA-PEI-CNT infiltrated *Nb* (Fig. 11a), and corresponding quantitative fluorescence intensity analysis of these images demonstrates that the highest GFP fluorescence intensity at day 3 disappears by day 10 (Fig. 11b). Similarly, quantitative PCR (qPCR) analysis of GFP mRNA corroborates the confocal imaging results. For pDNA-PEI-CNT treated *Nb* leaves, I observe an over 7,500-fold GFP mRNA increase at 3 days post-infiltration, which drops to an insignificant twofold mRNA change by day 10 (Fig. 11c), revealing that maximal GFP expression occurs at day 3 with transient expression that lasts through day 10. Similar GFP expression profiles at day 3 and 10 are also verified with arugula, wheat and cotton mature leaves (Fig. 11d). Compared to CNT-mediated expression, however, *Agrobacterium*-mediated GFP expression in mature arugula leaves did not cease at day 10, as shown by confocal imaging (Fig. 11e), GFP fluorescence intensity quantification (Fig. 11f) and qPCR analysis (Fig. 11g), supporting the established concept of plasmid DNA genomic integration with *Agrobacterium*-mediated delivery[115].

These results, both at the mRNA transcript and protein levels, demonstrate that GFP expression is transient and genes delivered into plant cells *via* CNT do not integrate into the plant nuclear genome. I tested the non-integration of plasmid DNA into the plant nuclear genome using droplet digital PCR (ddPCR). ddPCR is a method that allows high-precision and absolute quantification of nucleic acid target sequences[116]. Here, I used ddPCR to determine whether DNA delivered with CNTs integrates into plant genomic DNA and compared the genomic DNA integration rates of CNT and *Agrobacterium*. The ddPCR experiments reveal that there is no transgene integration when DNA is delivered *via* CNTs (Fig. 11h), whereas high-frequency GFP integration events are shown when *Agrobacterium*-mediated delivery is performed (Fig. 11i). I performed experiments with additional ddPCR control samples such as no template control, non-treated leaf and free DNA infiltrated leaf. As expected, amplification of neither EF1 nor GFP genes is observed in the NTC, and amplification of only the EF1 gene is observed in non-treated or free DNA infiltrated leaves. The transient production of GFP in leaves induced by CNT and *Agrobacterium* delivery was quantified 3 days after infiltration. I find that CNTs and *Agrobacterium* delivery produce 13.6 μg and 21.9 μg GFP per gram of fresh weight of leaves, respectively.

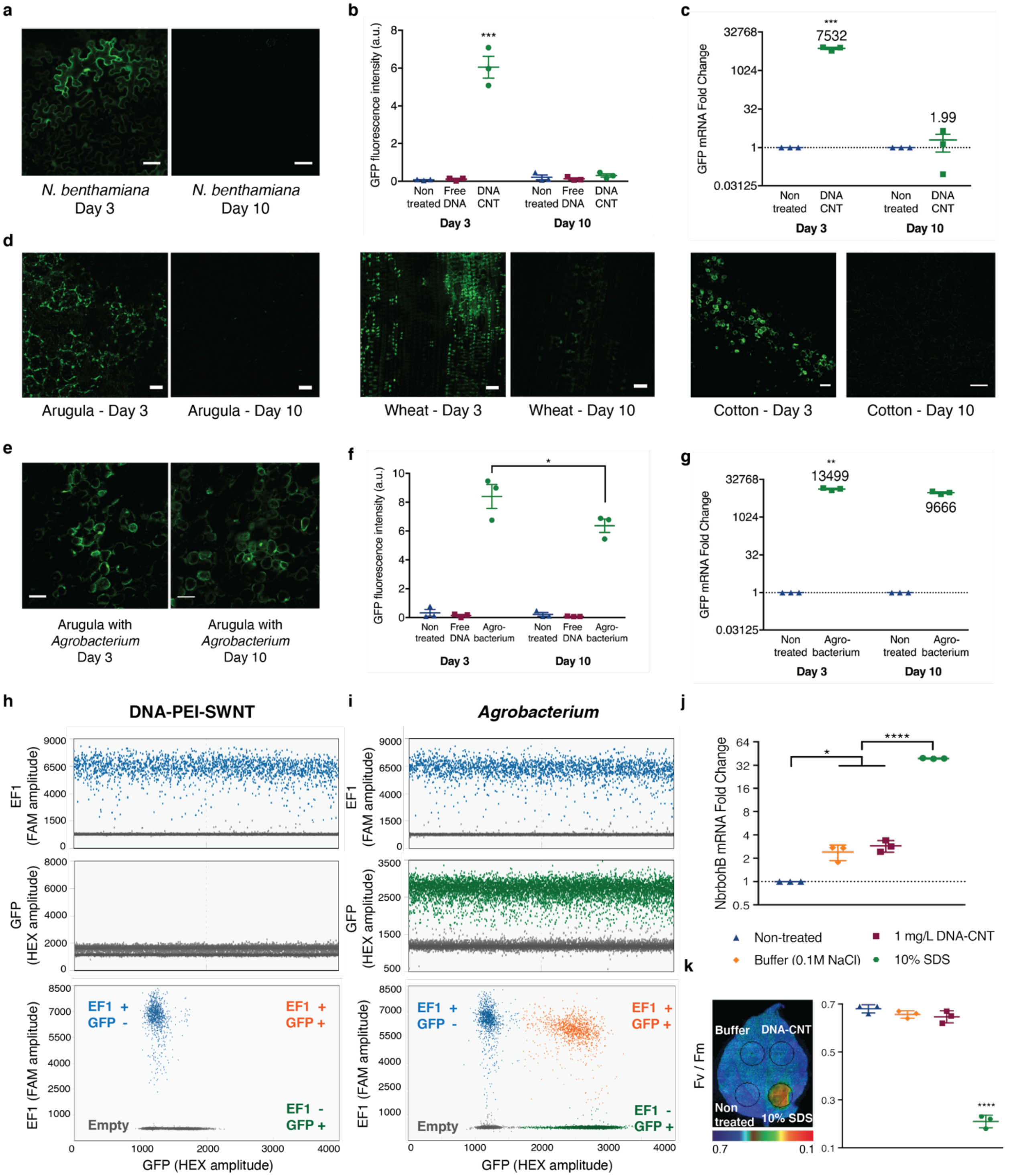

Figure 11. Transient CNT-mediated GFP expression in mature plant leaves and nanoparticle toxicity assessment.

a, Representative confocal microscopy images of pDNA-PEI-CNT-infiltrated mature *Nb* leaves imaged at day 3 and 10. **b**, Quantitative fluorescence intensity analysis of confocal images at 3- and 10-days post-infiltration. ***P = 0.0001 in two-way ANOVA. **c**, qPCR analysis of GFP mRNA expression levels at day 3 and day 10 in pDNA-PEI-CNT-treated *Nb* leaves. ***P = 0.0003 in two-way ANOVA. **d**, Representative confocal microscopy images at day 3 and day 10 in pDNA-PEI-CNT-infiltrated mature arugula, wheat and cotton leaves. **e**, Representative confocal microscopy images of *Agrobacterium*-infiltrated mature *Nb* leaves imaged at day 3 and day 10. Scale bars, 50 μm. **f**, Quantitative fluorescence intensity analysis of *Agrobacterium*-transformed leaves at 3- and 10-days post-infiltration. *P = 0.012 in two-way ANOVA. **g**, qPCR analysis of *Agrobacterium*-transformed leaf at day 3 and day 10. **P =

0.0028 in two-way ANOVA. **h**, ddPCR with FAM and HEX probes of DNA-PEI-CNT-infiltrated *Nb* leaves. **i**, ddPCR results of *Agrobacterium*-infiltrated *Nb* leaves. **j**, qPCR analysis of NbrbohB relative to EF1 to test CNT toxicity. *P = 0.0169 and ****P < 0.0001 in one-way ANOVA. **k**, Quantum yield measurements of photosystem II to test whether CNT-infiltrated leaves have similar photosynthesis quantum yield as control leaves without CNT infiltration. Fv/Fm ratio represents the variable/maximum fluorescence measurement of the Photosystem II quantum efficiency. ****P < 0.0001 in one-way ANOVA. All error bars indicate s.e.m. (n = 3).

2.5. Comparison of CNT-Mediated Delivery with Gene-Gun Method

Biolistic (gene gun-based) DNA delivery is a preferred technique for transformation of plant species that are incompatible with *Agrobacterium*-mediated transformation. In this section, I compared CNT-mediated delivery with biolistic particle DNA delivery by transforming mature arugula true leaves and cotyledons with the same GFP-encoding plasmid using a gene gun. Interestingly, with biolistic transformation, we obtained little GFP expression in arugula true leaves, and also observed sparse GFP expression only in some of the guard cells on the topmost surface of arugula cotyledons through high-pressure condition biolistic delivery (Fig. 12b). Since GFP expression is limited to the topmost layer of the cotyledons, it is likely that biolistic delivery cannot penetrate deep enough in the arugula leaf to enable transformation of sub-cuticle cell types, such as mesophyll cells, even though a wide range of gene gun pressures (up to 900 PSI) were also tested. To my knowledge, biolistic transformation of arugula leaves remains to be shown in the literature. Consequently, we tested the transformation of mature *Nb* plant leaves with biolistic transformation and successfully obtained GFP expression in mesophyll cells, most likely due to the fact that, as a model laboratory plant, *Nb* has a thinner and easy-to-penetrate leaf structure (Fig. 12a). These results demonstrate that depending on the plant species and tissue type, biolistic transformation can result in variable tissue penetration depth and lower expression efficiency compared to the CNT-mediated delivery.

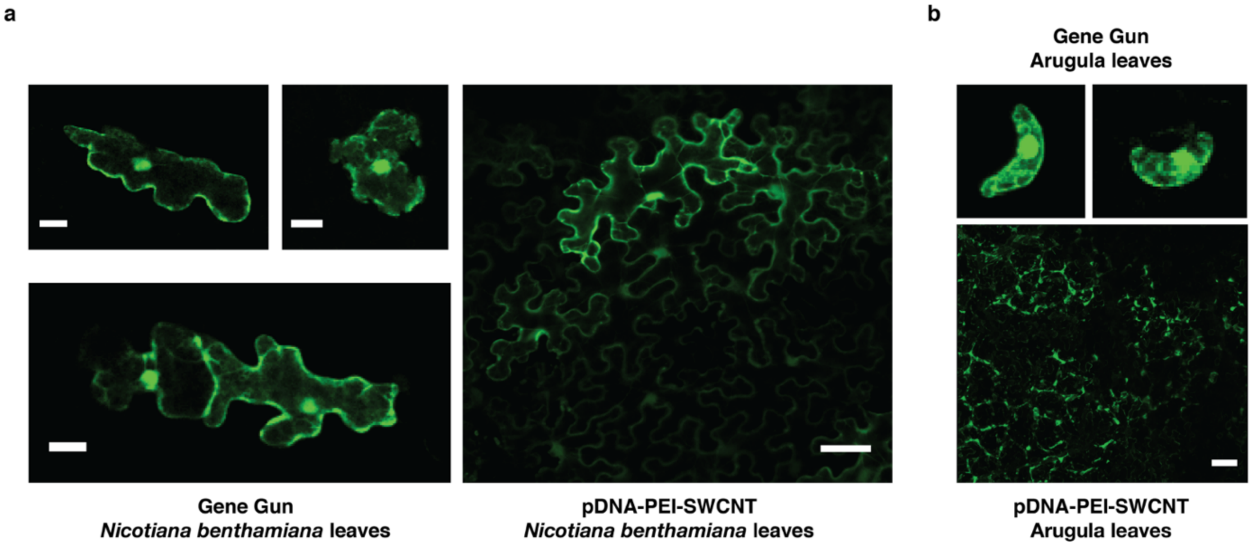

Figure 12. Comparison of CNT-mediated transformation with biolistic (gene gun) based transformation.
a, In *Nicotiana benthamiana* leaves, gene gun-mediated sparse GFP expression is observed in the leaf mesophyll cells, whereas expression was more dispersed when delivered *via* pDNA-PEI-CNTs. **b**, Gene gun-mediated GFP expression is only observed sparsely in the guard cells of arugula cotyledons, and no to little expression is observed in the true arugula leaves (not shown). With pDNA-PEI-CNTs, GFP expression was also more dispersed in true arugula leaves. All scale bars, 20 µm. Gene gun experiments are performed with detached leaves.

2.6. Testing CNT Toxicity and Damage in Plant Leaves

To test CNT nanocarrier biocompatibility, I undertook plant toxicity and tissue damage tests. Specifically, for toxicity analyses, I performed qPCR analysis of respiratory burst oxidase homologue B (NbrbohB) upregulation, a known stress gene representing many different types of stress conditions in *Nb* plants[117]. Quantification of NbrbohB expression shows that DNA-CNT-treated areas do not upregulate NbrbohB compared to adjacent areas within the same leaves treated only with buffer (Fig. 11j). qPCR analysis of NbrbohB expression was also performed for PEI-functionalized CNT infiltrated leaves at short time points (3, 6 and 12 h) and a long time point (14 days). qPCR results show that PEI-CNTs exhibit a twofold upregulation of NbrbohB at 3 h, which returns to nontreated levels by 6 h, and show that there is no long-term toxicity caused by PEI-CNTs as assessed at a longer 14-day time point (Fig. 13d).

Additionally, quantum yield measurements of photosystem II show that DNA-CNT-infiltrated areas in *Nb* leaves have similar photosynthesis quantum yields as control areas within the same leaves that are infiltrated only with buffer (Fig. 11k). Positive controls to induce plant stress for both NbrbohB qPCR and photosystem II quantum yield measurements show clear upregulation of NbrbohB and a significant decrease in photosystem II quantum yield in *Nb*. I also analyzed leaf tissue damage visually and *via* confocal microscopy, which again show no sign of tissue damage in CNT-infiltrated leaves (Fig. 13a, b and c). The results suggest that the CNT-based delivery platform is biocompatible and does not induce toxicity or tissue damage to mature plants with the conditions and concentrations used in the present study. After preparation, PEI-CNT complexes are assumed to be stable for ~1 month at 4°C and can be stored long-term at -20°C by freezing (Fig. 13e and f). I show that freeze-thaw cycles do not affect the colloidal stability of PEI-CNTs, and thawed PEI-CNTs remain active for DNA loading and transformation (Fig. 13f).

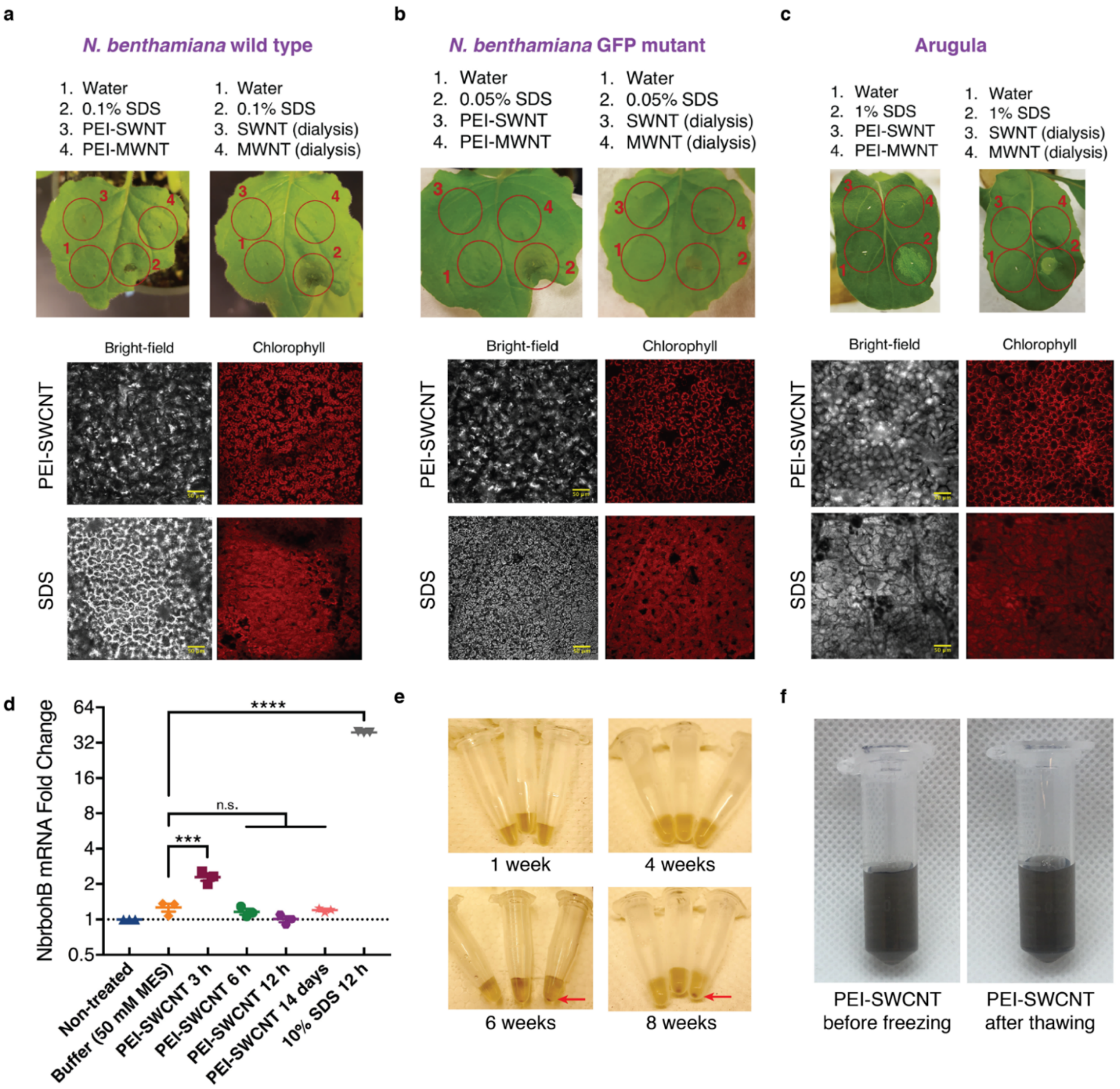

Figure 13. Tissue damage, short and long-term toxicity of PEI-CNTs in leaves and long-term PEI-CNT stability.

a, Tissue damage induced by infiltration of water, SDS, PEI-SWCNT and PEI-MWCNT (electrostatic), and SWCNT and MWCNT (dialysis) samples are tested in mature *Nb* wild type leaves. **b**, mature *Nicotiana benthamiana* GFP mutant leaves and **c**, mature arugula leaves. None of the CNT formulations cause tissue damage compared to water control, and only the positive control SDS infiltrated leaves show significant tissue damage detected by visual observation and by confocal imaging. Scale bars, 50 µm. **d**, NbrbohB stress gene expression levels are measured with qPCR, whereby NbrbohB expression doubles at 3 h but returns to baseline 6 h following infiltration with PEI-CNTs. No long-term toxicity is observed for PEI-CNT infiltrated leaves. **e**, Photos showing the 4˚C stability of pDNA loaded PEI-SWCNTs for more than 4-weeks, and by week 6 some CNT pelleting begins to occur. Red arrows denote the pelleting of CNTs. **f**, PEI-CNTs can be stored longer-term by freezing at -20˚C, and upon thawing PEI-CNTs are stable and remain active for DNA loading and transformation (data not shown). All experiments are done with intact leaves attached to healthy plants.

2.7. Diffusion-Reaction Model of CNT Spatial Distribution Inside a Leaf

After infiltration into the plant leaves, DNA-CNTs diffuse in the extracellular matrix while internalizing into plant cells. Consequently, there is a point where no nanocarrier is left in the extracellular matrix due to the consumption by cells proximal to the DNA-CNT infiltration area. I analyzed and modeled the spatial distribution of nanocarriers inside the leaf with a diffusion-reaction equation in which I implement a first order elementary reaction with a constant rate constant for metabolic consumption of nanocarriers. The model predicts an exponential decay in the concentration of nanocarriers with respect to distance from the infiltration area. To fit this mathematical model to my experimental results, I analyzed the lateral profile of leaf GFP fluorescence expression obtained through confocal imaging as a proxy for nanocarrier diffusivity and obtain good agreement between my diffusion-reaction model and GFP fluorescence localization ($R^2 = 0.996$, Fig. 14).

The most general diffusion-reaction equation to describe the spatial distribution of CNT nanoparticles inside a leaf is:

$$\frac{\partial C}{\partial t} = D\left[\frac{\partial^2 C}{\partial x^2} + \frac{\partial^2 C}{\partial y^2} + \frac{\partial^2 C}{\partial z^2}\right] + F(C) \tag{1}$$

where C is the concentration of CNT nanocarriers carrying DNA or RNA, t is time, x, y, z denotes the distance from the infiltration area, D is the diffusion coefficient, and F(C) is a function for nanocarrier consumption in the leaf.

I assumed the following to simplify the general equation:

1. 1D in Cartesian coordinates
2. Steady-state; $\left.\frac{\partial C}{\partial t}\right|_{ss} = 0$
3. First order elementary reaction with constant rate constant; $F(C) = -kC$

With these assumptions, Equation (1) simplifies to:

$$D\,\frac{\partial^2 C}{\partial x^2} = kC \tag{2}$$

where k is the metabolic consumption rate of the nanocarrier by plant leaf cells.

The boundary conditions are:

$C\,(x = 0) = C_o$	Known infiltration concentration at the infiltration point
$\left.\frac{\partial C}{\partial x}\right|_{L} = 0$	No flux outside the impermeable leaf boundary

The constants k and D are calculated as follows:

$k^{118} = 0.52\ \mathrm{min}^{-1}$
$D^{119} = 0.75\ \mathrm{nm}^2/\mathrm{ns}$

Then, ∝ is defined as square root of the k to D ratio:

$$\propto = \sqrt{\frac{k}{D}} = 3x10^{-6}\ nm^{-1}$$

With these given boundary conditions, solution to Equation (2) is:

$$C(x) = C_0(\cosh \propto x - \tanh \propto L \sinh \propto x) \tag{3}$$

Inserting the constants k and D into the solution, I get:

$$C(x) = C_0(\cosh \propto x - \sinh \propto x) \tag{4}$$

which can be further simplified by using the definition of hyperbolic functions:

$$C(x) = C_0\ e^{-\propto x} \tag{5}$$

The solution for the simplified diffusion-reaction equation is thus an exponential decay function, which suggests that the concentration of the nanocarriers decreases exponentially from the DNA-CNT infiltration area. To fit this mathematical model to the experimental results, I used GFP fluorescence measurements obtained through confocal imaging as a proxy for nanocarrier concentration and internalization into plant cells (Fig. 14).

The fitting results demonstrate good agreement between the model and fluorescence imaging experiments for the exponential decay function solution. The goodness estimates of the fits are 0.9953 and 0.996 for CNTs loaded with linear DNA (lDNA) and plasmid DNA (pDNA), respectively. However, experimental GFP fluorescence data inside the leaves exhibit a stationary phase prior to the exponential decay phase, which I predict occurs due to the fact that closer to the infiltration area, there is a surplus of DNA-CNT conjugates relative to available plant leaf cells. As such, the local concentration of CNTs is higher than can be captured by GFP expression, such that CNT internalization by cells proximal to the infiltration area underestimates the effective concentration of CNT nanocarriers.

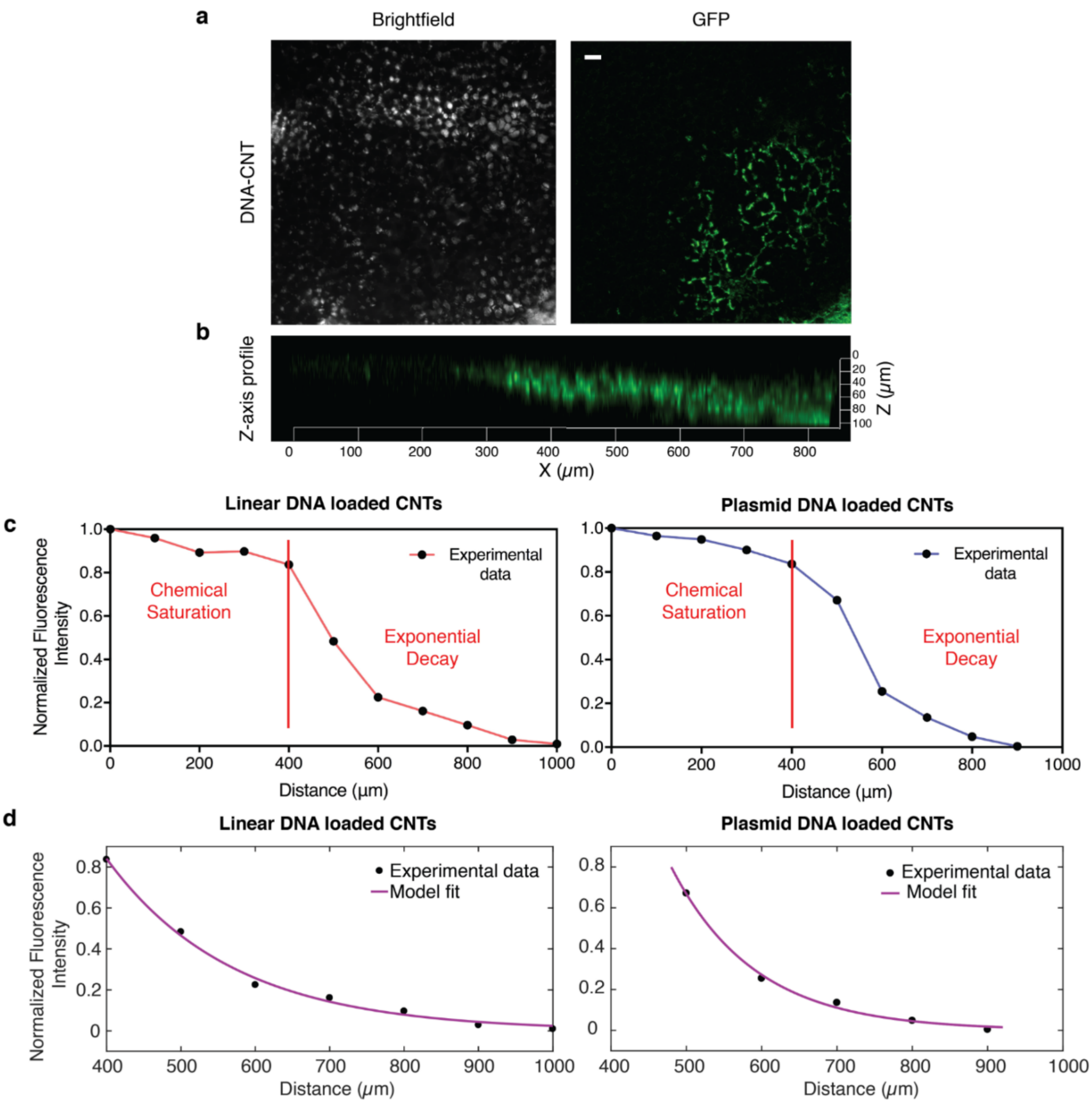

Figure 14. Spatial distribution analysis of CNT nanocarriers inside the plant leaf modeled by a diffusion-reaction equation.
a, Confocal image of a DNA-CNT infiltrated arugula leaf shows the spatial distribution of GFP expression at a field of view farther away from the infiltration area (roughly bottom right corner), showing GFP expression begins to disappear when further from DNA-CNT exposure. Scale bar, 50 μm. **b**, Z-axis profile of the same leaf area demonstrating the z-axis distribution of GFP from the leaf abaxial to adaxial surfaces. **c,** Experimental data obtained from confocal imaging of GFP shows two phases for DNA-CNT diffusion: a stationary chemical saturation phase and an exponential decay phase of GFP fluorescence (Experimental data points are connected for clarity). **d,** Spatial distribution of nanocarriers inside the plant leaf is modeled and plotted with a first order diffusion-reaction equation. The model predicts an exponential decay in the concentration of nanocarriers with respect to the distance from the infiltration area. To fit the mathematical model (purple trace) to the experimental results (black dots), I analyzed the lateral profile of plant leaf GFP fluorescence intensity measurements obtained through confocal imaging as a proxy for nanocarrier diffusivity, and obtained good agreement between the diffusion-reaction model and GFP expression in the leaf tissue ($R^2 = 0.9953$ for plasmid DNA loaded CNTs and $R^2 = 0.996$ for linear DNA loaded CNTs). All experiments are done with intact leaves attached to healthy plants.

2.8. DNA Delivery into Isolated Protoplasts with CNTs

I further investigated the ability of CNT nanocarriers to deliver plasmid DNA and trigger functional gene expression in a different plant system—isolated protoplasts—which are cultured plant cells without cell walls that are used extensively in plant biotechnology. Recently, it has been shown that certain CNT formulations can internalize into plant mesophyll protoplasts[120]. Protoplasts are used to increase the throughput of plant genetic screens and for the synthesis of recombinant proteins, thus benefiting from a facile, passive, high-efficiency and species-independent transformation platform[121]. For this purpose, intact and healthy protoplasts were extracted from arugula leaves through enzymatic cell wall degradation (Fig. 15a) with high efficiency and high yield (10^7 total protoplasts per 10 leaves). Isolated protoplasts were incubated with Cy3-DNA-CNTs and subsequently stained with a nuclear marker, DAPI. Imaging of protoplasts incubated with Cy3-DNA-CNTs confirmed nanomaterial internalization into the protoplast cytoplasm and nucleus, which is absent when Cy3-DNA is delivered without CNTs (Fig. 15b). Nanoparticle internalization into isolated protoplasts was also confirmed through direct NIR imaging of DNA-CNTs. When DNA-CNTs are co-incubated with a protoplast solution, I observe near-infrared (NIR) CNT fluorescence that colocalizes with the bright-field image of the protoplast, confirming internalization.

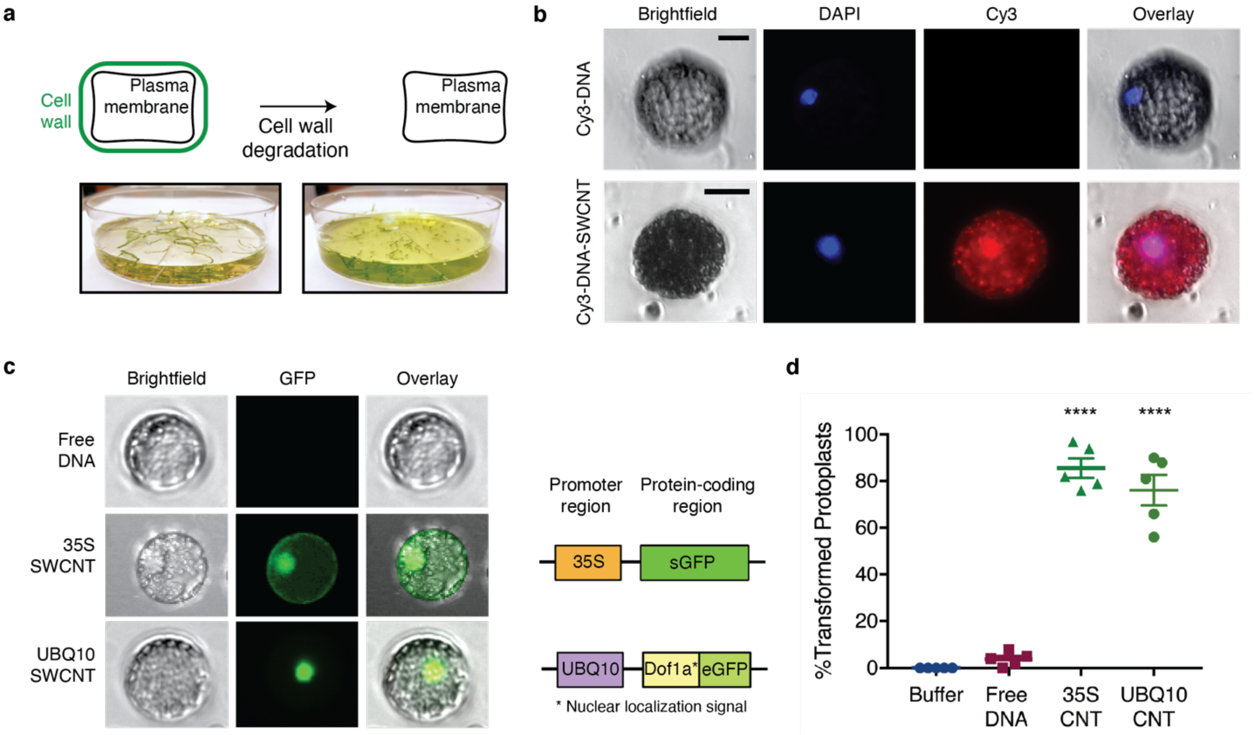

Figure 15. DNA delivery into isolated protoplasts with CNTs and subsequent GFP expression.
a, Intact and healthy protoplast extraction from arugula leaves (intact leaves attached to plants) through enzymatic cell wall degradation. **b**, Verification of nanoparticle internalization into isolated protoplast cytosol and nucleus by imaging the Cy3-DNA-

CNTs after incubation with DAPI-stained protoplasts. Scale bars, 20 µm. **c**, GFP expression imaging of protoplasts incubated with 35S and UBQ10 plasmids carrying DNA-CNTs *via* fluorescence microscopy. Protoplast diameters are ~20 µm. **d**, Percentage of the total isolated protoplasts transformed with 35S-CNTs and UBQ10-CNT after 24 h incubation with plasmid DNA–CNTs. ****P < 0.0001 in one-way ANOVA. Error bars indicate s.e.m. (n = 5).

For gene expression studies, isolated protoplasts were incubated with plasmid DNA-CNTs prepared *via* dialysis, and subsequently imaged with fluorescence microscopy. In addition to the plasmid used in leaf studies (35S-GFP), for protoplast experiments I also used a plasmid that encodes a nuclear localization signal (UBQ10-GFP, Fig. 16), which transports the expressed GFP protein from the cytosol into the nucleus. Protoplasts incubated with both types of DNA-CNT show GFP expression correctly localized in cells, whereas protoplasts incubated with free plasmids without CNTs do not show GFP expression (Fig. 15c). CNT-mediated protoplast transformation efficiencies are 76% and 86% with UBQ10-CNTs and 35S-CNTs, respectively (Fig. 15d). Our earlier work on CNT internalization into extracted chloroplasts suggests that nanoparticle internalization through the lipid bilayer occurs within seconds of CNT exposure[107]. Thus, the CNT-based plasmid DNA delivery platform enables rapid and passive delivery of DNA into protoplasts and transgene expression with high efficiency and no observable adverse effects on protoplast viability.

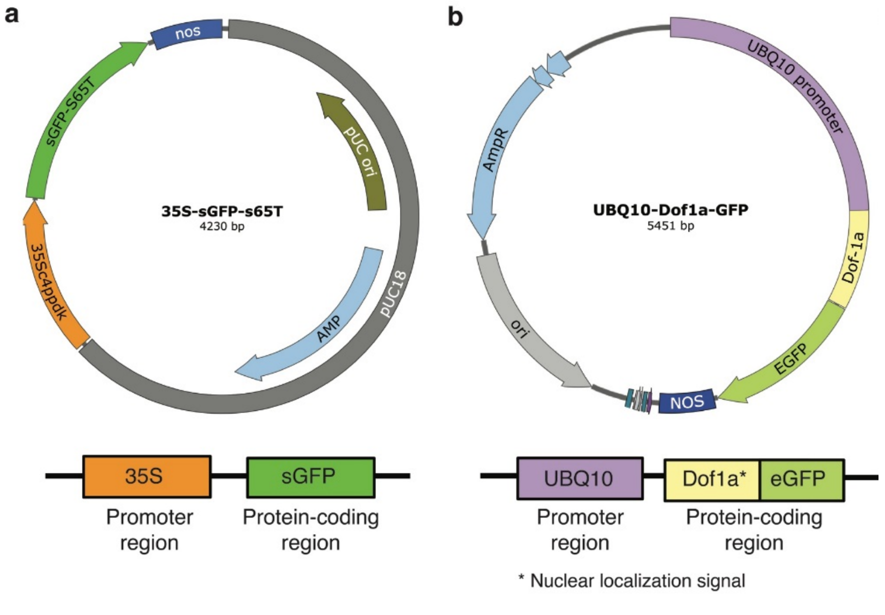

Figure 16. Plasmids used in the current study.

a, Plasmid map for 35S dicot plasmid DNA encoding sGFP-S65T that lacks a nuclear localization signal for the expressed GFP protein. **b**, Plasmid map for UBQ10 dicot plasmid DNA encoding eGFP that contains a nuclear localization signal (Dof1a) for the expressed GFP protein.

2.9. The Effect of CNT Surface Chemistry on Delivery Efficiency

The results suggest that the CNT surface chemistry is an important factor for biomolecule delivery into plant cells. The observed results can be explained by different DNA binding affinities to CNT surfaces in the two DNA grafting methods. The predominant DNA-CNT binding interaction in the case of dialysis is π-π stacking. In contrast, electrostatic attraction between PEI-CNTs and DNA is the predominant binding interaction for the electrostatic grafting method. I propose that the smaller equilibrium dissociation constant[122] and higher binding energy value[123] for electrostatic attraction compared to π-π stacking interactions increase the stability of the DNA-CNT complex as it traverses the cell wall, plasma membrane, and nuclear envelope, thus increasing the delivery efficiency of DNA to the plant cell.

Worthy of note, for electrostatically-loaded DNA, I also observe statistically significantly higher protein expression efficiencies with CNT conjugates loaded with plasmid (pDNA) compared to linear (lDNA) conjugates. I hypothesize that this difference in transformation efficiency is due to the decreased cytosolic degradation rate of pDNA compared to lDNA in eukaryotic cells, as lDNA is prone to degradation by both endo- and exonucleases, while pDNA is only degraded by endonucleases (as it does not contain free ends).

2.10. Additional Considerations for the Use of PEI-CNTs As a Plant Transformation Tool

After preparation, PEI-CNT complexes are stable for at around 1 month at 4°C and can be stored long-term at -20°C by freezing. I show that freeze-thaw cycles do not affect the colloidal stability of PEI-CNTs, and thawed PEI-CNTs remain active for DNA loading and transformation. The 1-month solution-phase stability of PEI-CNT complexes facilitates rapid loading of DNA onto CNTs through a 30-minute co-incubation of DNA vectors with PEI-CNTs. This platform is also scalable and amenable to high throughput applications. The preparation of PEI-CNTs and DNA loading can be scaled by changing the amounts of constituents while keeping their mass ratio constant. Additionally, with CNTs, loading one plasmid *versus* tens of plasmids will approximately take the same amount of time, as the only required step is mixing of plasmids with CNTs. Conversely, if such high-throughput applications are desired with *Agrobacterium* transformation, the researcher first needs to transform *Agro* bacterial strains separately with each plasmid, grow each strain, and activate the T-DNA (3-4 days) before introducing *Agrobacteria* into plants as a mixture of each strain solution.

A simple calculation reveals that this study's CNTs and their necessary chemistries cost less than 3 dollars per infiltration, and do not require the relatively high cost associated with gene gun equipment and gold particles commonly used in biolistic delivery. Here are the details of the calculation given as item cost per infiltration:

CNT	\$0.22
PEI	\$0.01
DNA preparation	\$0.24
All consumables	\$0.29
Utilities	\$0.20
Labor	\$2.00
Total	**\$2.96/infiltration**

The EPA (regulation #40 CFR 721.10929) classifies CNTs under the "Toxic Substances Control Act" as distinct from carbon and graphite on the grounds that sufficient information is known about bulk-sized carbon and graphite, whereas insufficient information is known about these same materials at the nano-scale. This regulation necessitates certain approvals for the synthesis and distribution of CNTs, and it is required to handle all dry CNT materials inside a chemical fume hood with proper protective personal equipment until CNT materials are in solution phase, at which point they may be handled outside a chemical hood.

Specifically, regarding genetic transformation of edible plants with CNTs, I note that the transformed plant material constitutes the experimental generation T_o. Plants genetically edited with CNTs would undergo several generations of progeny production before their seeds are brought to market, and thus edible plants would constitute generations that have never undergone exposure to CNTs.

2.11. Discussion

Genetic engineering of plants may address the crucial challenge of cultivating sufficient food, natural product therapeutics and bioenergy for an increasing global population living under changing climatic conditions. Despite advances in genetic engineering across many biological species, the transport of biomolecules into plant cells remains one of the major limitations for rapid, broadscale and high-throughput implementation of plant genetic engineering, particularly for intact plant tissues and organs. I thus present a nanomaterial-based delivery platform that permits diverse conjugation chemistries to achieve DNA delivery without transgene integration in both model and crop plants, and in both dicot and monocot plants, with high efficiency and without toxicity or tissue damage. In this chapter, I show the development and optimization of dialysis and electrostatic grafting methods for loading DNA plasmids or linear amplicons onto high aspect ratio CNTs. I confirm the feasibility and test the efficacy of this platform by delivering reporter GFP DNA constructs into mature *N. benthamiana*, arugula, wheat and cotton leaves, and arugula protoplasts, and obtain strong expression of a functional transgenic protein.

The nanomaterial-based transient plant transformation approach demonstrated herein is beneficial for plant biotechnology applications where gene expression without transgene integration is desired, and is amenable to multiplexing, whereby multiple gene vectors are to be delivered and tested rapidly in a combinatorial manner and in parallel[124]. This approach may aid high-throughput screening in mature plants so as to rapidly identify genotypes that result in desired phenotypes, mapping and optimization of plant biosynthetic pathways, and maximization of plant-mediated natural product synthesis, most of which currently rely on *Agrobacterium*-mediated transformation[125]. CNT-mediated delivery is well suited for such transient applications as it is easy, cost-effective, nondestructive, fast, species-independent and scalable.

Additionally, global regulatory oversight for genetically modified organisms (GMOs) is motivating the future development of non-integrative and/or DNA-free plant genetic transformation approaches, in which the delivered gene expression is transient and foreign DNA is not integrated into the plant genome[126]. However, the most commonly used tool today for plant genetic transformations – *Agrobacterium*-mediated transformation technology – is unable to perform DNA- and transgene-free editing, and yields random DNA integration. Similarly, DNA delivery methods that utilize a gene gun or other external forces such as vortexing can cause cell damage, which leads to increased rates of transgene integration, possibly due to the over-activation of the endogenous cellular DNA repair mechanisms commonly induced by stress and cell/DNA damage.

Notably, when combined with nuclease-based genome editing cargoes such as zinc finger nucleases (ZFNs), transcription activator-like effector nucleases (TALENs), clustered regularly interspaced short palindromic repeats (CRISPR) from Prevotella and Francisella 1 (Cpf1), and CRISPR associated protein 9, CNTs could enable transient expression of these tools for the production of permanent (stable) edits. As such, CNT-based delivery of these biomolecular cargoes could enable high-efficiency genome modification without transgene integration, thus circumventing strict GMO regulations. This latter application of the presented technology could be particularly beneficial for heterogeneous plant species such as cassava, cacao and sugarcane, in which crossing cannot be used to remove transgenes. Furthermore, CNTs are shown herein to protect DNA cargo against nuclease degradation, a feature of CNT-based delivery that may be extended to the protection of other biological cargoes of interest.

In this study, I have thus developed nanoparticle-based plant transformation biotechnologies that show high-efficiency and species-independent delivery of plasmid DNA and linear amplicons, and transient expression of encoded proteins, which can potentially be used as a transgene-free plant genetic engineering approach when combined with nuclease-based genome editing tools. As such, CNT-based plant transformations are a useful addition to the plant biotechnology toolkit.

2.12. Materials and Methods

Procurement and preparation of chemicals and nanomaterials. Super-purified HiPCO SWCNTs (lot no. HS28–037) were purchased from NanoIntegris, MWCNTs (lot no. R0112) were purchased from NanoLab and both CNT samples were extensively purified before use[127]. Carboxylic acid-functionalized SWCNTs (lot no. MKBX0303V) and MWCNTs (lot no. BCBR9248V) were purchased from Sigma-Aldrich. GFP-encoding dicot plasmids (35S-GFP-NOS and UBQ10-GFP-NOS) were obtained from the Sheen Lab, Harvard Medical School[128]. GFP-encoding monocot plasmid (osACTIN-GFP-NOS) was obtained from the Staskawicz Lab, UC Berkeley. The 35S-GFP-NOS plasmid expresses sGFP-S65T with a 35S promoter, has no subcellular localization signals and is around 4.2 kbp in length. The UBQ10-GFP-NOS plasmid expresses eGFP with a UBQ10 promoter, has a subcellular localization signal for GFP to the nucleus (Dof1a) and is around 5.4 kbp in length. The osACTIN-GFP-NOS plasmid expresses eGFP with an osACTIN monocot promoter, has no subcellular localization signals, and is around 5.2 kbp in length. 20K MWCO dialysis cassettes were purchased from Thermo Scientific. The following chemicals were purchased from Sigma-Aldrich: stains-all dye (95%), SDS (molecular biology grade), sodium chloride, MES hydrate, d-mannitol, calcium chloride dihydrate (suitable for plant cell culture), potassium chloride, magnesium chloride hexahydrate, bovine serum albumin (heat shock fraction), polyethylene glycol (4K) and polyethylenimine (branched, 25K). Cellulase R10 and macerozyme R10 enzymes were purchased from Grainger. Single-stranded DNA (ssDNA) polymers were purchased from IDT and dissolved in 0.1 M NaCl before use. All ddPCR reagents and materials were purchased from Bio-Rad. BSA-biotin and NeutrAvidin were purchased from Sigma-Aldrich and S1 nuclease was purchased from Promega. UltraPure DNase/RNase-free distilled water from Invitrogen was used for qPCR and ddPCR experiments, and EMD Millipore Milli-Q water was used for all other experiments.

Plant growth. Italian arugula (*Eruca sativa*) seeds purchased from Renee's Garden were germinated in SunGro Sunshine LC1 Grower soil mix by planting the seeds half an inch deep into the soil of a standard propagation liner tray (Nursery Supplies). The germinated plants were then moved to a Hydrofarm LED growth chamber (12h light at

~22˚C / 12h dark at 18˚C). Plants were allowed to mature to 3-4 weeks of age within the chamber before experimental use. Wild type *Nb* and transgenic mGFP5 *Nb* seeds obtained from the Staskawicz Lab, UC Berkeley, were germinated and grown in SunGro Sunshine LC1 Grower soil mix for four weeks before experimental in a growth chamber, 12-hour light at 24°C: 12-hour dark at 18°C cycle. Spring wheat (*Triticum aestivum L.*, cv. Fielder) were grown in Supersoil (Rod McClellan Co., South San Francisco, CA, USA) in a Conviron growth chamber with 60% relative humidity, 18-hour light at 24°C: 8-hour dark at 18°C cycle, and 3-4-week-old plants were used for experiments. Cotton seedlings were purchased from Cottonman.com and allowed to mature within the Hydrofarm LED growth chamber (12h light at ~22˚C / 12h dark at 18˚C). All experiments (except gene gun) were done with intact leaves attached to plants, where plants were incubated in the growth chamber until the time of data collection.

SDS-CNT, ssDNA-CNT and Cy3-DNA-CNT preparation. HiPCO SWCNTs (3 mg) were added to 3 ml 2 wt% SDS in water and bath sonicated for 10 min, followed by probe-tip sonication with a 6 mm sonicator tip at 10% amplitude for 30 min in an ice bath (pulse 1 s on/1 s off). The resulting solution was allowed to rest at room temperature for 30 min before centrifugation at 16,100g for 1 h to remove unsuspended SWCNT aggregates and metal catalyst precursor. The concentration of SDS-SWCNTs (supernatant) was measured by recording the SWCNT absorption spectrum with a UV-vis-NIR spectrometer and calculating the SWCNT concentration in mg l^{-1} (absorbance at 632 nm/extinction coefficient of 0.036). The same suspension protocol was applied for MWCNTs, but their concentration was measured using a standard curve as obtained in reference[129].

For toxicity, tissue damage and internalization assays, SWCNTs were suspended in ssDNA polymers with $(GT)_{15}$ or Cy3-tagged $(GT)_{15}$ sequences through probe-tip sonication as previously described[130]. Briefly, ssDNA was dissolved at a concentration of 100 mg ml^{-1} in 0.1 M NaCl. A 20 μl volume of this ssDNA solution was aliquoted into 980 μl 0.1 M NaCl, and 1 mg HiPCO SWCNTs were added. The mixture was bath sonicated for 10 min, followed by probe-tip sonication with a 3 mm tip at 50% amplitude (~7 W) for 30 min in an ice bath. The resulting solution was rested at room temperature for 30 min before centrifugation at 16,100g for 1 h to remove unsuspended SWCNT aggregates and metal catalyst precursor. Unbound (free) ssDNA was removed by spin-filtering (Amicon, 100K) 10–15 times and the concentration of ssDNA-SWCNTs was determined by measuring the SWCNT absorbance at 632 nm.

Direct adsorption of DNA onto CNTs *via* dialysis. SDS-CNT solution containing 1 μg of CNTs, and 10 μg of free plasmid DNA were placed into an accurate pore-sized dialysis cartridge (20 kDa molecular weight cutoff (MWCO), 0.5 ml), that allowed the exit of SDS monomers that desorbed from the CNT surface, while free plasmid DNA suspended the CNTs, which remained inside the dialysis cartridge. If necessary due to volume considerations, 2 wt % SDS was used to fill the additional volume of dialysis cartridge to ensure there was no free air space in the cartridge. After 4 days of dialysis with continuous stirring at room temperature and changing the dialysis buffer (0.1 M NaCl) daily, we obtained a stable suspension of plasmid DNA-conjugated CNTs. The preparation protocol was same for both plasmids and linearized DNA vectors, and for both types of CNT (SWCNTs and MWCNTs). The NIR fluorescence spectra of dialysis-suspended CNTs were obtained through NIR fluorescence microscopy using 721 nm laser excitation and an inverted microscope outfitted with an InGaAs sensor array for imaging.

Electrostatic grafting of DNA onto CNTs. Chemical modification of CNTs to carry positive charge is described elsewhere[131] and was applied here with some modifications. COOH-CNT powder (10 mg) was added to 10 ml water (this could be scaled up or down as desired at 1 mg ml^{-1} concentration). The solution was bath sonicated for 5 min and probe-tip sonicated with a 6 mm tip at 10% amplitude for 30 min on ice. It was rested for 30 min at room temperature and centrifuged at 16,000g for 1 h. Supernatant was taken and the SWCNT concentration was measured *via* absorbance at 632 nm with an extinction coefficient of 0.036 to convert to mg l^{-1}. MWCNT concentration was measured using a standard curve as obtained in reference[129]. The prepared COOH-CNT solution was mixed with PEI at a mass ratio of 1:10 CNT:PEI. The solution was bath sonicated for several minutes, and subsequently heated at 84 °C with stirring for 16 h (the reaction could be scaled up or down as desired by keeping the PEI-to-CNT mass ratio constant). The reaction mixture was subsequently cooled to room temperature and filtered with 0.4 μm and 1 μm Whatman Nucleopore membranes to filter SWCNTs and MWCNTs, respectively. The filtered product was washed vigorously with water 10 times to remove unreacted PEI from the reaction mixture, then dried and collected. Dried product (PEI-CNT) (3 mg) was subsequently suspended in 3 ml water by probe-tip sonication with a 6 mm tip at 10% amplitude for 30 min in an ice bath. The resulting solution was rested at room temperature for 30 min before centrifugation at 16,100g for 1 h to remove unsuspended CNT aggregates. The PEI-CNT solution containing 1 μg of CNTs was added into 1 μg of DNA dropwise, pipetted in and out 10 times, and incubated at room temperature for 30 min (DNA incubation could be scaled up or down by keeping the DNA-to-PEI-CNT mass ratio constant).

Plasmid DNA protection assay. Total proteins (including nucleases) were extracted from wild-type *Nb* leaves by grinding in liquid nitrogen to obtain dry frozen powders. The frozen powders were transferred to a microcentrifuge tube with pre-prepared lysis buffer containing 400 μl of 10 mM Tris/HCl (pH 7.5), 150 mM NaCl, 1 mM EDTA, 0.1% NP-40, 5% glycerol and 1% Cocktail and vortexed briefly to mix well. After lysis at 50 °C for 5 min, the tube was centrifuged at 10,000 r.p.m. for 30 min and the supernatant containing whole proteins was collected in a new tube. Total protein extract was quantified by a Pierce 660 nm protein assay (Thermo, product no. 22660). Free pDNA (5 μg) and 5 μg pDNA on PEI-SWCNTs were each incubated with cell lysate proteins obtained from one *Nb* leaf to mimic the intracellular degradation conditions for 6, 12, 24 and 72 h.

After incubation, all pDNA was desorbed from SWCNTs at 95 °C for 1 h in the presence of 2% SDS and 1.5 M NaCl. Desorbed pDNA and cell lysate-treated free pDNA were run on a 1% agarose gel with pDNA standards of known quantity to measure the intact versus degraded DNA in each sample. DNA amounts on the agarose gel were quantified by using band intensity as a proxy (ImageJ Gel Analyzer) and normalized with the lanes containing known DNA quantities (all agarose gel DNA quantifications were conducted as described here).

AFM characterization. A 3 μl volume of sample was deposited on a freshly cleaved mica surface and left to adsorb on the surface for 5 min. The mica surface was then slowly rinsed with water three times (each time with 10 μl water) to remove the salt. The mica surface was then dried with a mild air stream using an ear-washing bulb and imaged with a MultiMode 8 AFM with NanoScope V Controller (Bruker) in tapping mode in air. All AFM images were analyzed by NanoScope Analysis v1.50.

Infiltration of leaves with CNTs. Healthy and fully developed leaves from arugula (3-4 weeks old), *N. benthamiana* (4 weeks old), wheat (4 weeks old) and cotton (4 weeks old) plants were selected for experiments. A small puncture on the abaxial surface of the arugula and cotton leaf lamina was introduced with a pipette tip, and 100–200 μl of the plasmid DNA-CNT solution (or of any control solution) was infiltrated from the hole with a 1 ml needleless syringe by applying gentle pressure, with caution so as not to damage the leaf. For *Nb* infiltration, a tiny puncture on the abaxial surface of the leaf lamina was introduced with a sharp razor, and 100-200 μl of DNA-CNT solution (or of any control solution) was infiltrated through the puncture with a 1 ml needleless syringe by applying gentle pressure.

TEM sample preparation and imaging. An FEI Tecnai 12 transmission electron microscope with acceleration voltage of 120 kV was used for imaging DNA-SWCNT-infiltrated and non-treated mature plant leaves. Small pieces of leaf were directly cut from the whole leaf. Samples were fixed by 2% glutaraldehyde in 0.1 M sodium cacodylate buffer at pH 7.2, followed by vacuum microwaving to remove air in the vacuoles. Samples were post-fixed with 1% osmium tetroxide in 0.1 M sodium cacodylate buffer at pH 7.2, dehydrated with acetone and transferred to epoxy resin. Finally, epoxy resin-embedded samples were cut with a diamond knife into 70-nm-thin cross-sectioned films using a Reichert-Jung Ultracut E, then transferred onto bare Cu TEM grids for imaging.

Chloroplast extraction and SWCNT internalization imaging. Chloroplasts were extracted from 4-weeks old intact wild type *Nb* leaves in a sucrose buffer: 28 mM Na_2HPO_4, 22 mM KH_2PO_4, 2.5 mM $MgCl_2$, 400 mM sucrose and 10 mM KCl at pH=7.3. All buffers and materials were previously cooled to 4˚C and all centrifugation steps were performed at 4˚C. Central veins of *Nb* leaves were removed with a sharp razor blade and leaves were grounded in food processor without the buffer. 5 grams of ground leaves were added to 40 mL cold sucrose buffer and homogenized in mortar and pestle. Ground liquid was poured over 4 layers of cheesecloth and centrifuged at 4000 rpm for 20 min. Supernatant was discarded and the crude chloroplast pellet was resuspended in 5 mL cold sucrose buffer. The solution was centrifuged again at 4000 rpm for 20 min, and the pellet was resuspended in 5 mL cold sucrose buffer. In 2 separate 15 ml falcon tubes, 80%, 60%, 40% and 20% (v/v) Percoll and sucrose buffer are gently combined from bottom to top. 2.5 ml of each fraction is added starting with 80% and ~3 ml of chloroplast solution was gently added to the top of each tube. The gradients were centrifuged at 4000 rpm for 20 min and the dark chloroplast bands in the middle were gently removed with a pipette and combined. 5 mL cold sucrose buffer was added, and the solution was centrifuged at 4000 rpm for 20 min. Chloroplasts were pelleted at the bottom and 3 mL sucrose buffer was added for the subsequent experiments. Chloroplast suspension was kept in fridge at 4 ˚C and avoided exposure to light.

Cy3-DNA-SWCNT or ssDNA-SWCNT solutions (at a DNA concentration of 200 nM) were added to 100 µl of extracted chloroplasts, chloroplasts were pelleted after 4 hours of incubation at room temperature, and the supernatant solution was replaced to fresh sucrose buffer without SWCNTs prior to imaging either with fluorescence microscope for Cy3-DNA tracking or nIR microscope for SWCNT tracking in extracted chloroplasts, respectively.

Imaging of infiltrated leaves for internalization and GFP expression. After infiltration, plants with attached infiltrated leaves were left in the plant growth chamber to allow for internalization for 6 h and imaged with either a NIR microscope to track SWCNTs or with a confocal microscope to track Cy3-tagged DNA-SWCNTs in the leaves. For GFP expression and transience studies, infiltrated leaves were imaged after 3 and 10 days with a confocal microscope. For wheat leaf infiltrations, a sharp razor blade was used to produce a small puncture on the abaxial surface of 3- to 4-week-old plant leaves, and 100-200 µl of the plasmid DNA-CNT solution (or of any control solution) was infiltrated with a 1 ml needless syringe. Plants were returned to the growth chamber and imaged with a confocal microscope after 3- and 10-days post infiltration.

Quantitative fluorescence intensity analysis of GFP gene expression. DNA-CNT-infiltrated plant leaves were prepared for confocal imaging 72 h post infiltration by cutting a small leaf section of the infiltrated leaf tissue and inserting the tissue section between a glass slide and coverslip of #1 thickness. A 100 µl volume of water was added between the glass slide and coverslip to keep the leaves hydrated during imaging. A Zeiss LSM 710 confocal microscope was used to image the plant tissue with 488 nm laser excitation and with a GFP filter cube. GFP gene expression images were obtained at ×10 and ×20 magnification. Confocal image data were analyzed to quantify GFP expression across samples. For each sample, three biological replicates (three infiltrations into three different plants) were performed, and for each biological replicate, 15 technical replicates (15 nonoverlapping confocal fields of view from each leaf) were collected. Each field of view was analyzed with custom ImageJ analysis to quantify the GFP fluorescence intensity value for that field of view, and all 15 fields of view were then averaged to obtain a mean fluorescence intensity value for that sample. The same protocol was repeated for all three biological replicates per sample, and averaged again for a final fluorescence intensity value, which correlates with the GFP expression produced by that sample.

qPCR experiments for gene expression. Two-step qPCR was performed to quantify GFP gene expression in wild-type *Nb* plants with the following commercially available kits: RNeasy plant mini kit (QIAGEN) for total RNA extraction from leaves, iScript cDNA synthesis kit (Bio-Rad) to reverse transcribe total RNA into cDNA, and PowerUp SYBR green master mix (Applied Biosystems) for qPCR. The target gene in our qPCR was GFP, and the reference gene was elongation factor 1 (EF1). The GFP primers used are: forward 5′-CGCCGAGGTGAAGTT-3′; reverse 5′-GTGGCTGTTGTAGTTGTAC-3′. Primers for EF1 are: forward 5′-TGGTGTCCTCAAGCCTGGTATGGTTGT-3′; reverse 5′-ACGCTTGAGATCCTTAACCGCAACATTCTT-3′. An annealing temperature of 60 °C was used for qPCR, which we ran for 40 cycles. qPCR data were analyzed by the ddCt method[132] to obtain the normalized GFP gene expression fold change with respect to the EF1 housekeeping gene and control sample. For each sample, qPCR was performed as three technical replicates (three reactions from the same isolated RNA batch), and the entire experiment consisting of independent infiltrations and RNA extractions from different plants was repeated three times (three biological replicates).

***Agrobacterium*-mediated transformation.** *Agrobacterium tumefaciens* strain GV3101 was used for genetic transformation of *Nb* and arugula leaves, and as a positive control in ddPCR experiments. To generate the *Agrobacterium*-binary construct, the DNA fragment containing 35S-GFP-NOS were excised from the plasmid 35sC4PPDKsGFPTYG with the restriction enzymes XhoI and EcoRI and cloned into an entry cloned digested with the same restriction enzymes. The 35S-GFP-NOS entry clone was recombined into the *Agrobacterium* destination vector pPZP2017. *Agrobacterium* suspensions (OD600 = 0.4) were infiltrated into *Nb* and arugula leaves of 3-4-week-old plants using a 1-ml needleless syringe. Plants were returned to the growth chamber and imaged after 3 and 10 days-post-infiltration and used in ddPCR experiments 14-days post-infiltration.

Biolistic delivery of plasmid DNA. *Nb* and arugula seeds were sterilized in solution (20% bleach) for 30 minutes under gentle agitation, then washed three times with sterile water, plated on ½ strength Murashige and Skoog (MS) medium, stratified for 2 days at 4˚C before transferring to a 26˚C incubator with 16-hour light: 8-hour dark cycle for growth. 3-wk-old leaves were placed onto semi-solid pre-shooting media [4.43 g/L of MS basal medium and vitamins; 36.43 g/L of mannitol; 36.43 g/L of sorbitol; 0.30g of casein enzymatic hydrolysate; 0.5 g/L of L-proline 2 mL/L of 2,4-D (1 mg/ml); pH 5.8; 3.5 g/L of Phytagel] in a 1.5-inch diameter circle in the center of the plate to facilitate bombardment and incubated at 25˚C for 4 hours in the dark. 35S-GFP DNA plasmid was coated onto 0.6 µm gold nanoparticles (Bio-Rad): 1 mg of gold particles were mixed with 30 µl of DNA construct (0.17 µg/µl), 25 µl of 5.0 M $CaCl_2$ and 20 µl of 0.1 M spermidine and incubated on ice for 10 min. DNA-coated gold particles were collected at 14,000 rpm for 1 min, and the pellet was rinsed with 1 mL of absolute alcohol, resuspended in 85 µl ethanol, and then immediately loaded onto the center of a macrocarrier (5 µl each) and allowed to air dry. Biolistic bombardment was performed using a PDS1000/He particle bombardment system (Bio-Rad) with a target distance of 6.0 cm and a rupture pressure of 900 PSI. After bombardment, leaves were transferred to MS solid medium and imaged at 3 and 10 days-post-bombardment.

Droplet Digital PCR (ddPCR) experiments. Genomic DNA (gDNA) was extracted from leaves, 14 days after the treatment with pDNA-PEI-SWCNTs and *Agrobacterium*, *via* CTAB extraction. Briefly, 200 mg leaf tissue was ground in liquid nitrogen with a mortar and pestle, and the leaf powder was transferred into 600 µl CTAB buffer (10 g CTAB, 50 mL 1 M Tris-HCl pH 8, 20 mL 0.5M EDTA pH 8, 140 mL 5 M NaCl and 5 g PVP). The mixture was vortexed well and incubated at 65˚C for 45 minutes. 600 µl chloroform: isopropanol (39:1) was added to mixture and vortexed well. The mixture was centrifuged at 18,000g for 10 minutes and the upper phase was transferred into a new microcentrifuge tube. 600 µl isopropanol was added to the new tube, incubated 5 minutes at room temperature, and then mixed softly. The mixture was centrifuged at 18,000g for 10 minutes. The supernatant (isopropanol) was removed and 100 µl 70% ethanol was added. The mixture was centrifuged at 18,000g for 10 minutes. The supernatant (ethanol) was removed as much as possible and the tube was left to dry at 37˚C for 30 minutes. The gDNA pellet was resuspended in 200 µl autoclaved MilliQ water and the concentration and purity were measured by Nanodrop. All gDNA samples were digested overnight with HindIII-HF in CutSmart buffer. 2 µg gDNA was digested with 20U enzyme in a 50 µl reaction volume for 16 hours at 37˚C. Note that the restriction enzyme was selected so as not cut inside the reference or target gene. We have confirmed that the extracted genomic DNA does not contain any of the infiltrated plasmid DNA *via* several measures. First, 14-days incubation is assumed to be long enough for plasmid DNA to degrade inside the cells. Second, plasmid DNA is not present in any of the agarose gels we have run. Last, all samples were treated the same and if there was any plasmid DNA left at the time of PCR, it would be present not only in the *Agrobacterium* sample, but in all samples (which is not the case, as controls and DNA-PEI-SWCNT samples did not show any amplification with PCR).

ddPCR was performed *via* probe chemistry in a duplex assay for reference EF1 and target GFP genes. The GFP probe (5′-TGCCGTCCTCCTTGAAGTCG-3′) was labeled with HEX at 5′, Iowa Black Hole Quencher at the 3′ end and with an internal ZEN quencher 9 nucleotides away from the 5′ end. The EF1 probe (5′-AGGTCTACCAACCTTGACTGGT-3′) was labeled with FAM at the 5′end, with Iowa Black Hole Quencher at the 3′ end, and with internal ZEN quencher 9 nucleotides away from the 5′ end. Primers used for GFP gene: 5′-GACTTCTTCAAGTCCGCCAT-3′ and 5′-CGTTGTGGCTGTTGTAGTTG-3′, primers used for EF1 gene: 5′-TCCAAGGCTAGGTATGATGA-3′ and 5′-GGGCTCATTAATCTGGTCAA-3′. 20X probe-primer mixes (18 μM PCR primers (each), 5 μM probe) were prepared for both genes.

ddPCR reaction mixes were prepared according to the instructions in ddPCR Supermix for Probes (No dUTP) #1863024 kit. For each sample, we prepared 10 wells, each containing 100 ng digested gDNA, so that a total of 1μg DNA was screened for transgene integration for each sample. Droplets were generated with a QX200 droplet generator right after the ddPCR reaction mixes were prepared. 20 μL of each sample mastermix was transferred to the sample row and 70 μL droplet generation oil was transferred to the oil row in the droplet generation cartridge. After the droplets were generated, 40 μL of droplets were transferred to a new 96-well plate and the plate was sealed for 5 s at 180°C in plate sealer. The PCR was run in a deep-well thermal cycler with the following PCR program: enzyme activation 95˚C 10 min, denaturation 94˚C 30 sec (40X), annealing/extension 60˚C 1 min (40X), stabilization 98˚C 10 min, and hold 4˚C. The fluorescence of the droplets was measured 4 hours after PCR (kept in the dark and at 4˚C) with a QX200 droplet reader, and the results were analyzed with the Bio-Rad Quantasoft Pro Software.

Quantification of GFP protein amount in leaves. Month-old *Nb* leaves were infiltrated with either pDNA-PEI-SWCNTs or *Agrobacterium* solutions. Three days post-infiltration, leaves were harvested, weighed, then frozen and ground in liquid nitrogen to obtain powder. The powder was placed in a liquid nitrogen-cooled tube to which 350 μL of lysis buffer containing 10 mM Tris/HCl (pH 7.5), 150 mM NaCl, 1 mM EDTA, 0.1% NP-40, 5% glycerol, and 1% Cocktail was added. The tube was immediately vortexed for 2-3 seconds before being placed on ice while other samples were similarly harvested. All tubes were incubated in a 50˚C water bath for 3 minutes, then centrifuged at 16,000 g for 40 minutes. The supernatant containing proteins were then transferred to a fresh tube.

A GFP-Trap (ChromoTek GFP-Trap_A) was used to purify and concentrate GFP present in the supernatant. For each sample, 25 μL of GFP-Trap beads was pipetted into ice-cold dilution buffer composed of 10mM Tris/HCl (pH 7.5), 150 mM NaCl and 0.5 mM EDTA. The beads were centrifuged at 2,500 g for 2 min at 4oC and the supernatant was discarded. This was then repeated twice. The beads were added to the supernatant along with 300 μL dilution buffer, and the tube placed on a tube rotator for 1 hour at 4˚C. Samples were centrifuged at 2,500 g for 2 min at 4˚C with the supernatant discarded. Then, 500 μL ice-cold dilution buffer was added to each sample, which was again centrifuged at 2,500 g for 2 min at 4˚C with the supernatant discarded three times. The bound GFP was eluted by constant mixing with 50 μL 0.2M glycine at pH 2.5 for 30 s followed by centrifugation. The supernatant was transferred to a fresh tube and 5 μL 1M Tris Base pH 10.4 added for neutralization. The protein elution step was executed twice to obtain two tubes of approximately 55 μL each per sample.

A Qubit Protein Assay Kit (Invitrogen) was used to quantify the mass of GFP eluted. Briefly, 20 μL of eluted protein was added to 180 μL Qubit Working Solution. The samples were vortexed for 3 seconds and incubated at room temperature for 15 minutes. Standard calibrations and measurements were collected *via* a Qubit 4 Fluorometer.

Plant toxicity analysis. To test for plant stress and toxicity, the expression level of an oxidative stress gene (NbRbohB) in *Nb* leaves was measured through qPCR with the following primers: forward 5′-TTTCTCTGAGGTTTGCCAGCCACCACCTAA-3′; reverse 5′-GCCTTCATGTTGTTGACAATGTCTTTAACA-3′. EF1 was again measured as a housekeeping gene with the same primer set as described above. An annealing temperature of 60 °C was used for qPCR, which was run for 40 cycles, and the ddCt method was used to obtain the normalized NbRbohB expression fold change with respect to the EF1 housekeeping gene and control sample. This toxicity qPCR assay was carried out both for ssDNA-SWCNTs and pDNA-PEI-SWCNTs in triplicate independent experiments.

As an additional toxicity assay, the Fv/Fm ratio, representing the variable/maximum fluorescence measurement of the photosystem II quantum efficiency of infiltrated *Nb* leaves were measured with an Imaging-PAM Maxi fluorimeter (Walz). A singular leaf was infiltrated from the abaxial surface, in three distinct locations within the same leaf, with buffer (0.1 M NaCl), 1 mg/l DNA-SWCNTs or 10% SDS (positive control for toxicity). The fourth quadrant of the leaf was left unperturbed. The triply infiltrated leaf was subsequently incubated for 24 h without further perturbation. Subsequently, the infiltrated leaf was dark-adapted for 15-30 min and chlorophyll fluorescence-related parameters were measured with the Imaging-PAM Maxi fluorimeter to calculate the Fv/Fm ratio, which is commonly used to test for plant stress.

Protoplast isolation from E. sativa leaves. Protoplasts were isolated from arugula and *Nb* leaves as described in reference[128] with some modifications. Briefly, thinly cut leaf strips were immersed in 20 ml of enzyme solution (consisting of cellulase and macerozyme), vacuum infiltrated for an hour in the dark using a desiccator, and further incubated at 37 °C for 3 h in the dark without stirring. Undigested leaf tissue was removed by filtration with a 75 μm nylon mesh, and the flow-through was centrifuged at 200 g for 3 min to pellet the protoplasts in a round-bottomed tube. Pelleted protoplasts were resuspended in 0.4 M mannitol solution (containing 15 mM $MgCl_2$ and 4 mM MES) with a pH of 5.7, which has similar osmolarity and pH to the protoplasts. Isolated protoplasts can be kept viable on ice for over 24 h. However, we used only freshly isolated protoplasts for all internalization and gene expression studies.

Cy3-DNA-SWCNT and ssDNA-SWCNT internalization by protoplasts. A 200 μl volume of the 3×10^5 cells ml^{-1} protoplast solution was mixed with Cy3-DNA-SWCNT solution containing 200 nM DNA and incubated at room temperature for 4 h. The supernatant containing excess free Cy3-DNA-SWCNT was removed without disturbing the protoplast pellet. The protoplasts were immediately resuspended in 200 μl of MMg solution (0.4 M mannitol, 15 mM $MgCl_2$, and 4 mM MES, pH 5.7). A 200 μl volume of the protoplast solution was transferred to a poly-l-lysine-coated microwell dish and the protoplasts were allowed to settle at room temperature for 1 h. Immediately before imaging, 150 μl of the sample was removed from the microwell dish and DAPI was added at a final concentration of 2 μg ml^{-1} to stain protoplast nuclei for 5-10 min. Cy3 and DAPI fluorescence were imaged with a fluorescence microscope, and images were overlaid in ImageJ for co-localization analysis.

Similarly, 200 μl of the 3×10^5 cells ml^{-1} protoplast suspension was mixed with 48 μl of 15.5 mg l^{-1} ssDNA-SWCNT. The samples were tapped lightly every 15 min to encourage mixing and prevent protoplasts from settling at the bottom of the tube. Samples were incubated for 9 h at room temperature. The same sample preparation steps for imaging as used in "Cy3-DNA-SWCNT and ssDNA-SWCNT internalization by protoplasts" were followed, and all NIR images were captured using a custom-built near-infrared inverted microscope equipped with a Raptor Ninox VIS-SWIR 640 camera. Bright-field images were captured with a 100 ms exposure time. Near-infrared images were captured using a 720 nm excitation laser with a 200 ms exposure time and with a 1,070 nm long-pass filter to avoid chlorophyll autofluorescence.

Protoplast transformation with DNA-SWCNTs prepared *via* dialysis. A 100 μl volume (~2 × 10^4) of isolated protoplasts in mannitol solution was added to 10 μg DNA containing DNA-SWCNT dialysis solution, or for the control sample only 10 μg plasmid DNA and mixed well by gently tapping the tube. The mixture was incubated at room temperature for 1 h, and subsequently centrifuged at 200 g for 3 min to pellet protoplasts. Protoplasts were resuspended in 1 ml of 0.5 M mannitol solution (containing 4 mM MES and 20 mM KCl at pH 5.7) in a non-culture treated 6-well plate (Corning) for 24 h in the dark. Protoplasts settled at the bottom of the well plate. Fluorescence microscopy was performed through the well plate to image the protoplasts and to measure GFP expression for quantification of transformation efficiency.

Single molecule TIRF to image DNA protection by SWCNTs. The sequence of DNA used for this assay is the same as that used in co-localization experiments, $(GT)_{15}$. While Cy3 was used for co-localization assays in planta, the Cy5 fluorophore was selected for the TIRF assay due to lower levels of background noise in the collection region. 10 µM 3′ labelled Cy5 DNA was added to an equal mass of HiPCO SWCNT. The suspension and clearing of unbound DNA followed the same protocol as described in SDS-CNT, ssDNA-CNT and Cy3-DNA-CNT preparation. The positive control comprised of 5′ labelled biotin with a Cy5 fluorophore on the 3′ end.

6-channel µ-slides (ibidi, µ-Slide VI 0.5 Glass Bottom) were used for single-molecule TIRF microscopy. The slides were initially washed by pipetting 100 µL of 100 mM NaCl solutions in nuclease-free water filtered with a sterile 0.2 µm syringe filter into one reservoir and removing 60 µL the other end, leaving just enough solution to fully wet the channel. Each subsequent step involved depositing the desired solution volume into the reservoir and removing the equivalent volume from the other end of the channel. 50 µL of 0.25 mg/mL BSA-Biotin was added to coat the surface of the glass slide for 5 minutes. Next, 50 µL of 0.05 mg/mL NeutrAvidin was added, followed by 50 µL of 1.0 mg/L DNA-loaded SWCNT. For the positive control, 50 µL of 100 pM biotinylated Cy5-DNA was added in place of DNA-loaded SWCNT. The addition of each component comprised of a 5-minute incubation period, followed by gently flushing the channel with 50 µL of NaCl solution to remove unbound entities. Each channel was exposed to 50 µL of 2.8 U/µL S1 Nuclease for 30 minutes at room temperature. The reaction was stopped by rinsing the channel with 1 mM ATP solution to inactivate the nuclease. To minimize disturbance of bound DNA or DNA-SWCNT, no imaging buffer was used; each field of view obtained was ensured to not have been imaged previously.

Following slide preparation and immobilized procedure as outlined above, we obtain a surface coverage of ~ 300-400 fluorescent molecules of DNA-loaded SWCNT for each field of view, imaged with a 642 nm laser line, collected with a 655 LP filter, with a 1000 ms exposure time and an EMCCD gain of 300 under TIRF microscopy (Zeiss ELYRA PS.1).

CHAPTER 3. CARBON NANOTUBES DELIVER RNA TO INTACT PLANT CELLS FOR EFFICIENT GENE KNOCKDOWN

3.1. Summary

Post-transcriptional gene silencing (PTGS) is a powerful tool to understand and control plant metabolic pathways, which is central to plant biotechnology. PTGS is commonly accomplished through delivery of small interfering RNA (siRNA) into cells. Standard plant siRNA delivery methods (*Agrobacterium* and viruses) involve coding siRNA into DNA vectors and are only tractable for certain plant species. In this chapter, I develop a nanotube-based platform for direct delivery of siRNA and show high silencing efficiency in intact plant cells. I demonstrate that nanotubes successfully deliver siRNA and silence endogenous genes owing to effective intracellular delivery and nanotube-induced protection of siRNA from nuclease degradation. This chapter establishes that nanotubes could enable a myriad of plant biotechnology applications that rely on RNA delivery to intact cells.

3.2. Introduction

Plants are central in providing over 25% of our most clinically-relevant drugs, are at the core of our sustainability efforts, and will benefit from genetic engineering to feed our growing population in the midst of climate change. Plant biotechnology is currently limited by the cost, ease, and throughput of methods for probing plant genetics, and by the complexity of plant biosynthetic pathways. Consequently, less than a dozen complete biosynthetic pathways are known for plant natural products that have been reconstituted heterologously, compared to the ~1000 known biosynthetic pathways in bacteria and fungi[125]. RNA interference (RNAi) is sequence-specific inhibition of gene expression at the messenger RNA (mRNA) level and can either consist of transcriptional gene silencing (TGS) or post-transcriptional gene silencing (PTGS). In PTGS, small RNA molecules – micro (miRNA) or small interfering (siRNA) – direct enzyme complexes to degrade mRNA molecules, hence suppress their activity by preventing translation.

PTGS has shown to be a prominent tool in plants for genotype-phenotype mapping[133], discovery of new biosynthetic pathways[134], increased production of valuable small molecules[135],understanding the functions of genes and proteins[136], and to confer resistance to plant diseases[137]. One common way of utilizing PTGS in plants is to directly deliver siRNA molecules into cells. However, plants have a cell wall which presents a barrier to exogenous biomolecule delivery, whereby the plant cell wall size exclusion limit is ~ 5-20 nm[61]. Consequently, viral vectors combined with *Agrobacterium* *tumefaciens* delivery is the preferred method to deliver siRNA into intact plant cells. Viral vectors present the advantage of directly and strongly expressing the siRNA without relying on plant transformation, however, most viruses are limited in their host range [51], often do not result in uniform silencing of the gene, and thus levels of silencing can vary between plants and experiments[138], and might inadvertently result in the suppression of non-target genes. *Agrobacterium*-mediated delivery, similarly, is also limited to use in certain plant species, often yields random DNA integration that can adversely and unpredictably affect the cell operation[139], results in constitutive expression of siRNA thus limiting temporal control over gene silencing, and can be difficult to scale or multiplex for high-throughput or multi-gene target applications, respectively[97].

While nanomaterial-mediated delivery of RNA and therapeutics has been extensively explored in animals, its potential for plant systems remains understudied. Polymeric nanoparticles have shown promise for siRNA delivery to cell wall-free plant protoplasts, but polymeric nanoparticles have not been shown to traverse the cell wall for gene silencing in intact plant cells[51]. A recent study has shown that clay nanosheets can facilitate delivery of pathogen-specific double-stranded RNA into intact plant cells for virus resistance[106]. Topical application of clay nanosheets enabled silencing of homologous RNA to provide sustained 20-day viral protection on the leaf surface. Clay nanosheet platform is a promising use of nanoparticles for delivery of RNAi into plants, paving the way towards future developments in plant bionanotechnology. For many applications, particularly biosynthetic pathway mapping, direct and strong but also transient gene silencing is desired within all cellular layers of plant leaves whilst also mitigating against RNA degradation.

In this chapter, I demonstrate the delivery of siRNA into intact cells of plant leaves using high-aspect-ratio one dimensional carbon nanomaterials: single-walled carbon nanotubes (SWNTs). Prior usage of SWNTs in plant systems is limited to studies of SWNT biocompatibility[107], sensing of small molecules[108], and for delivery of plasmid DNA for genetic transformations[42]. To-date, there has yet to be a nanoparticle-based delivery platform for siRNA molecules into intact plant cells. Herein, I develop a SWNT-based siRNA delivery platform for the efficient silencing of an endogenous *Nicotiana benthamiana* gene in plant leaves. I show that SWNTs enable passive delivery (without external mechanical aid) and fluorescent tracking of siRNA molecules in plant tissues. SWNTs present a non-toxic platform for siRNA delivery that uses a minimal siRNA dose to achieve silencing for up to 7 days, whereby silencing can be sustained upon re-infiltration of the siRNA-SWNT dose. With SWNT-mediated siRNA delivery, I achieve 95% gene silencing efficiency at the mRNA level and show a significant delay in siRNA nuclease degradation in cells, and also at the single-molecule level, through protection by SWNTs.

3.3. Preparation and Characterization of siRNA-SWNTs

In this chapter, I aim to validate SWNTs as a passive and effective siRNA delivery and gene silencing platform for use in intact cells of mature plants. To this end, I aim to silence GFP transgene expression in transgenic mGFP5 *Nicotiana benthamiana* (*Nb*) plants by delivering siRNA molecules into leaves with SWNT nanocarriers, and also demonstrate silencing of an endogenous plant gene, ROQ1. mGFP5 *Nb* plants constitutively express GFP targeted to the ER under the control of the Cauliflower mosaic virus 35S promoter. I tested two separate siRNA sequences (a-siRNA and b-siRNA) that target two slightly different regions of the mGFP5 gene for GFP silencing (Fig. 17a).

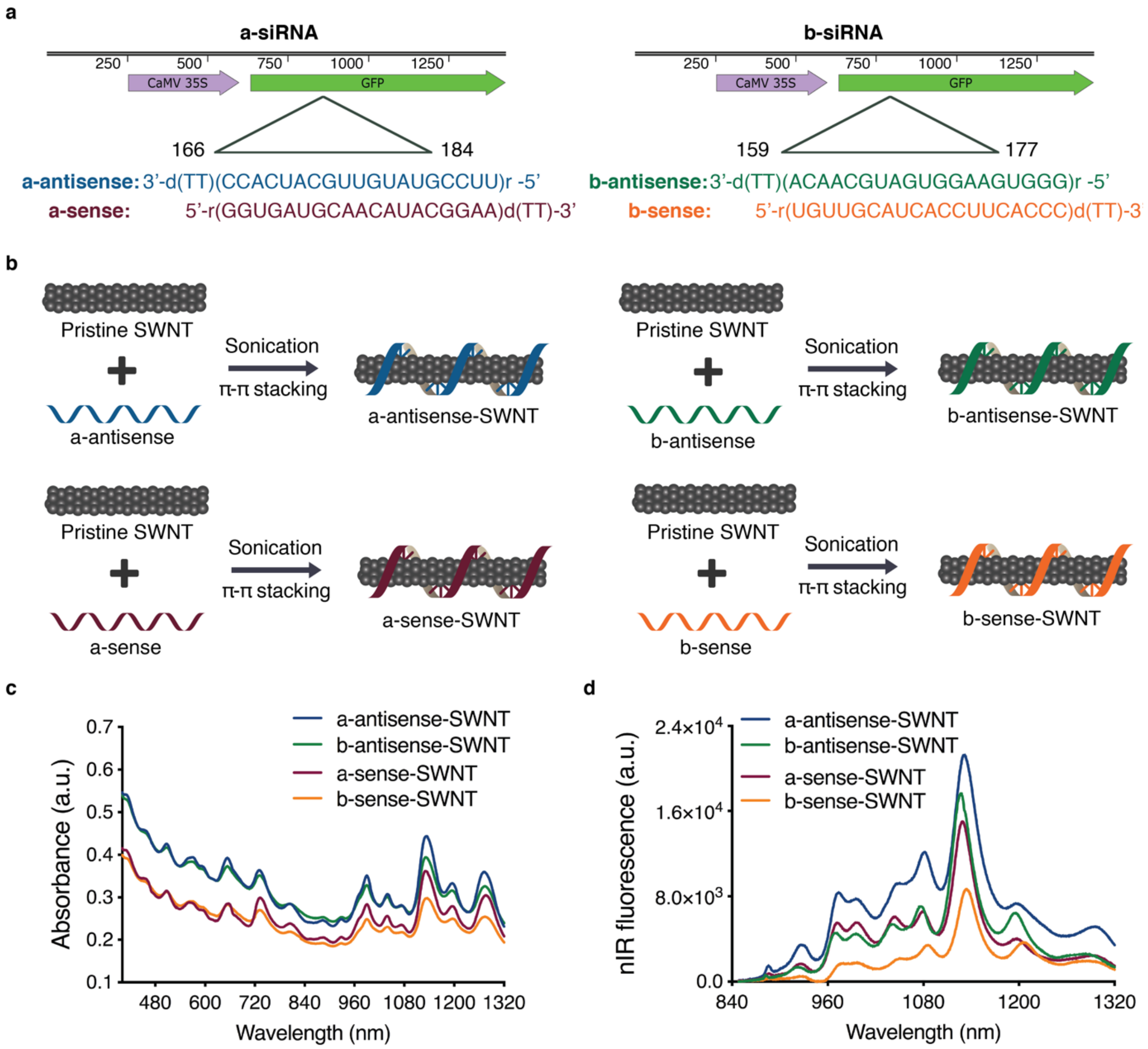

Figure 17. siRNA-SWNT preparation and characterization.

a, Two sets of siRNA sequences targeting the GFP gene of transgenic mGFP5 *Nicotiana benthamiana* were separately tested in this study. Sequences on the left were chosen from Tang *et al.*[140] and sequences on the right were designed specifically for this study. **b**, Suspension of pristine SWNTs with sense and antisense single-stranded RNA sequences *via* probe-tip sonication. **c**, Absorbance spectra of all RNA-SWNT suspensions. **d**, nIR spectra of all RNA-SWNT suspensions.

Loading of siRNA on SWNTs was accomplished by probe-tip sonication of each siRNA single-strand (sense, and separately antisense) with pristine SWNTs for both a-siRNA and b-siRNA sequences (Fig. 17b). With this method, sense and antisense strands of siRNA were non-covalently adsorbed on SWNTs *via* π-π stacking of RNA nitrogen bases with the π bonds of sp^2-hybridized carbons in SWNTs. The adsorption of RNA on SWNTs was confirmed for each sequence (a-antisense-SWNT, a-sense-SWNT, b-antisense-SWNT and b-sense SWNT) through the emergence of characteristic peaks in the individually-suspended SWNT absorbance (Fig. 17c) and nIR fluorescence emission spectra (Fig. 17d). I hypothesize and later verify that upon infiltration of an equimolar mixture of sense and antisense suspended SWNTs, these complementary siRNA strands desorb from the SWNT surface and hybridize to each other inside plant cells to form the active double-stranded siRNA silencing complex.

As a negative control for all siRNA silencing studies, I used SWNTs suspended with a non-targeting scrambled RNA sequence (s-RNA-SWNT), which is not complementary to the mGFP5 mRNA. Successful suspension of SWNTs with non-targeting RNA sense and antisense strands was confirmed by absorbance and fluorescence spectra of individually suspended s-RNA-SWNTs (Fig. 18a-c). Furthermore, AFM characterization of single-stranded RNA (ssRNA) suspended SWNTs reveals an average ssRNA-SWNT conjugate length of 776.6 nm and an average conjugate height of 1.567 nm (Fig. 18d).

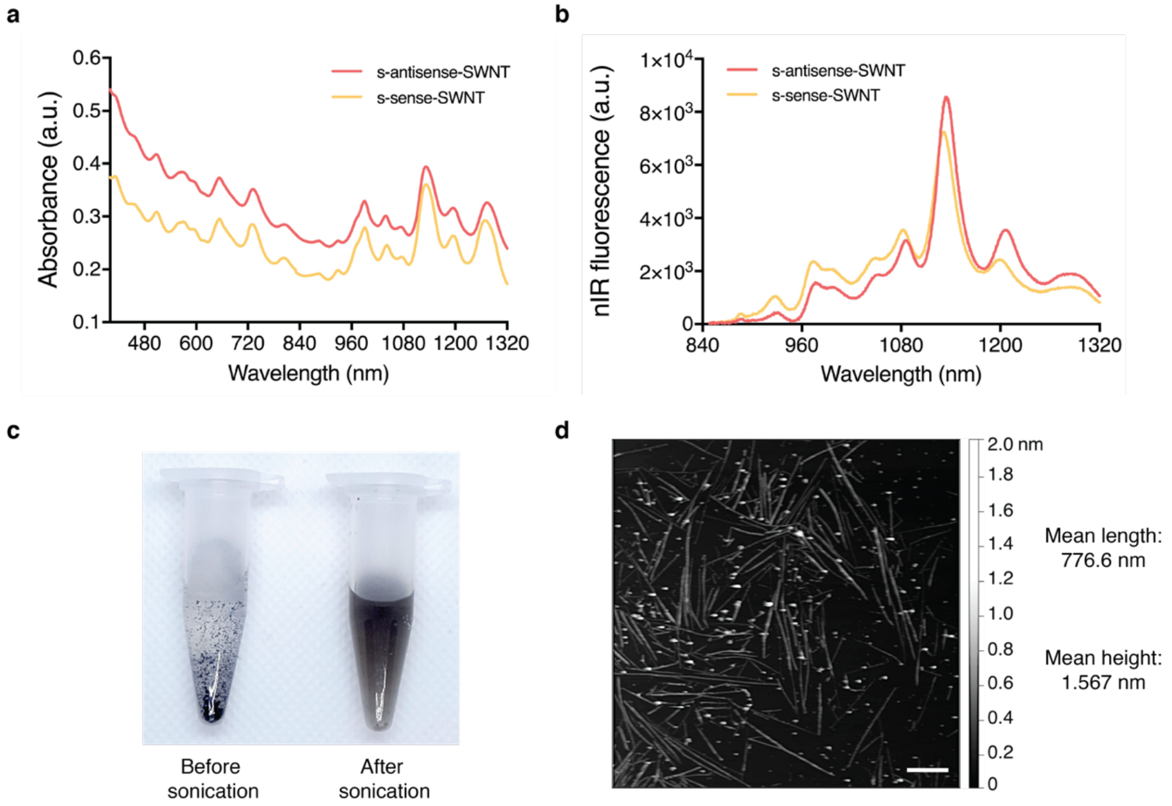

Figure 18. Non-targeting s-RNA-SWNT suspension characterization and AFM imaging.

a, Absorbance spectra of s-antisense-SWNT and s-sense-SWNT suspensions. **b**, Near-infrared (nIR) fluorescence spectra of s-antisense-SWNT and s-sense-SWNT suspensions. **c**, Photo on the left showing RNA SWNT mixture before probe-tip sonication where unsuspended SWNTs aggregate due to van der Waals and hydrophobic interactions between SWNTs, and photo on the right showing homogenous dark-colored individually suspended RNA-SWNT solution that is colloidally stable following probe-tip sonication. **d**, Representative AFM image of an ssRNA-SWNT suspension. Scale bar, 100 nm. Mean length of RNA-SWNTs is 776.6 nm (st. dev. 163 nm) and mean height is 1.567 nm (st. dev. 0.38 nm) for N = 25 SWNTs.

3.4. Internalization of siRNA-SWNTs into Mature Plant Leaves

I first tested the internalization of ssRNA-SWNTs into intact mGFP5 *Nb* leaf cells. All internalization studies were performed with a-antisense-SWNT suspension as a representative strand to demonstrate the internalization ability of single-stranded RNA loaded SWNTs into intact walled plant leaf cells. Cy3 fluorophore-tagged RNA-SWNTs (100 nM siRNA and 2 mg/L SWNTs) and Cy3 tagged free RNA (100 nM) solutions were introduced into the intact plant leaves by infiltrating the abaxial surface of the leaf lamina with a needleless syringe (Fig. 19a). Following 6 hours of incubation, infiltrated mGFP5 *Nb* leaves were imaged with confocal microscopy to quantify Cy3 fluorescence inside leaf cells and in the extracellular area. Leaves infiltrated with Cy3-RNA-SWNTs showed a high degree of co-localization (70% ± 8%, mean ± SD) between the intracellular (cytosolic) GFP and Cy3 fluorescence originating from the nanocarriers, which confirms efficient internalization of RNA-SWNTs into intact cells (Fig. 19b). Conversely, leaves infiltrated with Cy3-RNA show minimal co-localization between the GFP and Cy3 channels (12% ± 10%, mean ± SD), and Cy3 fluorescence is observed mostly around the guard cells, suggesting free RNA is not able to internalize into intact plant cells efficiently (Fig. 19b). To note, a typical plant cell contains an organelle called the vacuole which performs many functions in plants and is filled with water, thus occupying ~80% of the cell volume. Therefore, fluorescence localized in the cytoplasm follows the cytosolic cell contour shape.

To investigate the effect of SWNT length on the cell internalization efficiency, I prepared short SWNTs through excessive probe-tip sonication. AFM images revealed that these short SWNTs have an average length of 250 nm; they are significantly shorter than SWNTs obtained with regular preparation (776 nm). I then loaded these short SWNTs with Cy3-RNA as before and checked internalization efficiency into GFP benthamiana cells with confocal microscopy. Interestingly and unexpectedly, I found that short SWNTs have lower plant cell internalization efficiency compared to the longer ones, shown by respective average co-localization percentages of 47% and 70% (Fig. 19b and 20b).

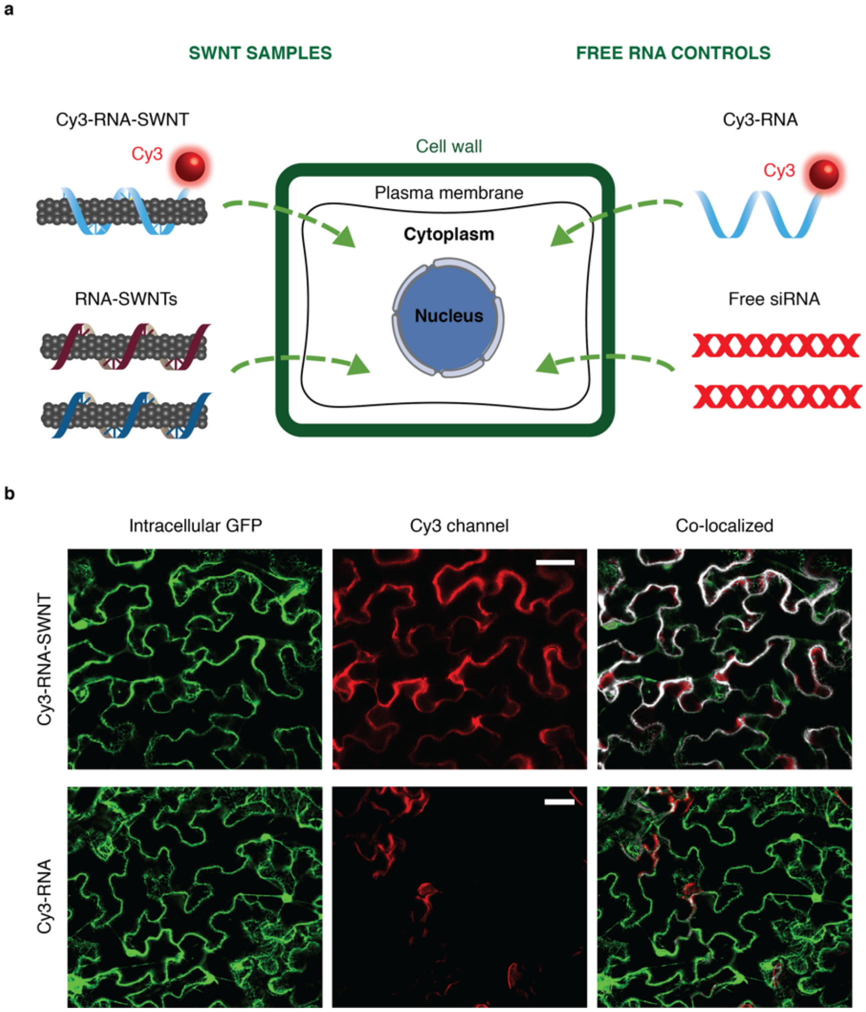

Figure 19. ssRNA-SWNT internalization into transgenic mGFP5 *Nicotiana benthamiana* leaves.

a, Schematic showing samples tested for internalization into mGFP5 *Nb* leaves (Cy3-tagged RNA-SWNTs and Cy3-tagged free RNA as a control), and samples subsequently tested for silencing of a constitutively expressed GFP gene (RNA-SWNTs and free siRNA as a control). **b**, Representative confocal images of Cy3-RNA-SWNT and Cy3-RNA infiltrated *Nb* leaves; intracellular GFP (green), Cy3 (red) and co-localization (white) channels. All scale bars are 20 μm.

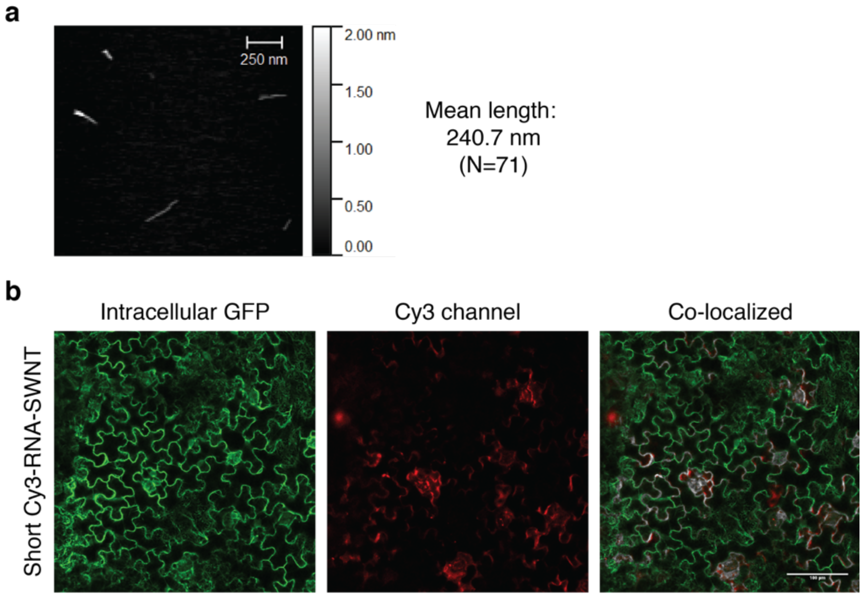

Figure 20. Short Cy3-RNA-SWNTs and their internalization efficiency analysis.

a, Representative AFM image showing shortened SWNTs with an average length of ~250 nm. **b**, Representative short Cy3-RNA-SWNT infiltrated *Nb* leaf confocal image showing 47% co-localization percentage of intracellular GFP with Cy3 fluorescence.

In addition to confocal imaging of fluorophore tagged ssRNA-SWNTs, I verified internalization of SWNT nanocarriers into intact leaf cells by leveraging the intrinsic SWNT nIR fluorescence. mGFP5 *Nb* leaves were infiltrated with ssRNA-SWNTs or free RNA without a fluorophore (Fig. 19a). Following 6 hours of incubation, I imaged the infiltrated leaves with a custom-built nIR microscope equipped with a Raptor Ninox VIS-SWIR 640 camera, a 721 nm SWNT excitation laser, and a white lamp and appropriate filters to image GFP. In leaves infiltrated with ssRNA-SWNTs, commensurate with Cy3-tagged confocal imaging results, I observe a high degree of co-localization between intracellular GFP and the nIR fluorescence of SWNTs (Fig. 21a), further substantiating efficient internalization of SWNTs into intact plant cells. No co-localization was observed in leaves treated with unlabeled free RNA. The internalization of SWNT nanocarriers into plant cells is also supported by the nIR fluorescence spectra of ssRNA-SWNTs. Compared to as-prepared ssRNA-SWNTs, the nIR fluorescence spectra of ssRNA-SWNTs infiltrated into leaves shows a 6-nm solvatochromic shift, and a relative change in intensity of small bandgap nanotubes upon cell membrane crossing (Fig. 21b). These differences in SWNT nIR spectra upon infiltration into leaves are possibly the result of the local dielectric environment change and exposure to intracellular biomolecules.

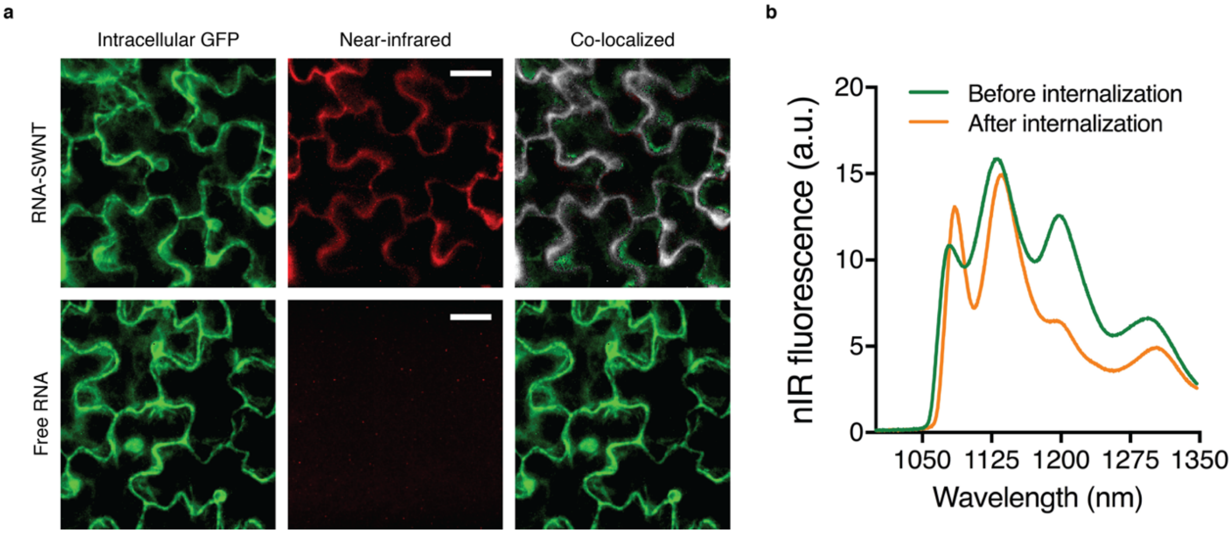

Figure 21. nIR imaging shows internalization of RNA-SWNT suspensions into mGFP5 *Nicotiana benthamiana* leaves.
a, Top row: RNA-SWNT infiltrated *Nb* leaf images showing high co-localization efficiency of intracellular GFP with intrinsic nIR SWNT fluorescence. Bottom row: Free RNA infiltrated *Nb* leaf images showing no co-localization of free RNA inside cells. Scale bars are 20 μm. **b**, nIR fluorescence spectra of RNA-SWNTs before and after internalization into leaf cells. Spectra were obtained with a 1050-nm long pass filter to avoid the autofluorescence of chlorophyll from leaves.

3.5. Thermodynamic Analysis of RNA Desorption and Hybridization

After confirming that ssRNA adsorbed SWNTs can efficiently be uptaken by plant cells, we analyzed the thermodynamics of sense and antisense strand desorption from the SWNT surface, and their subsequent propensities for hybridization in the extracellular and intracellular conditions. According to our analysis, in the *in vitro* and extracellular area of the leaf tissue, sense and antisense strand desorption from the SWNT surface and hybridization is not thermodynamically favorable (ΔG>0), due to a high free energy cost of bare SWNTs in an aqueous environment (Fig. 22a). This unfavorable RNA desorption energy facilitates maintenance of intact RNA-SWNT conjugates in the extracellular environment until RNA-SWNTs enter cells. Once intracellular, sense and antisense strand desorption from the SWNT surface and hybridization is thermodynamically favorable (ΔG<0) because intracellular proteins, lipids, and other membrane and cytosolic biomolecules can occupy the SWNT surface and lower the associated free energy costs of RNA desorption (Fig. 22b).

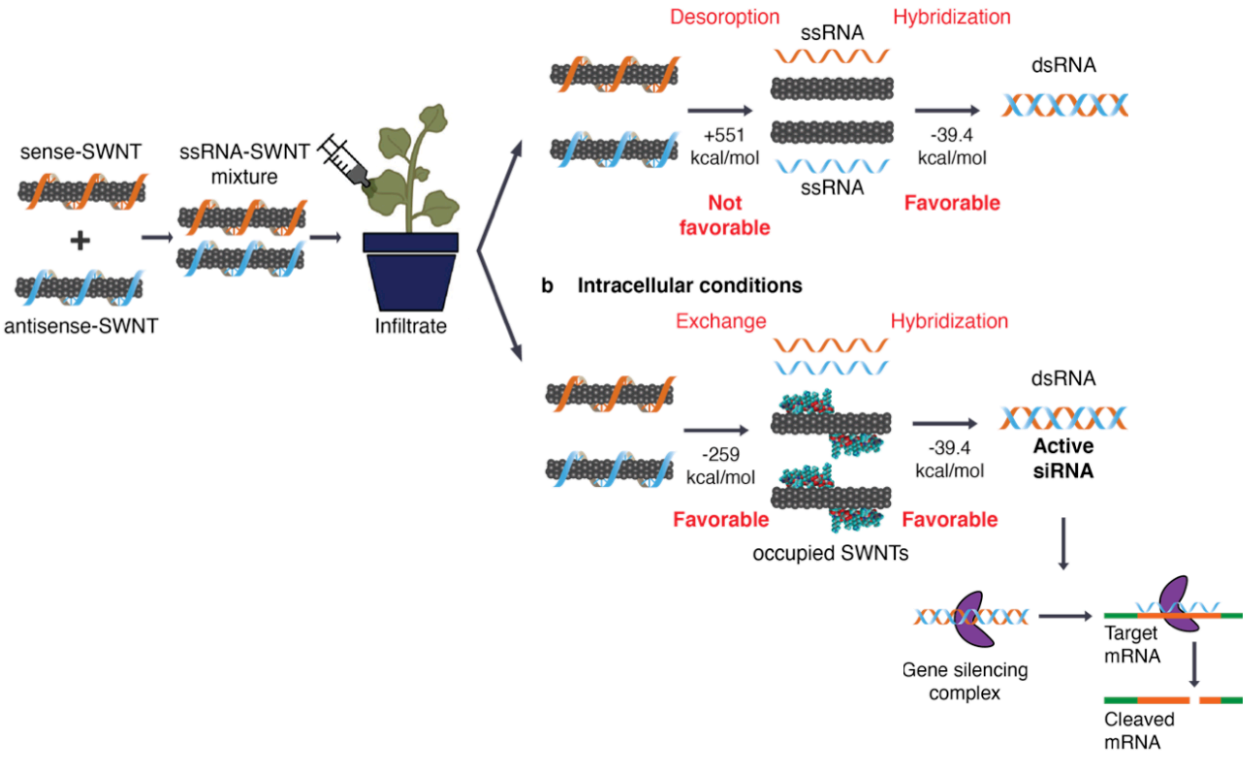

Figure 22. Thermodynamic analysis of RNA desorption from SWNTs: hybridization in extracellular and intracellular conditions and proposed gene silencing mechanism.

a, An equimolar mixture of sense-SWNT and antisense-SWNT suspensions are infiltrated into transgenic *Nb* leaves with a needleless syringe. In the extracellular area of leaf tissue, RNA desorption and hybridization is not thermodynamically favorable due to the high free energy cost of bare SWNTs. **b**, Inside cells, RNA desorption from SWNTs and hybridization is thermodynamically favorable because molecules can occupy the bare SWNT surface and lower the RNA desorption free energy cost. Upon desorption from SWNTs, double-stranded active siRNA assembles with the gene silencing complex and complexes with target mRNA for cleavage and gene silencing.

In this section, we perform a thermodynamic analysis to model whether siRNA sense and antisense complementary strands desorb from the SWNT surface and hybridize to each other in either the intracellular or extracellular environment. In both cases, it is assumed that the ssRNA desorption from the SWNT surface is the first step, followed by hybridization of free ssRNA to form double-stranded RNA (dsRNA): nucleic acid adsorption to SWNTs is through π-π interactions and H-bonding to neighboring strands, therefore, in order to hybridize and form Watson-Crick base-pairing H-bonds, the ssRNA strands first must desorb from the SWNT surface.

3.5.1. Extracellular thermodynamics analysis

Calculation for ssRNA desorption from SWNT:

In this analysis, we use energy values for adsorption of individual nucleobases to SWNTs from Johnson *et al.*[141] (Table 2) to calculate the total desorption energy of each ssRNA sequence used in this study (Table 3). Johnson *et al*. use solvent-explicit, all-atom molecular dynamics (MD) simulations for 21-nucleotide hetero- and homo-polymers adsorbing to SWNTs. Note that these energies are in close agreement with Das *et al.*[142], calculated from density functional theory (DFT) and experiment.

Table 2: Adsorption energy of each nucleotide to SWNTs[141]

Base	Energy [kcal/mol]
A	-13.84
G	-14.99
C	-11.07
T = U	-12.68

Using these adsorption energies, we calculate the average desorption energy of ssRNA from the SWNT surface to be +275.3 kcal/mol ± 11.25, which we then multiply by 2 ssRNA strands to have +550.6 kcal/mol for both siRNA sense and antisense desorption from SWNTs (Table 3).

Table 3: ssRNA-SWNT desorption energy and RNA hybridization energy for each ssRNA sequence

Sequence Name	Sequence	Desorption Energy[kcal/mol]	Hybridization Energy [kcal/mol]
a-antisense	UUC CGU AUG UUG CAU CAC CTT	267.1	-39.22
a-sense	GGU GAU GCA ACA UAC GGA ATT	283.4	-39.10
b-antisense	GGG UGA AGG UGA UGC AAC ATT	288.5	-39.67
b-sense	UGU UGC AUC ACC UUC ACC CTT	261.5	-39.80
NT-antisense	GUA UCU CUU CAU AGC CUU ATT	267.5	-33.76

NT-sense	UAA GGC UAU GAA GAG AUA CTT	283.9	-33.89
	Average	**275.3**	**-39.37**
	Standard deviation	11.25	0.3743

<u>Calculation for ssRNA to dsRNA hybridization:</u>

ssRNA hybridization next occurs in solution. We use the OligoAnalyzer tool through Integrated DNA Technologies, Inc., with the following assumed ion and ssRNA concentrations: $[Na^+] = 10$ mM, $[Mg^{2+}] = 0.1$ mM, and [ssRNA] = 0.25 μM. We calculate the hybridization energy for each ssRNA sequence used in this study, and the average hybridization energy is -39.37 kcal/mol ± 0.3743 (Table 3). Therefore, the overall free energy change under extracellular conditions is:

$$\Delta G_{extracell} = \Delta G_{ssRNA,des} + \Delta G_{hyb} = \left(+550.6\frac{kcal}{mol}\right) + \left(-39.37\frac{kcal}{mol}\right) = \mathbf{+511.2}\,\boldsymbol{\frac{kcal}{mol}}$$

Based on this positive (unfavorable) free energy change, our analysis demonstrates that it is unlikely for ssRNA desorption and hybridization to take place spontaneously in the extracellular environment when both complementary ssRNA strands are initially adsorbed on SWNTs.

3.5.2. Intracellular thermodynamics analysis

The intracellular environment is crowded with biomolecules, is highly dynamic, and intracellular components of the cell cytoplasm such as proteins and lipids are known to bind to SWNTs[143]. Accordingly, once inside the cell, cytoplasmic biomolecules will likely adsorb on SWNTs, as observed by SWNT solvatochromic shifts (Fig. 21b), and replace the nucleic acids originally on the SWNT surface[144]. Therefore, we hypothesize that inside the cell, ssRNA desorption and hybridization are likely to take place because the high free energy of "bare" SWNTs is avoided by direct biomolecule replacement, hence making this process thermodynamically favorable under cytoplasmic conditions as calculated below (Fig. 22b). We assume that the same ssRNA desorption energies apply, but now this unfavorable ssRNA desorption is countered by favorable protein adsorption to the SWNT surface.

<u>Calculation for protein adsorption energy to SWNTs:</u>

We assume that the ssRNA desorption and protein adsorption steps take place independently, as shown to be likely from experiment[144]. Shen *et al.*[145] use MD simulations to model the adsorption of human serum albumin (HSA) helices on different chirality SWNTs with water as the solvent and calculate an average protein adsorption energy of -14.51 kcal/mol ± 1.858 per amino acid. Similarly, DFT calculations have reported protein adsorption to carbon nanotubes with an average energy of ~ -10 kcal/mol per amino acid[146]. Hence, we assume -10 kcal/mol binding energy per amino acid.

To calculate how many amino acids replace each pre-adsorbed ssRNA strand on the SWNT surface, we make the following contact area estimations. First, nucleic acids have been shown to form helices wrapping around SWNTs above a length of ~12 nucleic acids[147]. Since these ssRNA strands are 21-mers, we assume helix morphology. RNA is known to adopt A-form helices, in which there are 25 Å per helical turn and ~11 nucleotides per helical turn, therefore 2.27 Å per nucleotide[148]. For the 21-mer ssRNA, this is 47.67 Å "helix length" L along the SWNT. Estimating that the nucleotides occupy the entire space between helically wrapped strands, this allows the surface area calculation: $SA_{\mathrm{cyl}} = 2\pi rL$, where r = 0.5 nm on average for these SWNTs, therefore SA_{cyl} = 14.98 nm^2 or 1,498 Å^2. This contact area calculation is within a reasonable order of magnitude, in comparison to an MD simulation of helix-forming $(GT)_{15}$ (30-mer) ssDNA on SWNTs occupying 2,400 Å^2, or 80 Å^2 per nucleotide (versus 71.31 Å^2 per ssRNA as calculated above).

Next, for protein contact area, we use beta sheet dimensions as a proxy of protein adsorption to SWNTs. In beta sheets, there are 3.25 Å per amino acid for X amino acids, or 3.25*X Å lengthwise on the SWNT. The width of the protein along the SWNT can be approximated as twice the R-group width for beta sheet geometry. Assuming aromatic R-group amino acids (Tyr, Phe, Trp) interact with SWNTs and calculating dimensions based on bond lengths, the average R-group dimension is 5.69 Å, or W = 2*5.69 = 11.38 Å. Then, contact area SA_{rect} = L*W = 36.99*X Å^2. Comparing the ssRNA to protein estimated surface areas, we see that 40.5 amino acids replace one 21-mer ssRNA on the SWNT surface.

Accordingly, for 40.5 amino acids and -10 kcal/mol per amino acid, we obtain -405 kcal/mol for an average protein adsorption energy to SWNTs. Note that this energy is within a reasonable order of magnitude, as HSA adsorption on carboxylated SWNTs is ~ -500 kcal/mol *via* MD simulation[149]. Moreover, the median number of amino acids per protein in *A. thaliana* is 356 amino acids[150], and assuming ~10% amino acids participate in protein adsorption gives -356 kcal/mol. Finally, multiplying by 2 SWNTs, we have -810 kcal/mol for protein adsorption to the SWNT surface. Therefore, the overall change in free energy in intracellular conditions is:

$$\Delta G_{intracell} = \Delta G_{ssRNA,des} + \Delta G_{prot,ads} + \Delta G_{hyb}$$

$$= \left(+550.6\frac{kcal}{mol}\right) + \left(-810\frac{kcal}{mol}\right) + \left(-39.37\frac{kcal}{mol}\right) = \boldsymbol{-298.8\frac{kcal}{mol}}$$

Our analysis shows that this overall free energy change is negative inside plant cells, which demonstrates that desorption from the SWNT surface and subsequent hybridization of complementary ssRNA sequences are favorable and spontaneous in intracellular conditions, recapitulating our experimental results.

3.6. Experimental Validation of RNA Desorption and Hybridization

Hybridization and desorption of sense and antisense RNA strands was verified with an *in vitro* experiment, where I mixed and incubated an equimolar mixture of a-sense-SWNT and a-antisense-SWNT suspensions for 3 h at room temperature; either in water or in plant cell lysate solution (Fig. 23b). I then eluted the desorbed siRNA and quantified it *via* absorbance at 260 nm. The results confirm that an insignificant amount of siRNA is desorbed when RNA-SWNTs incubated in water, whereas 66% of the siRNA is desorbed when incubated in plant cell lysate solution. I then ran the eluted RNA from the cell lysate sample on an agarose gel and showed that it is double-stranded, which verifies the formation of double-stranded siRNA in the cell cytosol (Fig. 23c). Additionally, zeta potential measurements of a-siRNA-SWNTs before and after hybridization in water and removal of desorbed RNA show unchanged nanoparticle zeta potential, suggesting there is not significant amount of RNA hybridization and desorption from SWNT surface in water (Fig. 23d).

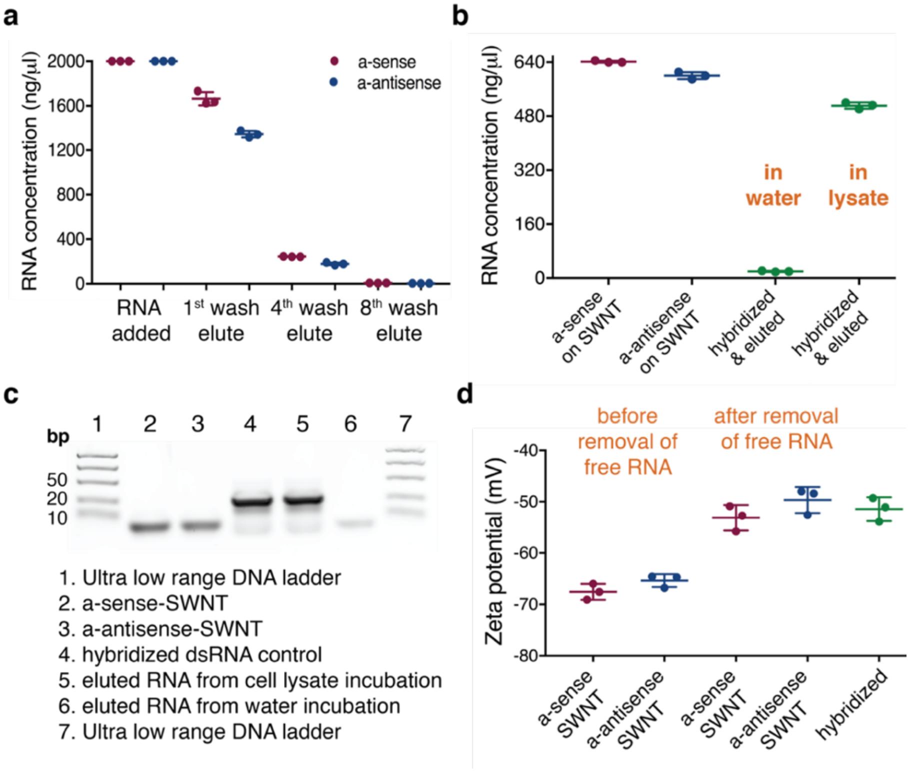

Figure 23. Characterization of dsRNA hybridization and desorption.

a, a-sense and a-antisense amount added to suspend SWNTs, RNA concentration in the 1st, 4th and 8th flow-through after centrifugation with 100K spin filters to remove free RNA. **b**, RNA amount on suspended SWNTs, dsRNA eluted after hybridization in water and in cell lysate conditions. **c**, 4% agarose gel showing eluted RNA in cell lysate and water, 97% dsRNA is eluted from the cell lysate incubation and 19% of ssRNA is eluted from the water sample. **d**, Zeta potential for a-sense-SWNT and a-antisense-SWNT suspensions before and after the removal of free RNA, and after mixing a-sense-SWNT and a-antisense-SWNT in water and eluting free RNA (hybridized).

Once hybridized, double-stranded active siRNA can merge with the gene silencing complex, whereby the antisense strand of siRNA directs the complex to the endogenous target mRNA. Upon hybridization of the antisense strand with the complementary target mRNA, a protein in the gene silencing complex (Argonaute), cleaves the target mRNA and prevents translation of GFP proteins (Fig. 22b).

3.7. siRNA-SWNT Mediated Gene Silencing in Intact Plants

Following verification of SWNT internalization and formation of active siRNA complexes in plant cells, I next infiltrated transgenic *mGFP5 Nb* leaves with siRNA-SWNTs and control solutions to determine the gene silencing efficiency. Silencing studies were conducted with the following samples at 100 nM final siRNA and 2 mg/L final SWNT concentration: non-treated leaves, s-RNA-SWNT (non-targeting), free siRNA, a-siRNA-SWNT, and b-siRNA-SWNT (Table 4 for sequences). I have shown that 100 nM siRNA on SWNTs is an optimal dose to be used in *mGFP5* silencing studies (Fig. 24).

Table 4: RNA sequences and primers used in the siRNA silencing study

RNA sequences:	(all sequences written as 5' to 3')
a-antisense	UUC CGU AUG UUG CAU CAC CTT
a-sense	GGU GAU GCA ACA UAC GGA ATT
b-antisense	GGG UGA AGG UGA UGC AAC ATT
b-sense	UGU UGC AUC ACC UUC ACC CTT
s-antisense	GUA UCU CUU CAU AGC CUU ATT
s-sense	UAA GGC UAU GAA GAG AUA CTT
Cy3 tagged a-antisense	Cy3/UUC CGU AUG UUG CAU CAC CTT
ROQ1-sense	GGU UUA AUU UGG UGU AUA A
ROQ1-antisense	UUA UAC ACC AAA UUA AAC C
Primers for qPCR:	
EF1 forward	TGG TGT CCT CAA GCC TGG TAT GGT TG
EF1 reverse	ACG CTT GAG ATC CTT AAC CGC AAC ATT CTT
mGFP5 forward	AGT GGA GAG GGT GAA GGT GAT G
mGFP5 reverse	GCA TTG AAC ACC ATA AGA GAA AGT AGT G
NbrbohB forward	TTT CTC TGA GGT TTG CCA GCC ACC ACC TAA
NbrbohB reverse	GCC TTC ATG TTG TTG ACA ATG TCT TTA ACA
ROQ1 forward	TCC CCG ACA TAA AGG AAT GC
ROQ1 reverse	GTC CCC TGG ACT CAA ACA GG

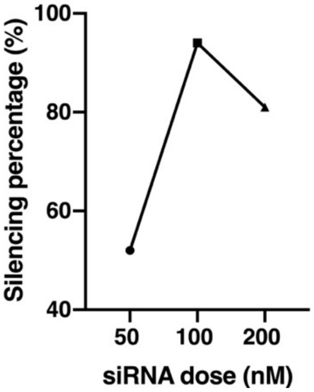

Figure 24. Optimization of siRNA dose on SWNTs for mGFP5 silencing.

Final siRNA concentration of 50, 100 and 200 nM on SWNTs, and corresponding gene silencing efficiencies at 1-day post-infiltration measured via qPCR assay.

Transgenic *Nb* leaves that constitutively express GFP were imaged *via* confocal microscopy to quantify GFP silencing at the protein level. Representative confocal images of the leaves 2-days post-infiltration reveals that both a-siRNA-SWNTs and b-siRNA-SWNTs lead to significant reduction of GFP in cells, whereas GFP expression in leaves infiltrated with s-RNA-SWNT and free siRNA appears similar to GFP expression in non-treated leaves (Fig. 25a). Quantification of GFP fluorescence intensity from the confocal images of s-RNA-SWNTs and a-siRNA-SWNTs reveals that a-siRNA-SWNT infiltrated leaves have 38% ± 3.2% (mean ± SD) less GFP protein 3-days post-infiltration compared to the s-RNA-SWNT infiltrated leaves. At 7-days post-infiltration, a-siRNA-SWNT shows roughly the same amount of GFP, 106.6 ± 4.1% (mean ± SD), as s-RNA-SWNT infiltrated leaves (Fig. 25b), as expected since gene silencing with siRNA is a transient process due to rapid RNA degradation in cells. GFP silencing with a-siRNA-SWNT was also verified with a Western blot analysis, where GFP extracted from the *Nb* leaves infiltrated with a-siRNA-SWNT is 42.6% ± 2.8% less than GFP extracted from s-RNA-SWNT infiltrated leaves both at 1 and 2-days post-infiltration (Fig. 25c).

I corroborated the GFP reduction results obtained with confocal imaging and Western blot analysis by performing quantitative PCR (qPCR) at the mRNA transcript level. One day after infiltration of leaves with s-RNA-SWNT, free siRNA, a-siRNA-SWNT, and b-siRNA-SWNT, I extracted total RNA from the leaves and quantified the GFP mRNA transcript levels in each sample at Day 1 and 7. qPCR demonstrates that s-RNA-SWNT and free siRNA infiltrated leaves have the same amount of GFP mRNA transcript as the non-treated leaf, whereby a-siRNA-SWNT and b-siRNA-SWNT infiltrated leaves show 95% ± 4.1% (mean ± SD) and 92% ± 6.2% (mean ± SD) reduction in the GFP mRNA transcript levels at Day 1, respectively (Fig. 25d). Similar to the confocal results, I found that mRNA transcript levels return back to the baseline levels as observed in non-treated leaves by Day 7 in all samples as a result of transient silencing (Fig. 25d). Additionally, I show that I can recover GFP silencing at Day 7 by up to 71% ± 2.9% (mean ± SD) by re-infiltrating the leaf with second 100 nM a-siRNA-SWNT dose at Day 5 (Fig. 25e).

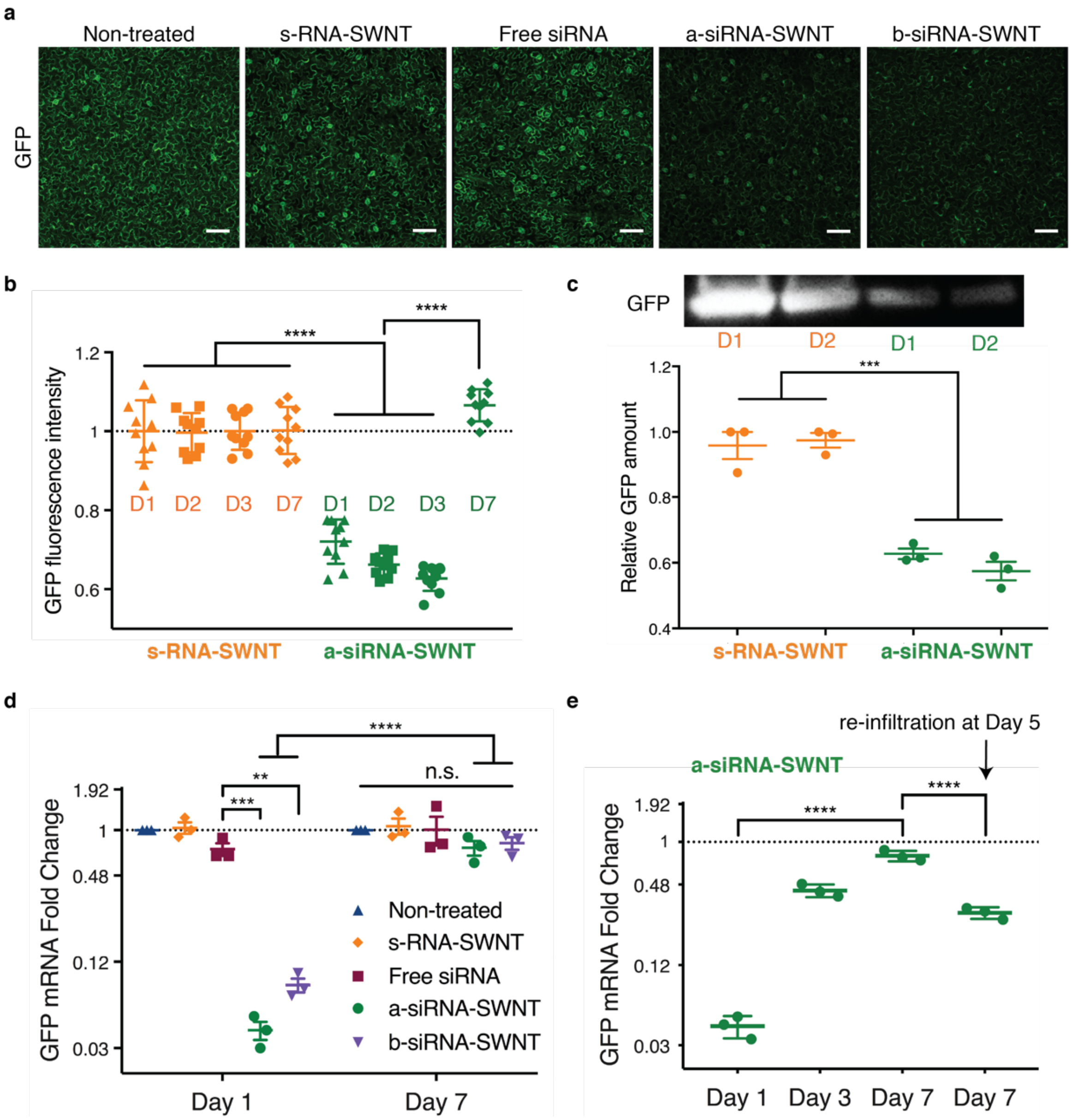

Figure 25. GFP gene silencing with RNA-SWNTs at the mRNA transcript and protein level.

a, Representative confocal microscopy images of non-treated, s-RNA-SWNT, free siRNA, a-siRNA-SWNT, and b-siRNA-SWNT infiltrated transgenic *Nb* leaves 2-days post-infiltration. Scale bars, 100 μm. **b,** Quantitative fluorescence intensity analysis of confocal images for s-RNA-SWNT and a-siRNA-SWNT at 1, 2, 3 and 7-days post-infiltration. ****$P < 0.0001$ in one-way ANOVA. Error bars indicate s.d. (n = 10). **c,** Representative Western blot for GFP extracted from s-RNA-SWNT and a-siRNA-SWNT infiltrated *Nb* leaves 1- and 2-days post-infiltration, and quantification of GFP protein. ***$P = 0.0001$ in one-way ANOVA and error bars indicate s.e.m. (n = 3). **d,** qPCR analysis for GFP mRNA fold change at Day 1 and 7 post-infiltration for all samples tested. **$P = 0.0016$, ***$P = 0.0008$ and ****$P < 0.0001$ in two-way ANOVA (n.s: non-significant) All error bars indicate s.e.m. (n = 3). **e,** qPCR analysis for GFP mRNA fold change at Day 1, 3, 7 and Day 7 with re-infiltration at Day 5 for a-siRNA-SWNT treated *Nb* leaf sample. ****$P < 0.0001$ in one-way ANOVA and all error bars indicate s.e.m. (n = 3). All qPCR data for GFP expression are normalized with respect to housekeeping gene Elongation Factor 1 (EF1), and a control sample of a non-treated leaf.

With the same technique described above, I also demonstrated the silencing of a functional endogenous *Nicotiana benthamiana* gene called ROQ1, which has implications in disease resistance against many plant pathogens[151] (Fig. 26). The results verify that SWNTs can also silence an endogenous plant gene, ROQ1, efficiently, and suggest that other endogenous genes may be targeted for downregulation with SWNT-based siRNA delivery.

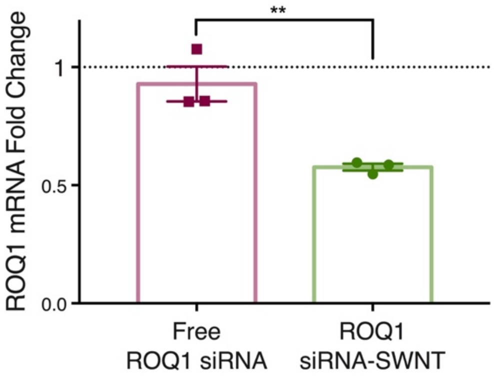

Figure 26. Silencing of endogenous functional *Nicotiana benthamiana* ROQ1 gene with siRNA-SWNTs.

Free ROQ1 siRNA without SWNTs do not show significant silencing of ROQ1 gene, whereas 100 nM ROQ1 siRNA on SWNTs yields nearly 50% mRNA reduction at Day 1 as assessed by qPCR of infiltrated *Nicotiana benthamiana* leaves compared to the non-treated control leaves. ** P = 0.0094 in two-tailed t-test. Error bars indicate s.e.m. (n = 3).

3.8. SWNT Scaffold Delays Intracellular RNA Degradation

It is likely that SWNT scaffolding improves internalization of siRNA and also protects siRNA from degradation once intracellular. To explore this hypothesis, we performed single molecule total internal reflection fluorescence (smTIRF) microscopy to probe single siRNA strand susceptibility to degradation by RNase A when adsorbed on SWNTs, compared to single free siRNA. To do so, we labeled the a-antisense strand of GFP siRNA with a 5′ terminal Cy3 fluorophore, and immobilized RNA-Cy3 and RNA-Cy3-SWNTs onto parallel channels of a microfluidic slide. We measured the Cy3 fluorescence in each channel before and after treatment with RNase A, whereby percent decrease in the number of Cy3 molecules was used as a proxy for the percent siRNA degraded (Fig. 27a). Our TIRF results show that 98% ± 0.3% (mean ± SD) of the initial Cy3-RNA immobilized on the channel surface is degraded after incubation with RNase A, whereas only 16% ± 4.9% (mean ± SD) of Cy3-RNA is degraded when it is bound to SWNTs, suggesting that SWNTs protect the siRNA cargo from enzymatic degradation inside cells (Fig. 27b). Negative controls in which only salt buffer is flown through, or empty BSA-passivated channels, do not show appreciable changes in fluorescence or fluorescence counts, respectively.

Intracellular stability of ssRNA suspended SWNTs and free ssRNA was also assessed by incubating ssRNA-SWNT conjugates with total proteins extracted from plant leaves (*i.e.* plant cell lysate). Agarose gel electrophoresis of free ssRNA *vs.* ssRNA-SWNTs incubated in plant cell lysate for 1, 3, 6, 12, and 24 hours demonstrate that free ssRNA is degraded significantly faster in cell lysate compared to ssRNA adsorbed on SWNTs (Fig. 27c). Band intensity quantification of this agarose gel reveals that both free ssRNA and ssRNA on SWNTs start degrading immediately in cell lysate solution. By 6 hours, 94% of free ssRNA and 70% of ssRNA on SWNTs is degraded (Fig. 27d and e). Results show that by 12 hours, all free ssRNA is completely degraded, whereas 14% of the ssRNA on SWNTs remains intact. By 24 hours, ssRNA on SWNTs is completely degraded (Fig. 27d and e), which corresponds to a 12 hour increase in the residence time of siRNA strands in cells when delivered with SWNTs. I hypothesize this increased residence time gives rise to prolonged and increased silencing efficiency, as siRNA strands in cells have a higher chance of hybridizing into the active siRNA duplex before getting degraded by plant nucleases if delivered with SWNTs.

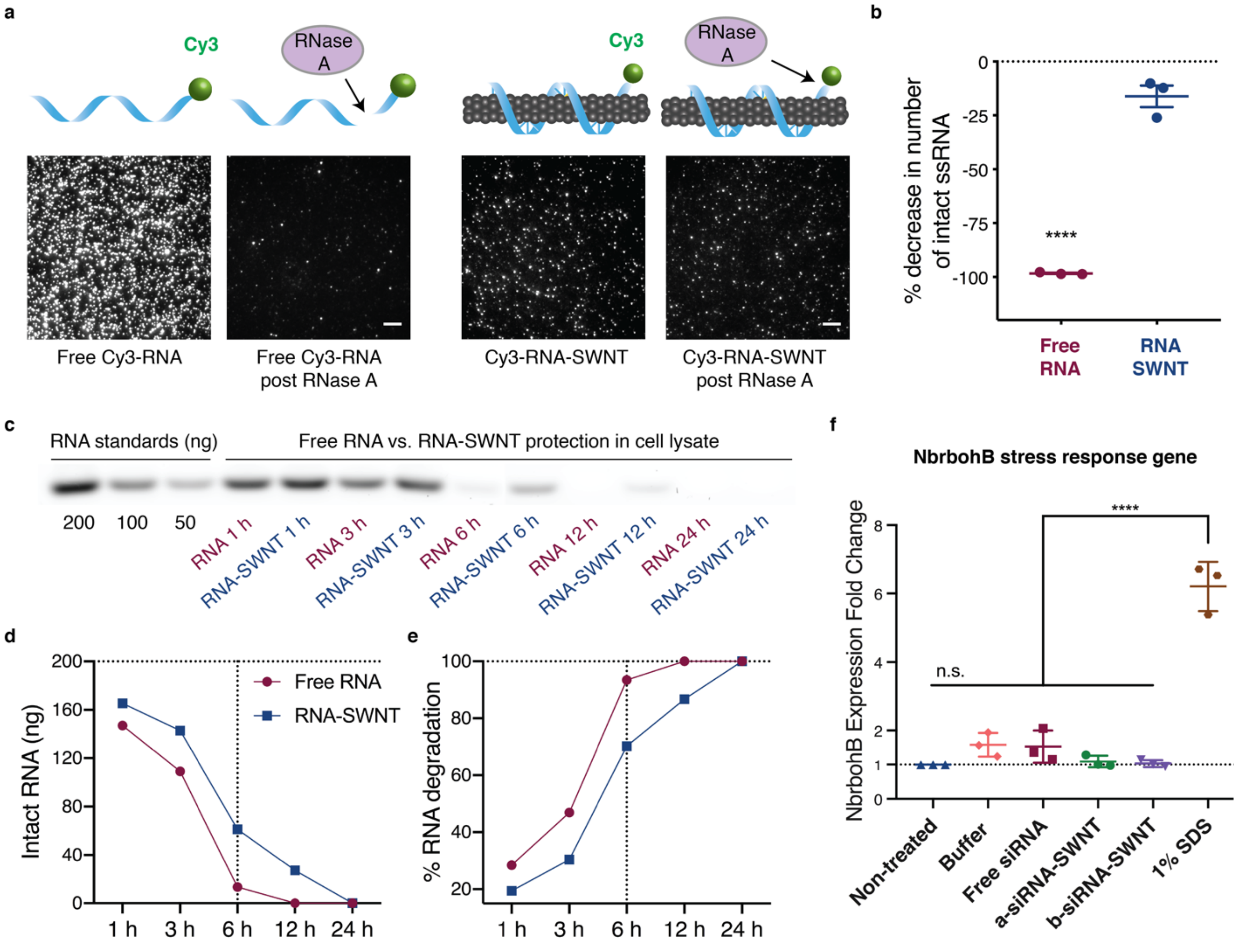

Figure 27. RNA protection from enzymatic degradation and SWNT toxicity analysis.
a, smTIRF microscopy of Cy3-labeled RNA and Cy3-labeled RNA-SWNTs before and after incubation with RNase A. Scale bars, 5 µm. **b,** Quantification of % decrease in number of intact RNA molecules upon RNase A treatment. Error bars indicate s.e.m. (n = 3). *****P* < 0.0001 in two-tailed unpaired t-test. **c,** Agarose gel electrophoresis of free RNA and RNA-SWNTs incubated in plant cell lysate for 1, 3, 6, 12, and 24 hours. **d,** Quantification of intact RNA from the agarose gel in part c. **e,** Quantification of % RNA degradation from the agarose gel in part c. **f,** qPCR analysis of *NbrbohB* following a 3-hour exposure to samples. *****P* < 0.0001 in one-way ANOVA and error bars indicate s.e.m. (n = 3).

With a similar *in vitro* cell lysate degradation experiment, I also show that after hybridization and desorption from SWNTs, about a quarter of the originally-delivered double-stranded siRNA persists in cells by 4-days. Results show that by 24 h, half of the double-stranded siRNA and by 96 h almost all of the double-stranded siRNA is degraded in cells (Fig. 28).

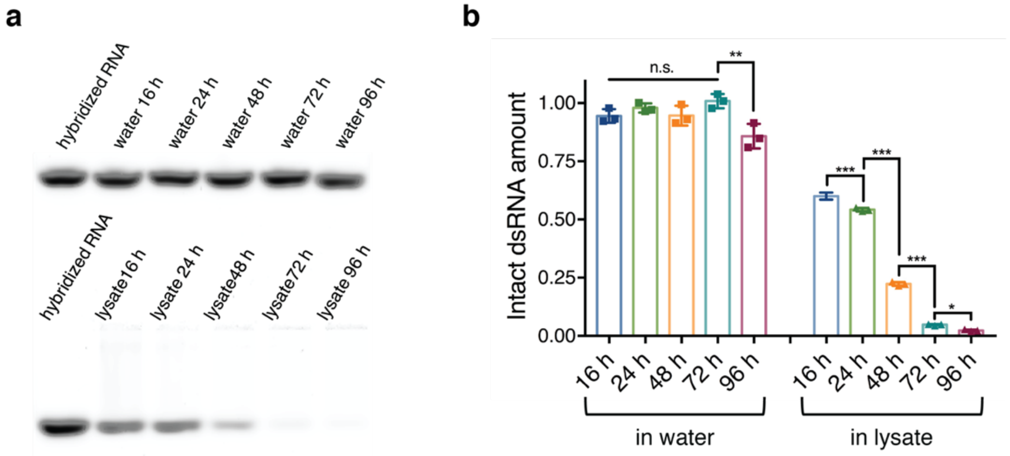

Figure 28. dsRNA stability in cell lysate.

a, Hybridized double stranded siRNA samples incubated in nuclease-free water and cell lysate solutions at room temperature for 16, 24, 48, 72 and 96 hours, and run on a 2% agarose gel. **b,** Quantification of RNA bands from the gel in part a and two other replicates, using the Image J gel analyzer tool. All band intensities are normalized with respect to the hybridized RNA band intensity at time zero without any treatment.

SWNT biocompatibility, at the concentrations used in this study, was tested by qPCR analysis of a commonly used stress gene, and by tissue damage analysis *via* confocal microscopy. For qPCR toxicity analysis, I checked the upregulation of the respiratory burst oxidase homolog B (*NbrbohB*) gene (Fig. 27f). *NbrbohB* upregulation in *Nicotiana benthamiana* leaves represents stress response to many factors such as mechanical, light or heat damage. qPCR results show that 2 mg/L RNA-SWNT treated areas in leaves do not upregulate *NbrbohB* gene compared to buffer treated adjacent areas within the same leaves. 1% SDS solution was used as a positive toxicity control, and upregulated *NbrbohB* gene by 6-fold 3 hours post-infiltration (Fig. 27f). Tissue damage in the RNA-SWNT and 1% SDS infiltrated leaves was also monitored *via* confocal microscopy, and no tissue or cell damage was detected in RNA-SWNT infiltrated leaves, whereas significant distortion of cell morphology and tissue integrity can be seen in the SDS treated areas (Fig. 29). Given the unchanged expression levels of stress gene *NbrbohB*, and healthy leaf tissue of RNA-SWNT infiltrated plants, I can conclude that 2 mg/L RNA-SWNTs are biocompatible for *in planta* RNAi applications.

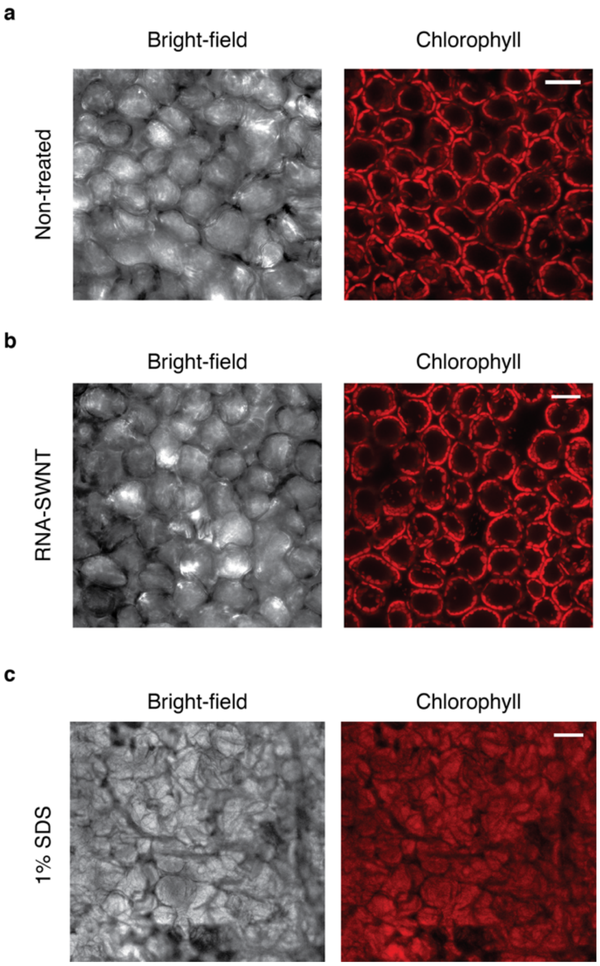

Figure 29. Confocal microscopy imaging of the *Nb* leaf tissue to assess cellular damage.
a, Representative bright-field and chlorophyll images of non-treated *Nb* leaf. **b,** RNA-SWNT treated *Nb* leaf and **c** 1% SDS treated *Nb* leaf as a positive control of leaf tissue damage. All scale bars, 20 μm.

3.9. Discussion

Nanomaterials have shown much promise for plasmid[42] and protein[47] delivery to plants, motivating their use for plant delivery of RNAi, as has proven quite fruitful for human therapeutics. I demonstrate here that high-aspect-ratio one dimensional SWNTs can successfully deliver siRNA molecules to efficiently silence a GFP gene in transgenic *Nicotiana benthamiana* mature plant leaves, through a combination of i) effective intracellular delivery and ii) protection of the siRNA cargo from nuclease degradation. I found that RNA adsorbed SWNTs rapidly and efficiently internalize into the full leaf thickness of mature walled plant cells within 6 hours, in contrast to free RNA internalization which is minimal. I further found that π-π adsorption of siRNA on the SWNT surface delays intracellular siRNA degradation and thus prolongs silencing.

Here, I developed a platform for siRNA delivery using nanoparticles, well suited for cellular delivery in plant tissues with intact cell walls. This platform utilizes SWNTs, to which single-stranded sense and antisense siRNA are adsorbed separately, enabling thermodynamically-favorable siRNA hybridization once intracellular for subsequent gene silencing mechanisms. I show that ssRNA is protected from degradation for up to 24 hours when adsorbed to SWNTs, whereas free ssRNA is almost completely degraded by 6 hours. I show a similar siRNA protection phenomenon with single-molecule TIRF microscopy of individual siRNA molecules either free or adsorbed to SWNTs. With this rapid and facile SWNT delivery platform, I achieve transient and DNA-free silencing of genes in mature plant leaves with a low siRNA-SWNT dose, showing mRNA knockdown efficiencies of up to 95% within 1-day post-infiltration, returning to native transcript levels by day 7. I further show that it is possible to retain gene silencing for longer periods of time with a re-infiltration of another siRNA-SWNT dose at day 5, for applications in which sustained silencing is desired. Applications that require the introduction of repeated doses of siRNA-SWNTs may cause some long-term toxicity due to the nanoparticle accumulation in cells[152]. However, studies should be undertaken to investigate the long-term effects of SWNT accumulation in plant cells.

The commonly used cationic nanoparticles for the delivery of negatively charged siRNA through electrostatic interactions have shown appreciable cellular toxicity to cells for certain effective concentrations and/or charge densities[153]. The pristine non-charged SWNT surface eliminates this problem and makes it possible to scale-up the delivery of siRNA for higher doses or systemic administration. Additionally, the platform could be adapted to loading multiple siRNA sequences to multiplex gene silencing targets by delivering a mixture of SWNTs suspended with multiple siRNA sequences or loading a single SWNT sample with multiple siRNA sequences. Furthermore, SWNT internalization and polynucleotide delivery into plants is hypothesized to be species-independent, can be used with monocots, non-model species, hard-to-transform species, and cargo-carrying SWNTs are expected to diffuse into the full thickness of leaves providing a uniform transformation profile[42].

Given aforementioned advantages, I believe that there is a broad range of applications of the siRNA delivery platform. The process of RNA adsorption to SWNTs is based on π-π adsorption and thus agnostic to the function of the RNA cargo. Additional to the more traditional applications of RNAi in plants, such as disease/virus resistance, discovery of biosynthetic pathways, increasing the yield of small-molecule production, and understanding protein functions, SWNT-mediated gene silencing could also potentially be used for efficient and DNA-free delivery of other synthetic ribonucleic acids. For instance, SWNTs could aid nuclease-based genome editing in plants by delivery of single guide RNAs (sgRNAs) and/or messenger RNAs (mRNAs) for controlled and transient nuclease expression and subsequent genome editing. Another potential application of SWNT-based RNA delivery is for increasing homology-directed repair (HDR) rates in plants for gene knock-in applications, which could possibly be achieved by suppressing the expression of the genes required for competitive non-homologous end joining (NHEJ) repair pathways[154]. As the efficient suppression of these genes is only desirable for the few-day time window in which genome editing takes place, the SWNT-mediated gene silencing platform could enable such control over transient siRNA delivery. As such, SWNT-based delivery of polynucleic acids is a useful resource to expand the plant biotechnology toolkit.

3.10. Materials and Methods

Preparation of chemicals. Super purified HiPCO SWNTs (Lot # HS28-037) were purchased from NanoIntegris, and SWNTs samples were extensively purified before use. Single-stranded RNA strands, Cy3-tagged single-stranded RNA strands and all primer sequences were purchased from IDT and dissolved in 0.1M NaCl before use. 100K MWCO Amicon spin filters were purchased from Fisher Scientific. The following chemicals were purchased from Sigma-Aldrich: sodium dodecyl sulfate (molecular biology grade), sodium chloride, Tris/HCl, EDTA, NP-40, glycerol, BSA-Biotin and NeutrAvidin. RNAse A was purchased from Takara Bio. All PCR reagents and materials, and molecular biology grade agarose were purchased from Bio-Rad. UltraPure DNase/RNase-free distilled water from Invitrogen was used for qPCR, and EMD Millipore Milli-Q water was used for all other experiments.

Plant growth. Transgenic mGFP5 *Nicotiana benthamiana* seeds were kindly provided by the Staskawicz Lab, UC Berkeley. The seeds were germinated and grown in SunGro Sunshine LC1 Grower soil mix for four to six weeks before experiments in a growth chamber, 12-hour light at 24°C and 12-hour dark at 18°C cycle. All experiments were done with intact leaves attached to plants, where plants were incubated in the growth chamber until the time of data collection.

RNA-SWNT and Cy3-RNA-SWNT preparation. SWNTs were suspended with single-stranded RNA polymers or Cy3-tagged single-stranded RNA sequences through probe-tip sonication as previously described. Briefly, RNA was dissolved in 0.1 M NaCl at a concentration of 100 mg/mL. 1 mg dry HiPCO SWNTs was added to 20 µL of dissolved RNA, and the solution volume was completed to 1 mL with 0.1 M NaCl. The mixture of SWNTs and RNA was bath sonicated for 10 min at room temperature. Then it was probe-tip sonicated with a 3-mm tip at 50% amplitude (~7 W) for 30 min in an ice bath. The sonicated solution incubated at room temperature for 30 minutes and centrifuged at 16,100g for 1 h to remove bundled SWNT and any leftover metal catalyst precursor from SWNT synthesis. Any RNA that was not bound to SWNTs was removed *via* spin-filtering 8 times with 100K Amicon filters, and the SWNT concentration of RNA-SWNTs was determined by measuring the carbon nanotube absorbance at 632 nm. Absorbance spectra of RNA-SWNTs were collected with Shimadzu UV-3600 Plus, and fluorescence spectra of RNA-SWNTs were collected with a near-infrared spectrometer (Princeton Instruments IsoPlane 320 coupled to a liquid nitrogen-cooled Princeton Instruments PyLoN-IR 1D array of InGaAs pixels). RNA concentration on suspended SWNTs was determined by measuring the amount of RNA in flow-through solutions after each spin-filter step *via* absorbance at 260 nm and subtracting the total amount of free RNA washed from the total amount of RNA added.

In more detail, for each suspension, I start with 1 mg of SWNTs and 2 mg of RNA in 1 mL 0.1 M NaCl solution. After the probe-tip sonication and centrifugation, I end up with approximately 40 μg/mL SWNTs, meaning that our SWNT yield is 40 μg/1000 μg = 4%. In terms of siRNA yield, after the probe-tip sonication, centrifugation and removal of free RNA, I end up with 640 μg/mL RNA on SWNTs, meaning that our RNA yield is 640 μg/2000 μg = 32%. These values can slightly change from experiment to experiment, therefore, I made sure to use the same final diluted concentration of siRNA-SWNTs for every experiment at 100 nM siRNA and 2 mg/L SWNT.

AFM characterization. AFM characterization of RNA-SWNTs was performed as described in Demirer *et al.*[42] and in Chapter 2.8.

Infiltration of leaves with RNA-SWNTs and control solutions. Healthy and fully-developed leaves from mGFP5 *Nicotiana benthamiana* (4-6 weeks old) plants were selected for experiments. A small puncture on the abaxial (bottom) surface of the leaf was introduced with a pipette tip, and ~100 μL of the RNA-SWNT solution was infiltrated from the hole with a 1 mL needleless syringe with caution not to damage the leaf.

Internalization imaging with confocal and nIR fluorescence microscopy. The a-antisense siRNA strand was utilized in the internalization study. After infiltration of 100 nM RNA carrying 2 mg/L RNA-SWNTs, plants with attached infiltrated leaves were left in the plant growth chamber to allow for internalization for 6 h and imaged with confocal microscopy to track Cy3-tagged RNA-SWNTs in leaves. A Zeiss LSM 710 confocal microscope was used to image the plant tissue with 488 nm laser excitation with an eGFP filter cube to detect intracellular GFP, and 543 nm laser excitation with an appropriate filter cube to detect Cy3 fluorescence. The emission window of Cy3 was adjusted to 550-600 nm to avoid crosstalk between Cy3 and leaf chlorophyll autofluorescence. For nIR imaging, 40 mg/L RNA-SWNTs were infiltrated into leaves and plants with attached infiltrated leaves were left in the plant growth chamber to allow for internalization for 6 h and imaged with nIR microscopy to track intrinsic SWNT nIR fluorescence in leaves. RNA-SWNT leaf internalization images were captured using a custom-built microscope equipped with a Raptor Ninox VIS-SWIR 640 camera. A 1050-nm long pass filter was used to avoid chlorophyll autofluorescence, and a white lamp with an appropriate filter cube was used to image GFP. GFP and Cy3 (or nIR) images were analyzed with the ImageJ co-localization program to demonstrate internalization of RNA-SWNTs into cells.

In vitro RNA hybridization and desorption assay. a-sense-SWNT and a-antisense-SWNT solutions were prepared according to "RNA-SWNT and Cy3-RNA-SWNT preparation" section. Equimolar mixtures of these suspensions each containing 600 ng/µL RNA on SWNTs were either incubated in water or in plant cell lysate for 3 h at room temperature to allow for hybridization and desorption. Next, hybridized double-stranded RNA in solution was eluted with 100K spin filters and the concentration of RNA in the elute was measured *via* absorbance at 260 nm with Nanodrop. For zeta potential measurements, an equimolar mixture of a-sense-SWNT and a-antisense-SWNT suspensions were incubated in water for 3 h at room temperature to allow for hybridization and desorption. Next, hybridized double-stranded RNA in solution (if any) was eluted with 100K spin filters and the zeta potential of the remaining RNA-SWNT mixture was measured with Malvern Zetasizer.

Confocal imaging for silencing and quantitative fluorescence intensity analysis of GFP expression. mGFP5 *Nb* leaves were infiltrated with s-RNA-SWNT, free siRNA, a-siRNA-SWNT, and b-siRNA-SWNT at the same RNA concentration of 100 nM and SWNT concentration of 2 mg/L. Infiltrated plant leaves were prepared for confocal imaging 1, 2, 3, and 7-days post-infiltration as described in[42]. For each sample, mean fluorescence intensity value was normalized with respect to the mean GFP fluorescence intensity of a non-treated leaf. The same imaging parameters and quantification analyses were applied to samples imaged on different days.

Quantitative Western blot experiments and data analysis. Whole leaves fully infiltrated with samples were harvested 24 and 48 h post-infiltration, and total proteins were extracted as described in[42]. After quantification of the total extracted proteins by a Pierce 660 nm Protein Assay, 0.5 µg of normalized total proteins from each sample were analyzed by 12% SDS–PAGE and blotted to a PVDF membrane. The membrane was blocked for 1 hour using 7.5% BSA in PBST (PBS containing 0.1% Tween20) buffer and incubated overnight at 4°C with the primary GFP antibody as required (1:2000 dilution, Abcam, ab290). After extensive washing, the corresponding protein bands were probed with a goat anti-rabbit horseradish peroxidase-conjugated antibody (1:5000 dilution, Abcam, ab205718) for 30 min. The membrane was then developed by incubation with chemiluminescence (Amersham ECL prime kit) plus and imaged by ChemiDoc™ XRS+ System. The intensity of GFP bands were quantified with ImageJ software.

Quantitative PCR (qPCR) experiments for gene silencing. Two-step qPCR was performed to quantify GFP gene silencing in transgenic *Nb* plants as described in[42]. The target gene in our qPCR was *mGFP5* (GFP transgene inserted into *Nb*), and *EF1* (elongation factor 1) as our housekeeping (reference) gene. An annealing temperature of 60˚C and 40 cycles were used for qPCR. qPCR data was analyzed by the ddCt method[132] as described in[42]. For each sample, qPCR was performed as 3 reactions from the same isolated RNA batch, and the entire experiment consisting of independent infiltrations and RNA extractions from different plants was repeated 3 times (3 biological replicates).

Single molecule TIRF to image RNA protection by SWNTs. The a-antisense siRNA strand was utilized in this assay. 10 μM 5' labelled Cy3-RNA was added to an equal mass of SWNTs. The RNA-SWNT suspension and removal of unbound RNA followed the same protocol as described in 'Quantitative PCR (qPCR) experiments for gene silencing'. The positive control comprised of the same sequence that was 5' Cy3 labeled, and 3' biotin labeled. 6-channel μ-slides (ibidi, μ-Slide VI 0.5 Glass Bottom) were initially washed by pipetting 100 μL of 100 mM sterile NaCl solutions into one reservoir and removing 60 μL the other end, leaving just enough solution to fully wet the channel. Each subsequent step involved depositing the desired solution volume into the reservoir and removing the equivalent volume from the other end of the channel. Slide preparation was done as described by Kruss and Landry *et al.*[155] with some modifications. Briefly, 50 μL of 0.25 mg/mL BSA-Biotin was added to coat the surface of the glass slide for 5 minutes. Next, 50 μL of 0.05 mg/mL NeutrAvidin was added, followed by 50 μL of 1.0 mg/L RNA-SWNT, which non-specifically adsorbs to NeutrAvidin. For the positive control, 50 μL of 200 pM biotinylated Cy3-RNA was added in place of RNA-SWNT. The addition of each component comprised of a 5-minute incubation period, followed by flushing the channel with 50 μL of NaCl solution to remove specimens that were not surface-immobilized. Each channel was exposed to 50 μL of 10 μg/mL RNase A for 15 minutes at room temperature. The reaction was stopped by rinsing the channel with 50 μL NaCl solution. Slides were imaged with a Zeiss ELYRA PS.1 microscope immediately following incubation with RNase A.

RNA protection gel assay. To determine if SWNT adsorbed RNA is protected from nuclease degradation, I performed an agarose gel electrophoresis based RNA protection assay as described in[42]. 200 ng free RNA and RNA-SWNTs (carrying 200 ng RNA) were each incubated with cell lysate proteins obtained from one *Nb* leaf to mimic the intracellular degradation conditions for 1, 3, 6, 12, and 24 hours.

After incubation in cell lysate, all RNA (intact or not) was desorbed from the SWNT surface by heating at 95˚C for 1 hour in 2% SDS and 1.5 M NaCl solution. Desorbed RNA and cell lysate treated free RNA were run on a 1% agarose gel with RNA standards (200, 100, and 50 ng) to measure the intact *versus* degraded RNA in each sample lane. RNA amounts on the agarose gel were quantified by using band intensity as a proxy (ImageJ Gel Analyzer) and normalized with the lanes containing known RNA quantities.

dsRNA degradation gel assay. a-sense and a-antisense siRNA strands were hybridized by heating at 95˚C for 5 min and 37˚C for 1 hour. Hybridized double stranded siRNA samples were incubated in nuclease-free water and cell lysate solutions at room temperature for 16, 24, 48, 72 and 96 hours, and solutions were run on 2% agarose gel. Quantification of the RNA bands from the gel was done using Image J gel analyzer tool. All band intensities were normalized with respect to the hybridized RNA band intensity at time zero without any treatment.

Plant toxicity analysis. qPCR was used to determine the expression levels of an oxidative stress gene (*NbRbohB*)[117] in *Nicotiana benthamiana* plants treated with RNA-SWNTs and control solutions. The samples tested for toxicity were: buffer (0.1 M NaCl), 100 nM free siRNA, a-siRNA-SWNT, b-siRNA-SWNT (each containing 100 nM siRNA and 2 mg/L SWNT) and 1% SDS (as a positive toxicity control), and the qPCR was performed 3-hours after the infiltration of these samples. *EF1* gene was used as a housekeeping gene with an annealing temperature of 60˚C for 40 cycles. Same ddCt method was used to analyze the qPCR data.

CHAPTER 4. DNA NANOSTRUCTURES TO STUDY NANOPARTICLE UPTAKE AND TRANSPORT IN PLANTS

4.1. Summary

Delivery of biomolecules to plants relies on *Agrobacterium* infection or biolistic particle delivery, the former of which is only amenable to DNA delivery. The difficulty in delivering functional biomolecules such as RNA to plant cells is due to the plant cell wall which is absent in mammalian cells and poses the dominant physical barrier to biomolecule delivery in plants. DNA nanostructure-mediated biomolecule delivery is an effective strategy to deliver cargoes across the lipid bilayer of mammalian cells, however, nanoparticle-mediated delivery without external mechanical aid remains unexplored for biomolecule delivery across the cell wall in plants. In this chapter, I report a systematic assessment of different DNA nanostructures for their ability to internalize into cells of mature plants, deliver small interfering RNAs (siRNAs), and effectively silence a constitutively-expressed gene in *Nicotiana benthamiana* leaves. We show that nanostructure internalization into plant cells and the corresponding gene silencing efficiency depends on the DNA nanostructure size, shape, compactness, stiffness, and location of the siRNA attachment locus on the nanostructure. We further confirm that the internalization efficiency of DNA nanostructures correlates with their respective gene silencing efficiencies, but that the endogenous gene silencing pathway depends on the siRNA attachment locus. This work establishes the feasibility of biomolecule delivery to plants with DNA nanostructures, and details both the design parameters of importance for plant cell internalization, and also assesses the impact of DNA nanostructure geometry for gene silencing mechanisms.

4.2. Introduction

Plant bioengineering may generate high yielding and stress-resistant crops amidst a changing climate and a growing population. However, unlike mammalian cells, plant cells have a cell wall which poses the dominant barrier to exogenous biomolecule delivery. Currently, biological delivery (using bacteria or viruses) and particle bombardment are the two preferred methods of biomolecule delivery to plant cells. However, biological delivery methods are highly cargo and host-specific[156] whereas particle bombardment can result in tissue damage[157]. Nanomaterial-mediated biomolecule delivery has facilitated genetic engineering and biosynthetic pathway mapping in animal systems but has only recently been explored for plants. Specifically, two recent studies have shown that carbon nanotubes[158] and clay nanosheets[106] enable intracellular delivery of DNA and RNA through surface-grafting or encapsulation strategies, circumventing the use of biolistics (external force). Biological cargo delivery to plants without external aid is an exciting development that warrants an understanding of how nanomaterials can internalize into plant cells, so that nanotechnology can be logically designed for future applications in plant biotechnology.

DNA nanotechnology leverages the programmability of DNA Watson-Crick base pairing to assemble DNA nanostructures into custom predesigned shapes *via* sequence-specific hybridization of template and staple DNA strands[159]. To date, a plethora of different DNA nanostructures of variable sizes and shapes have been synthesized, and have shown functionality in biotechnology for drug, DNA, RNA, and protein delivery applications in animal systems. However, to-date, DNA nanostructures have not been explored for use in plant systems, despite their utility shown in other sectors of biotechnology.

In this chapter, we explore DNA nanotechnology as a biomolecule delivery platform in plants. We synthesized a series of DNA nanostructures of controllable size, shape, stiffness, and compactness, and designed attachment loci onto which DNA, RNA, or protein cargoes may be conjugated. By hybridizing fluorophore-conjugated DNA strands onto the loci of DNA nanostructures, we tracked nanostructure internalization into the plant cell cytoplasm of several plant species (*Nicotiana benthamiana*, *Nicotiana tabacum*, *Eruca sativa*, and *Nasturtium officinale*) and found that stiffness and size are important design elements for nanostructure internalization into plant cells. DNA nanostructures with sizes below ~10 nm, and higher stiffness or compactness, showed higher cellular internalization – although size or stiffness alone are not mutually-exclusive contributors to nanostructure internalization. DNA nanostructures were next loaded with siRNA targeting a GFP gene and infiltrated into plant leaves. This study revealed that DNA nanostructures enable gene silencing in plant leaves with efficiencies that match nanostructure internalization trends. Interestingly, the plant endogenous gene silencing mechanism can be affected by the DNA nanostructure shape and the siRNA attachment locus, affecting whether silencing occurs dominantly through transcriptional or post-transcriptional gene silencing. This study confirms that DNA nanostructures can be designed to internalize into plant cells, and that DNA nanostructures may be a promising toolset for the delivery of exogenous biomolecules to plants, as has proven valuable in animal systems.

4.3. Design, Construction and Characterization of DNA Nanostructures

We report the synthesis and systematic assessment of different DNA nanostructures for their ability to internalize into plant cells, and their subsequent utility for the delivery of siRNAs to mature plants. Three DNA nanostructures with programmed sizes and shapes were synthesized: a three-dimensional (3D) tetrahedron, a one-dimensional (1D) hairpin-tile (HT) monomer, and a high-aspect-ratio 1D nanostring as illustrated in Figure 30 (Table 5 for DNA/RNA sequences). Both the HT monomer and tetrahedron were assembled through four single stranded DNA oligonucleotides. Briefly, the HT monomer structure was designed to contain a sticky end and a stem-loop hairpin structure, enabling co-polymerization with another monomer to assemble into the length-controlled 1D nanostring by introduction of an initiator. The tetrahedron was also assembled through annealing of four pre-designed single stranded DNA oligonucleotides. Based on B-form double helix DNA dimensions, the sizes of the nanostructures are 2 × 5 × 16 nm for the HT monomer; 2 × 5 × 320 nm for the 10-unit nanostring; and 2.4 nm for all edges of the tetrahedron.

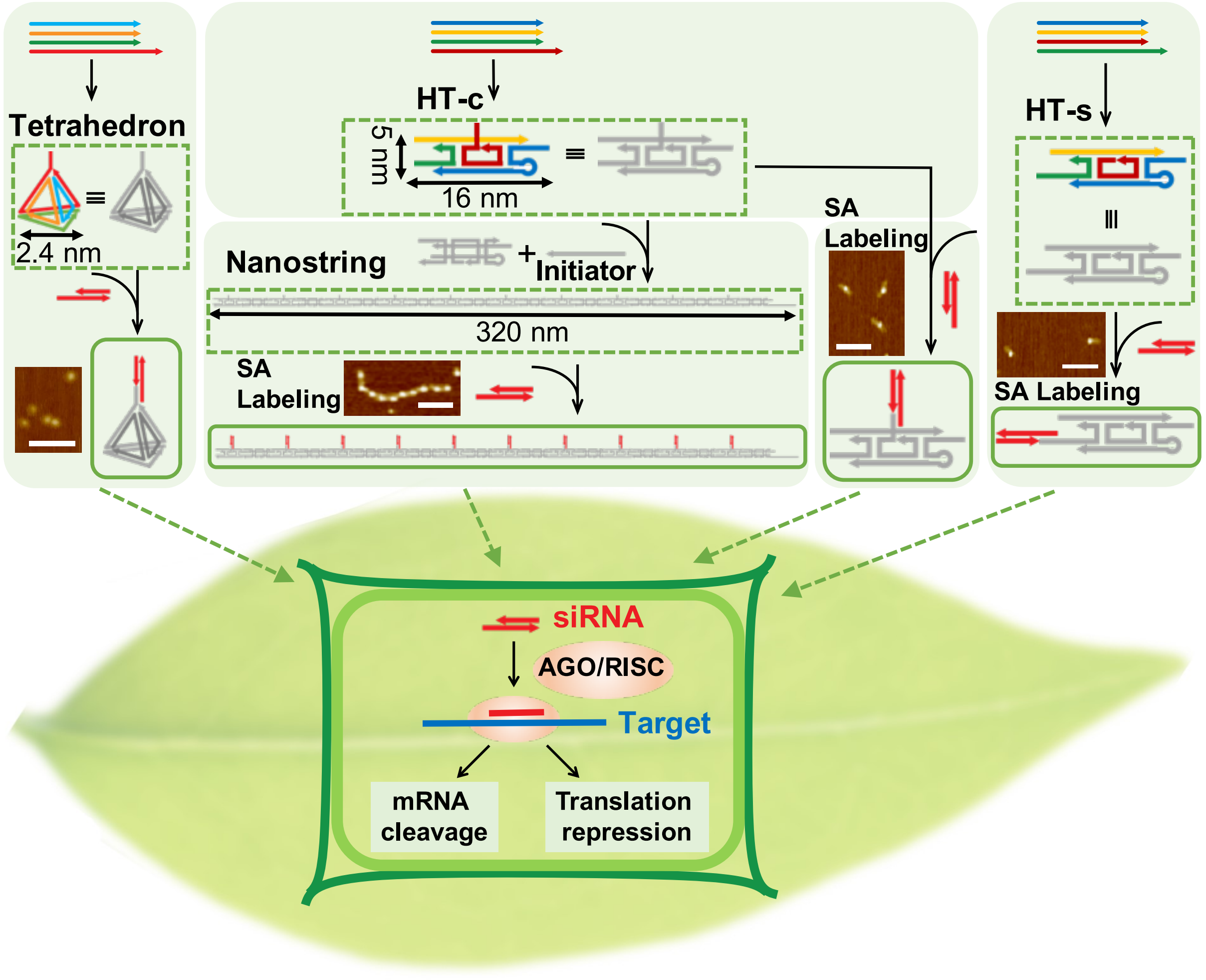

Figure 30. DNA nanostructure synthesis and plant infiltration workflow.

Tetrahedron and HT nanostructures were synthesized from four single stranded DNA sequences, and the 1D nanostring structure was synthesized by polymerization of HT monomers with the introduction of an initiator strand. The cargo attachment locus was designed to be at the apex of the tetrahedron, along the length of the nanostring, and to the side (HT-s) or center (HT-c) of each HT nanostructure. Inset AFM images of streptavidin bound biotinylated HT monomers (HT-c and HT-s) and nanostring show the attachment loci of the siRNA cargo. DNA nanostructures loaded with siRNA at each locus are infiltrated into the transgenic mGFP5 *Nicotiana benthamiana* plant leaves for downstream study of nanostructure internalization and gene silencing. Scale bars = 100 nm.

Table 5: Sequences of oligonucleotides used in the DNA nanostructure study

Name	Sequence (5'-3')
H1	GGACTTGTAGCGATACGACTCCGACGAGACTAGTAACTCTTG
H2	GGATGCGGAATGACAGCTACAAGTCCCAAGAGTTACGCTCTCCATTC
H3	TGTCACAGTAAGTCTTGTCATTCC
H4	GGGCTTGAATGGAGAGCCATCACTCATGTGAACCCATGAGTGATGTAGTCTCGTCGGAGTCGTATCAGACTTACT
H5	ACGAGACTACATGGTCAGATTCGTAGGTCCGATACGACTCCG
H6	GCATCCGATCCGTCCTGTCGGACCTACGAATCTGACCACCGAGAATC
H7	AAGCCCGATTCTCGGTCACTCATGGGTTCA
H8	CATGAGTGATGTAGTCTCGTCGGAGTCGTATCAGACTTACTGTGACAAGTAAGTCTGACAGGACGGATC
I	CATGAGTGATGTAGTCTCGTCGGAGTCGTATCAGACTTACTGTGACA
Bio-H1	Biotin-GGACTTGTAGCGATACGACTCCGACGAGACTAGTAACTCTTG
Cy3-H1	Cy3-GGACTTGTAGCGATACGACTCCGACGAGACTAGTAACTCTTG
H1-15-RNA	TACACGCATCCTTAGGGACTTGTAGCGATACGACTCCGACGAGACTAGTAACTCTTG
H2-15-RNA	TAC ACG CAT CCT GGA TGC GGA ATG ACA TGC TAC AAG TCC CAA GAG TTA CGC TCT CCA TTC
H5-15-CNT	ACGAGACTACATGGTCAGATTCGTAGGTCCGATACGACTCCG TAC ACG CAT CCT TAG
A-7	GAGCGTT A GCCACAC A CACAGTC
B-7	TTAGGCG A GTGTGGC A GAGGTGT
C-7	CGCCTAA A CAAGTGG A GACTGTG
D-7	AACGCTC A CCACTTG A ACACCTC
A-7-Cy3	GAGCGTT A GCCACAC A CACAGTC-Cy3
A-15-RNA	G CAT CCT TAG AAA AAA GAGCGTT A GCCACAC A CACAGTC
sense-15	CTA AGG ATG CGT GTA GGU GAU GCA ACA UAC GGAA TT
antisense	UUC CGU AUG UUG CAU CACC
$(GT)_{15}$-15	GTGTGTGTGTGTGTGTGTGTGTGTGTGTGT CTA AGG ATG CGT GTA
$(GT)_{15}$-15-Cy3	GTGTGTGTGTGTGTGTGTGTGTGTGTGTGT CTA AGG ATG CGT GTA-Cy3
fGFP	AGTGGAGAGGGTGAAGGTGATG
rGFP	GCATTGAACACCATAAGAGAAAGTAGTG
fEF1	GCATTGAACACCATAAGAGAAAGTAGTG
rEF1	ACGCTTGAGATCCTTAACCGCAACATTCTT
fNbrbohB	TTTCTCTGAGGTTTGCCAGCCACCACCTAA

rNbrbohB	GCCTTCATGTTGTTGACAATGTCTTTAACA
A-26	GCC TGG AGA TAC ATG CAC ATT ACG GCT TTC CCT ATT AGA AGG TCT CAG GTG CGC GTT TCG GTA AGT AGA CGG GAC CAG TTC GCC
B-26	CGC GCA CCT GAG ACC TTC TAA TAG GGT TTG CGA CAG TCG TTC AAC TAG AAT GCC CTT TGG GCT GTT CCG GGT GTG GCT CGT CGG
C-26	GGC CGA GGA CTC CTG CTC CGC TGC GGT TTG GCG AAC TGG TCC CGT CTA CTT ACC GTT TCC GAC GAG CCA CAC CCG GAA CAG CCC
D-26	GCC GTA ATG TGC ATG TAT CTC CAG GCT TTC CGC AGC GGA GCA GGA GTC CTC GGC CTT TGG GCA TTC TAG TTG AAC GAC TGT CGC
A-26-Cy3	GCC TGG AGA TAC ATG CAC ATT ACG GCT TTC CCT ATT AGA AGG TCTCAGGTGCGC GTT TCG GTA AGT AGA CGG GAC CAG TTC GCC-Cy3
A-37-1	CCC TGT ACT GGC TAG GAA TTC ACG TTT TAA TCT GGG CTT TGG GTT AAG AAA CTC CCC G
A-37-2	CGC TGG AGG CGC ATC ACC GTT TGC GTA TGT GTT CTG TGC GGC CTG CCG TCC CGT GTG GG
B-37-1	CGG TGA TGC GCC TCC AGC GCG GGG AGT TTC TTA ACC CTT TCC GAC TTA CAA GAG CCG G
B-37-2	GCG AGA CTC AGG TGG TGC CTT TGG CAT TCG ACC AGG AGA TAT CGC GTT CAG CTA TGC CC
C-37-1	CCC ATG AGA ATA ATA CCG CCG ATT TAC GTC AGT CCG GTT TCC CAC ACG GGA CGG CAG GC
C-37-2	CGC ACA GAA CAC ATA CGC TTT GGG CAT AGC TGA ACG CGA TAT CTC CTG GTC GAA TGC C
D-37-1	GCC CAG ATT AAA ACG TGA ATT CCT AGC CAG TAC AGG GTT TCC GGA CTG ACG TAA ATC GG
D-37-2	CGG TAT TAT TCT CAT GGG TTT GGC ACC ACC TGA GTC TCG CCC GGC TCT TGT AAG TCG G
A-37-1-Cy3	Cy3-CCC TGT ACT GGC TAG GAA TTC ACG TTT TAA TCT GGG CTT TGG GTT AAG AAA CTC CCC G

Both the HT monomer and tetrahedron were assembled with four single stranded DNA oligonucleotides with certain complementary sequences to form the nanostructure size and shape. The tetrahedron DNA sequences were designed to create a final tetrahedron shape (triangular pyramid) with 2.4 nm edges when assembled through annealing of four pre-designed single stranded DNA oligonucleotides. The HT monomer structure was designed to contain a sticky end and a stem-loop hairpin structure, enabling co-polymerization with another monomer to assemble into the length-controlled 1D nanostring by introduction of an initiator (Fig. 31).

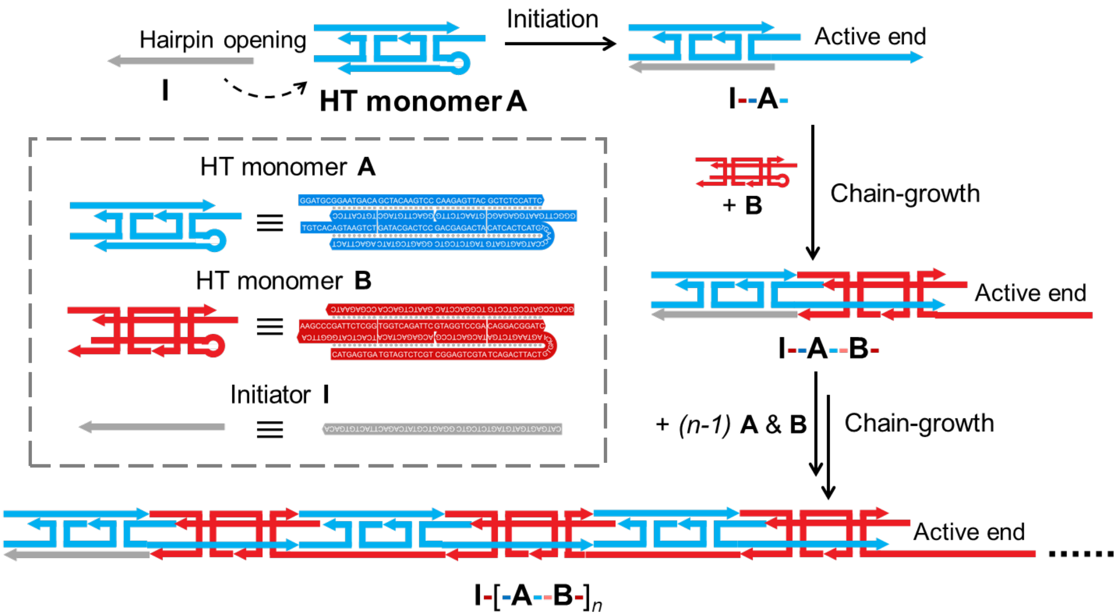

Figure 31. Toehold-mediated strand displacement reaction for nanostring synthesis.

Chain-growth supramolecular co-polymerization of nanostring from HT monomers A and B, initiated with I.

In detail, the initiator can open the hairpin loop structure of the monomer A through a toehold-mediated strand displacement reaction to produce a complex carrying a reactive terminus (I-A). The reactive terminus can invade the hairpin domain of monomer B and activate it with an exposed sequence identical to I (I-A-B), which will further activate monomer A. Subsequently, co-polymeric chain growth happens exclusively with sequential addition of monomers A and B to these active termini until monomers are consumed. We can tune the molar ratio of initiator I to monomers A and B to control the final average length of the nanostring. For the nanostring we employed in this study, the molar ratio of monomer to initiator was 10. As such, only 10% of monomers are activated by the initiator, followed by the chain growth reaction, until all monomers are consumed to form the nanostring with an average of 10 monomer subunits. In summary, we can tune the final length of the nanostring by changing the molar ratios of monomers with initiator I by keeping the concentration of monomers constant. AFM characterization in Figure 32 and 33 shows proper formation of the DNA nanostructures. As with any chain-growth polymerization reaction, it is common to obtain a distribution of lengths for the final product. In Figure 33c, we show the length distribution of HT monomer and nanostring, which follows a Gaussian distribution with means of 16 nm and 312 nm, respectively.

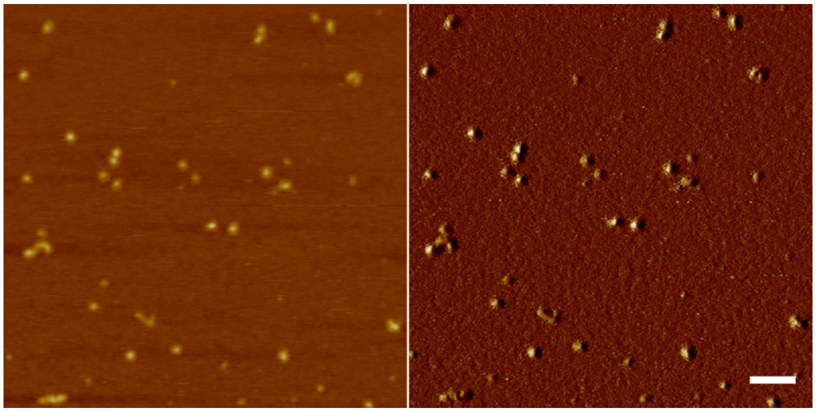

Figure 32. 2.4 nm tetrahedron nanostructure imaging.

AFM images of tetrahedron nanostructures. Left: height image; Right: phase image. Scale bar: 100 nm.

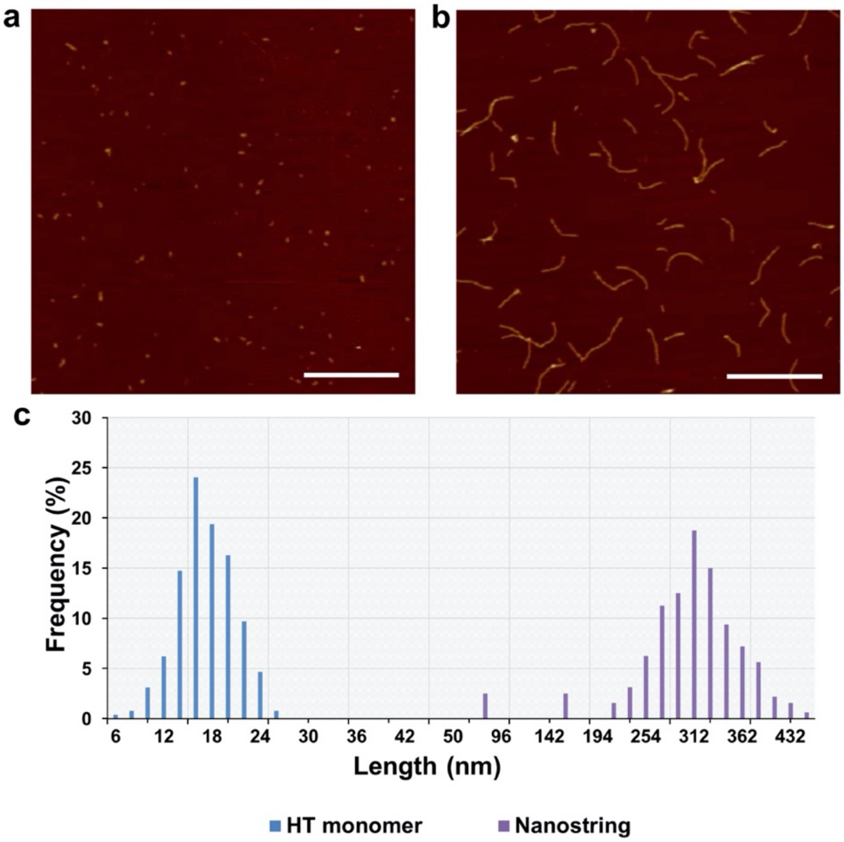

Figure 33. HT monomer and nanostring length distributions.

AFM height images of **a,** HT monomer and **b,** nanostring nanostructures. Scale bar: 500 nm. **c,** Statistical analysis of the HT monomer and nanostring length distribution from AFM images.

Each nanostructure was programmed to attach a biological cargo – DNA, RNA, or protein – to a predefined locus or loci through complementary base pair hybridization. As visualized in Figure 30, the tetrahedron contained one attachment locus at its apex, the nanostring contained ten attachment loci at the center of each of its constituent monomers, and the HT monomer contained one attachment locus either at its center (HT-c), or for a separate construct, an attachment locus at its side (HT-s). To confirm the accessibility of the attachment loci, streptavidin protein was attached to the siRNA attachment locus to visualize the conjugation site in the HT monomer and nanostring. AFM imaging revealed the predicted attachment of one streptavidin protein in the center or side of the HT-c or HT-s monomers, respectively, and ten streptavidin proteins per nanostring at the center of each constituent HT monomer (Fig. 30). Confirming the synthesis and attachment loci of the DNA nanostructures motivated an assessment of their internalization propensities into the cells of mature plant tissues.

4.4. Internalization Mechanism of DNA Nanostructures into Plant Cells

While the size exclusion limit set by the cell membrane is estimated to be around 500 nm, the plant cell wall has been reported to exclude particles larger than 5-20 nm[126]. Motivated by this figure of merit, we tested whether DNA nanostructures could internalize into the cells of *Nicotiana benthamiana* leaves without external aid (such as gene gun, electroporation, ultrasound, etc.). DNA nanostructures were fluorescently labeled *via* attachment of Cy3 labeled DNA strands to nanostructure attachment loci and infiltrated into the leaf abaxial side to assess cellular uptake in mGFP5 *Nicotiana benthamiana* transgenic plants (Fig. 34 and Fig. 35a). Confocal microscopy imaged both the Cy3 fluorescence of the nanostructures concurrently with the intrinsic cytosolic GFP fluorescence generated by the plant cells and provided a metric by which to assess relative internalization efficiencies of different nanostructures into plant cells. Colocalization of the Cy3 fluorescence (nanostructure) with the GFP fluorescence (plant cell cytosol) 12-hours post-infiltration was used to determine the extent of nanostructure internalization into the cell cytosol. Colocalization analysis in Figure 35b shows that the HT monomer and tetrahedron nanostructures exhibit a high degree of colocalization with the plant cell cytosol (59.5 ± 1.5% and 54.4± 2.7 % mean ± SD, respectively), while the nanostring showed a lower degree of colocalization (35.8 ± 0.9% mean ± SD) with the plant cell cytoplasm.

Figure 34. DNA nanostructure infiltration procedure photographs.

A small puncture on the abaxial surface of the leaf lamina was introduced with a pipette tip, and ~100 μL of the solution was infiltrated from the hole with a 1 mL needleless syringe by applying a gentle pressure, with caution not to damage the leaf.

Representative confocal microscopy images of colocalization are shown in Figure 35c, suggesting HT monomers and tetrahedron internalize into plant cells significantly more than nanostrings. We observe that a large portion of the Cy3 fluorescence from the Cy3-nanostring infiltrated leaves originates from nanostrings that are putatively stuck in the guard cells, which is the dominant contribution to the colocalization fraction calculated for nanostring internalization. Conversely, we observe that most of the Cy3 fluorescence recovered from Cy3-HT infiltrated leaves follows the cytosolic cell contour (the center of the cell is occupied by the vacuole, which is an organelle that occupies up to 80% of the cell volume in plants[160]), identified by cytosolic GFP expression (Fig. 35c).

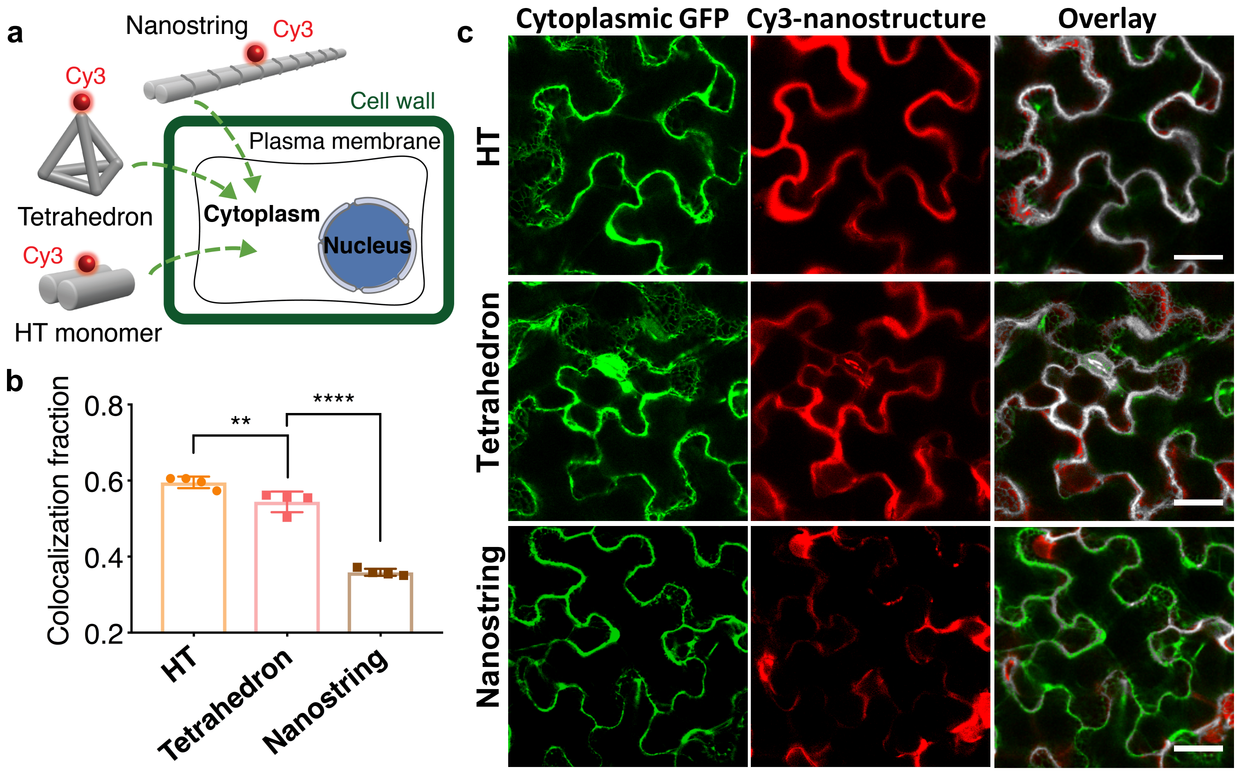

Figure 35. DNA nanostructure internalization into, and colocalization with, mGFP5 *Nicotiana benthamiana* cytoplasm.
a, Internalization of Cy3-tagged DNA nanostructures into mGFP5 *benthamiana* plant cells. **b,** Colocalization of Cy3 fluorescence (nanostructure) with GFP fluorescence (plant cell cytosol) 12-hours post-infiltration into mGFP5 *benthamiana* leaves. P** = 0.0041 and P**** < 0.0001 in one-way ANOVA. Error bars indicate s.e.m. (n = 4). **c,** Representative confocal images from data in (b) for HT, tetrahedron, and nanostring DNA nanostructures. Scale bars, 40 μm.

Free Cy3-oligonucleotides alone infiltrated into the leaves did not show significant colocalization with the cell cytoplasm (18.0 ± 4.6 % mean ± SD, Fig. 36). Moreover, we found that Cy3-labelled HT monomers can internalize into tobacco, arugula, and watercress plant leaf cells, whereby the nanostring again does not show significant internalization in these plant species (Fig. 37).

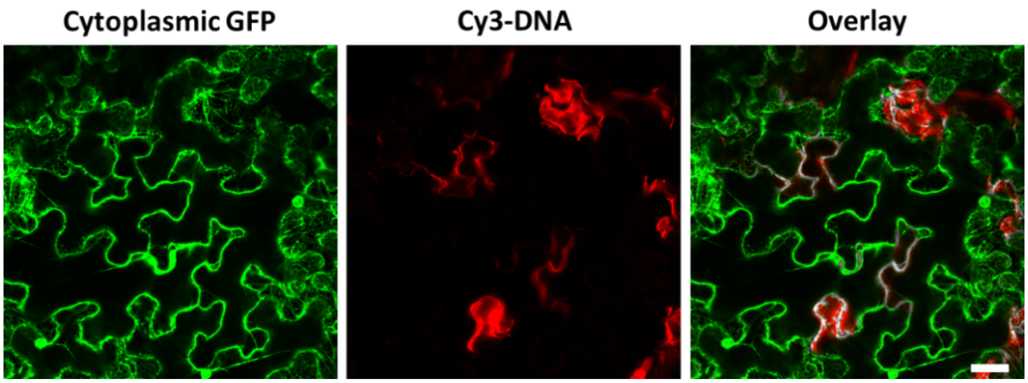

Figure 36. Free Cy3-labeled DNA oligonucleotides no not internalize into plant cells.
Representative confocal images of Cy3 labeled single stranded DNA colocalized with the GFP cytoplasm of mGFP5 *benthamiana*. Scale bars, 50 µm.

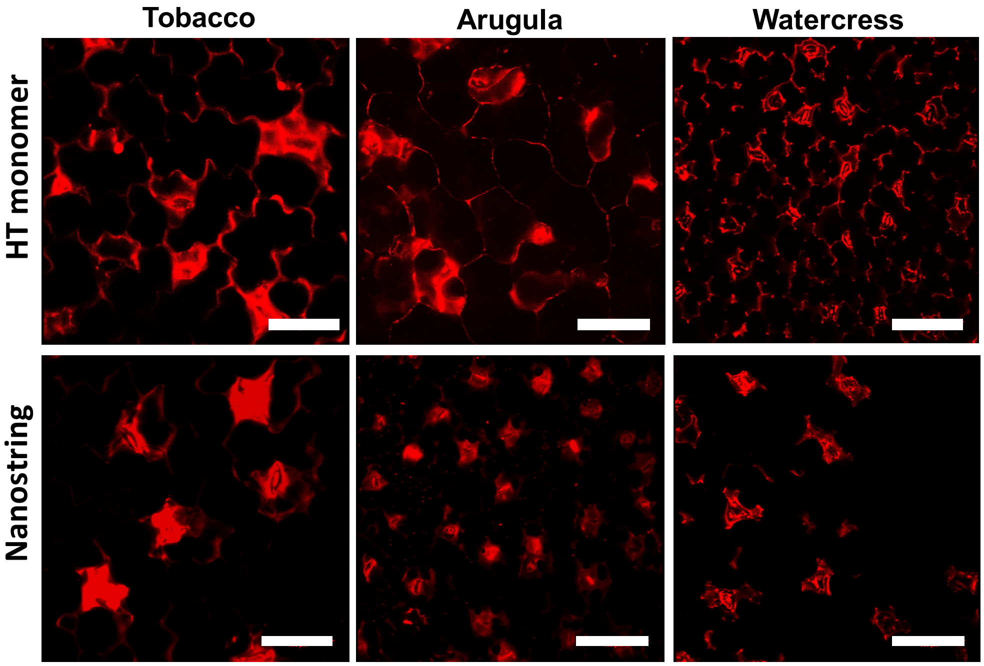

Figure 37. Internalization of Cy3 labeled HT monomer and Cy3 labeled nanostring into three different plant species.
Cy3-labeled HT monomer can enter tobacco, arugula, and watercress leaf cells, whereas the nanostring appears to be retained in the leaf guard cells and shows limited cellular internalization. Scale bars, 100 µm.

We next tested whether the cellular uptake mechanism is predominantly an energy-dependent or independent process by infiltrating the Cy3-labeled HT monomer into mGFP5 *Nicotiana benthamiana* plant leaves at either 20˚C or 4˚C, where at 4˚C, energy-dependent cellular uptake is reduced[161]. As shown in Figure 38, most of the Cy3-labeled monomer nanostructure is retained around the leaf stomata (guard cells) upon infiltration and incubation at 4˚C, whereas Cy3-labeled monomer nanostructures enter and diffuse uniformly into the cell cytoplasm if the infiltration and incubation is performed at 20˚C. Therefore, we propose that HT monomer nanostructures are uptaken through the plant cell membrane by an energy-dependent mechanism.

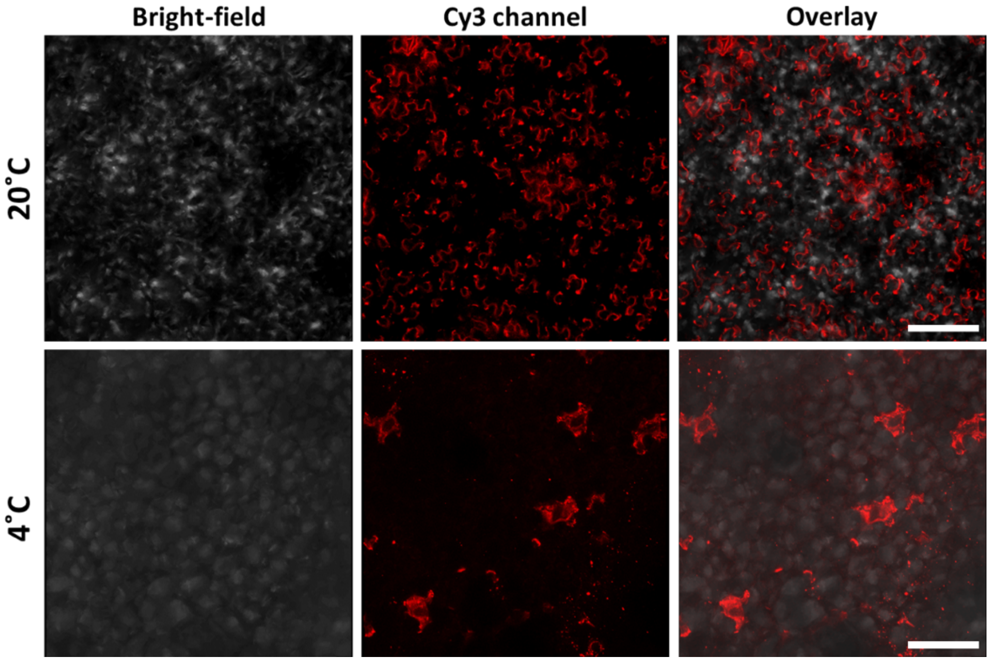

Figure 38. Nanostructure internalization into plant cells is temperature-dependent.

Representative confocal images showing the temperature dependence of nanostructure internalization for the Cy3 labeled HT monomer. Scale bars, 50 µm.

Furthermore, 3D z-stack analysis (Fig. 39) shows that the monomer diffuses approximately 50 µm in z direction, and 2-3 cm in x-y direction with a 100 µl infiltration, where the lateral diffusion length can be increased by increasing the infiltration volume.

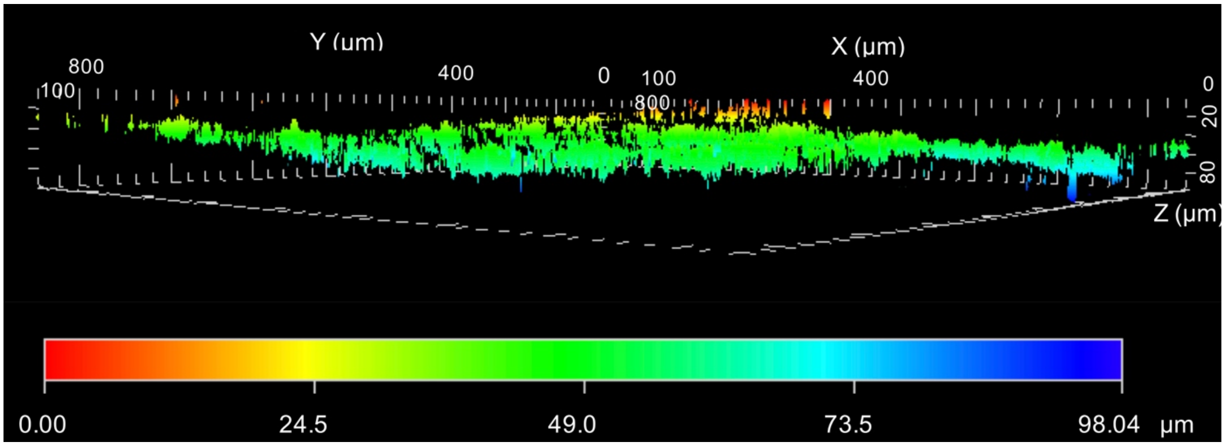

Figure 39. 3D z-stack analysis of the fluorescence profile of Cy3 labeled HT monomer treated *benthamiana* leaf.
Fluorescence originates from and diffuses ~50 µm into the leaf tissue (z direction), and 2-3 cm in the x,y direction for a 100 µl infiltration.

Subcellular localization analysis (Fig. 40) of Cy3-labelled HT monomers in single plant cells (protoplasts) indicates that DNA nanostructures are located in the cell cytosol and are excluded from the nucleus (Fig. 40a and c), a phenomenon that is also observed in plant leaf cells with high-resolution confocal imaging (Fig. 40b).

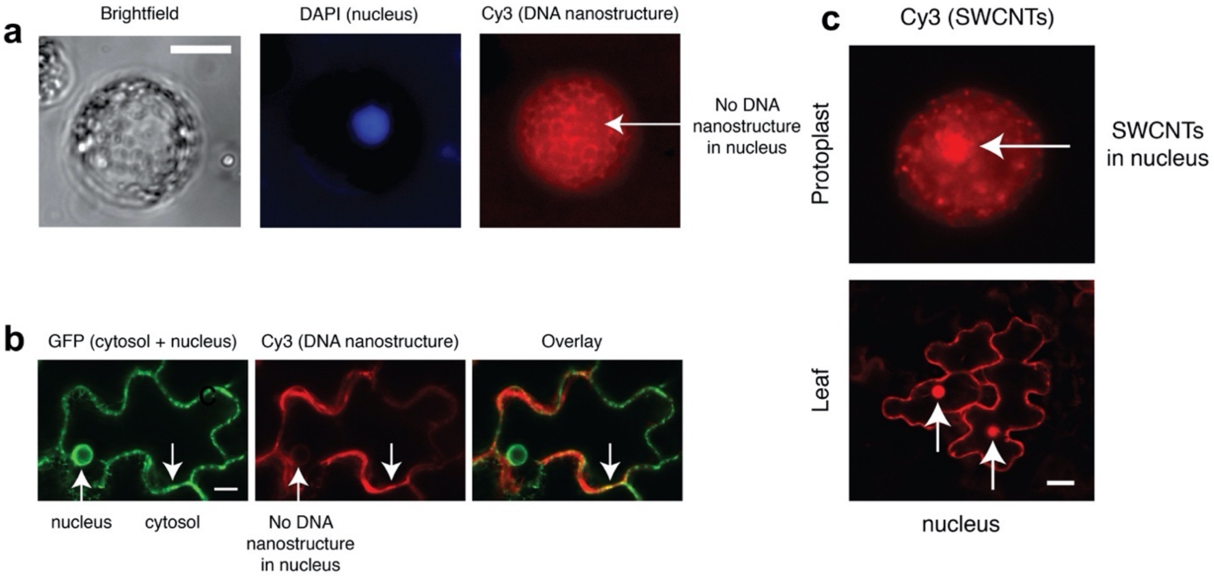

Figure 40. Subcellular localization of DNA nanostructures.
a, Cy3-labeled DNA nanostructures localize in the cell cytosol of *Nicotiana benthamiana* protoplasts and are excluded from the nucleus. Scale bar: 20 µm. **b,** High resolution confocal co-localization shows that Cy3-labeled DNA nanostructures infiltrated into mGFP5 *Nicotiana benthamiana* leaves only enter the cytosol of plant cells, and no Cy3 in the nucleus is observed. Scale bar: 20 µm. **c,** Cy3-labeled SWCNTs (to compare with DNA nanostructures) in protoplasts and intact leaves show SWCNTs can enter both the cell cytosol and nucleus 6-hours post-co-incubation and post-infiltration, respectively. Scale bar: 25 µm.

Prior work probing nanomaterial uptake in mammalian systems suggests uptake across the lipid bilayer is dependent on nanoparticle size, shape, aspect ratio, and mechanical stiffness[65]. We posit these parameters may also affect DNA nanostructure uptake across the plant cell wall. To better understand nanostructure parameters enabling plant cell internalization, we compiled and compared the size, compactness, aspect ratio (after conjugation with siRNA), and relative stiffness of the DNA nanostructures. Regarding size, as shown in Table 6 and Figure 41, we find that smaller nanostructures of the same shape internalize into plant cells significantly more than their larger-sized counterparts (tetrahedrons, 2.4 nm, 8.8 nm, or 12.6 nm), possibly because smaller nanostructures can remain below the plant cell wall size exclusion limit[61]. Specifically, we find an abrupt decline in the internalization efficiencies between the 8.8 nm and the 12.6 nm tetrahedrons, thus we estimate that the size cutoff for nanostructure internalization is approximately 10 nm.

Table 6: Calculation of DNA nanostructure parameters

Structures	Cross section (nm^2)	Length (nm)	Stiffness ($k_{structure}/k_{dsDNA}$)	Compactness ($C_{structure}/C_{sphere}$)	Co-localization	Aspect ratio w/ siRNA	
HT monomer	2 × 5	16	0.83	0.45	59.5 ± 1.5%	Center	1:1
						Side	5:1
Nanostring	2 × 5	320	1.0×10^{-4}	0.11	35.8 ± 0.9%	20:1	
8-helix	6 × 7.2	300	1.7×10^{-3}	0.19	52.7± 1.1%	-	

SWCNT	1 × 1	~500	GPa to TPa	-	54.2± 4.5 %	35:1
Tetra-7	-	2.4	-	0.55	54.4± 2.7 %	5:1
Tetra-26	-	8.8	-	0.55	47.7± 0.6 %	-
Tetra-37	-	12.6	-	0.55	36.6± 1.6 %	-

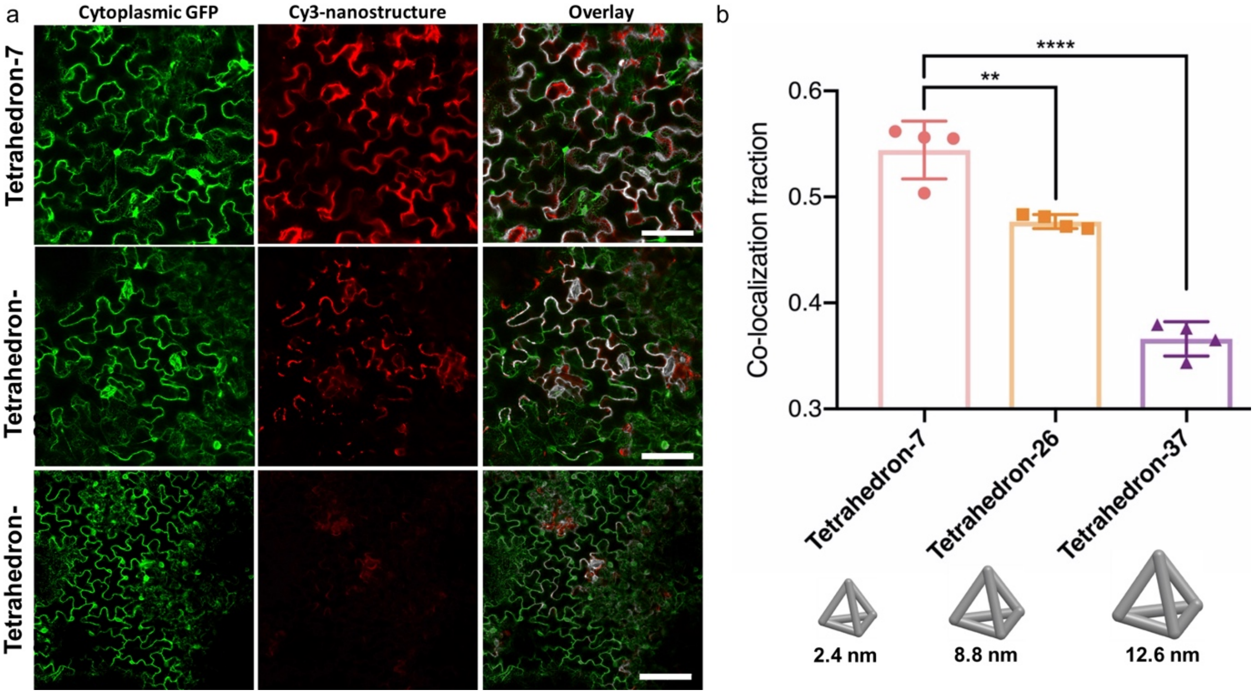

Figure 41. Cy3-labeled tetrahedron DNA nanostructure internalization into mGFP5 *Nicotiana benthamiana* leaf cells is size-dependent.

a, Representative post-infiltration confocal images of 2.4 nm, 8.8 nm, or 12.6 nm Cy3-labeled tetrahedron nanostructures in mGFP5 *benthamiana* leaves. Tetrahedron nanostructure size is inversely proportional to cellular internalization. Scale bars, 100 μm. **b,** Co-localization fraction of Cy3 fluorescence (nanostructure) with GFP fluorescence (plant cell cytosol) 12-hours post-infiltration into mGFP5 *benthamiana* leaves. P** = 0.0016 and P**** < 0.0001 in one-way ANOVA. Error bars indicate s.e.m. (n = 4).

Regarding compactness (Table 6), we calculated that the tetrahedron and HT monomer exhibit higher compactness than the nanostring (0.55 and 0.45 *vs.* 0.11, respectively). Our results indicate that nanostructures with higher compactness enable higher cellular uptake efficiency in mGFP5 *Nicotiana benthamiana* plants (59.5 ± 1.5 % for HT monomer, and 54.4± 2.7 % for tetrahedron, compared to 35.8 ± 0.9% for nanostring), consistent with internalization results of HT and nanostring into tobacco, arugula, and watercress leaves (Fig. 35 and 37), and some mammalian cell studies[162]. We also simulated the bending stiffness of aforementioned DNA nanostructure constructs, and again found that higher simulated bending stiffness correlates with higher plant cell uptake (Table 6 and Fig. 42). Based on the above results, we hypothesize that in addition to nanostructure size, the mechanical stiffness of the nanostructure plays an important role in nanostructure internalization into plant cells.

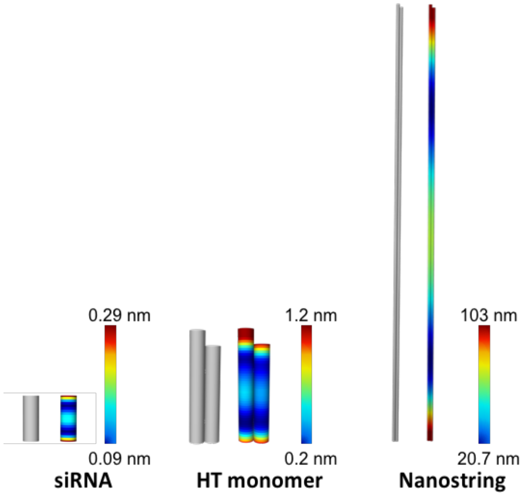

Figure 42. Simulation of DNA nanostructure bending stiffness.

Equilibrium conformation and heat map color range of root-mean-square fluctuations (RMSF) for the siRNA, HT monomer, and nanostring nanostructures, simulated by CanDo[163]. Blue and red represent low and high relative flexibility, respectively. Bluest = 0% RMSF and reddest = 95% RMSF.

To further explore this hypothesis, we tested the effect of nanostructure stiffness – with similar nanostructure shape on plant cell internalization by synthesizing nanostructures with different mechanical stiffnesses. We synthesized an 8-helix bundle DNA origami[164] with a similar length but of higher stiffness than the nanostring, and tested their relative internalization efficiencies upon infiltration in *Nb* plant leaf cells. Additionally, we tethered the nanostring to SWCNTs to test the effect of nanostructure stiffness for internalization into *Nicotiana benthamiana* plant cells. AFM, agarose gel characterization and near-infrared spectroscopy confirmed successful assembly of 8-helix bundles (Fig. 43) and nanostring-SWCNT conjugation (Fig. 44).

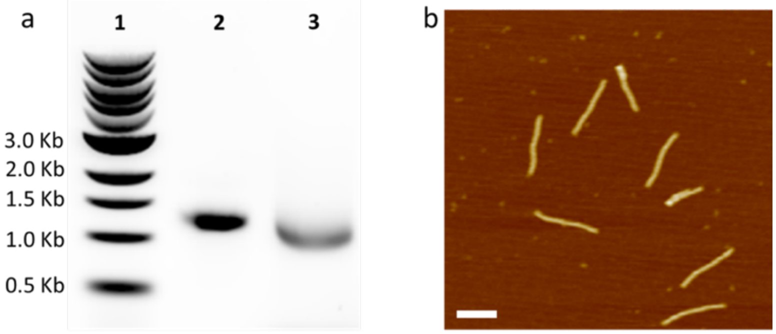

Figure 43. Validation of 8-helix DNA origami assembly.

a, 1% agarose gel confirming the successful assembly of 8-helix bundle DNA origami. Lane 1: 1kb DNA ladder, lane 2: M13 template ssDNA, lane 3: 8-helix bundles origami. **b,** AFM image of 8-helix bundle DNA origami. Scale bar, 200 nm.

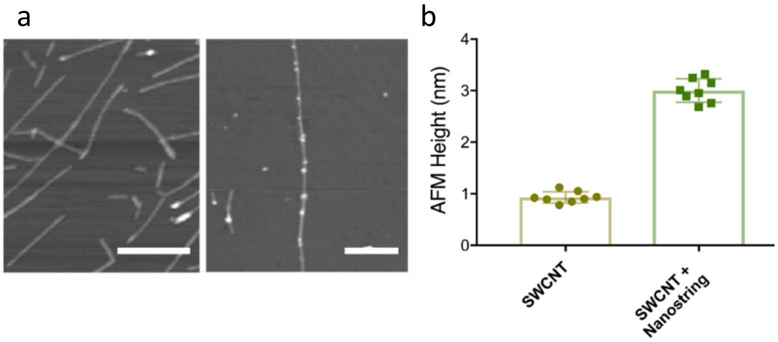

Figure 44. Confirmation of nanostring tethering to SWCNT.

a, Representative AFM images of SWCNT (upper left), SA-biotin nanostring conjugated SWCNT (upper right), and statistical height analysis of SWCNT (~1 nm) and SWNT-nanostring conjugation (~3 nm). Scale bars, 100 nm. **b,** SWCNT nIR fluorescence change with time when nanostrings hybridize to SWCNTs. **c,** SWCNT nIR spectra after adding different nanostring concentrations.

We chose to tether nanostrings to SWCNTs because SWCNTs have a small ~1 nm diameter but exhibit a stiffness on the order of hundreds of GPa to TPa, approximately one thousand times stiffer than the nanostring nanostructure (several GPa[165]). Furthermore, SWCNTs have been shown to internalize into cells of a variety of plant species[42] (previous chapters), with a leading hypothesis that the larger tensile strength of the SWCNT compared to that of the plant cell wall facilitates needle-like plant cell internalization. Colocalization analysis (Fig. 45b and c) indicates that Cy3-labeled SWCNTs alone (54.2± 4.5%), 8-helix bundles with higher stiffness (52.7± 1.1%), as well as the nanostring-SWCNT conjugate (51.4 ± 4.5%) showed significantly higher plant cell internalization efficiency than the nanostring (35.8 ± 0.9%). These results suggest that higher DNA nanostructure stiffness, or tethering a flexible nanostring to the stiffer SWCNT, enables internalization into plant cells, despite the fact that the 8-helix bundles or nanostring-SWCNT conjugates are both slightly larger in diameter than either the nanostring or the SWCNT alone. Based on these results, we conclude that the nanostructure stiffness is a highly important design element for nanostructure internalization into plant cells. In summary, we find that smaller size, higher aspect ratio, and higher stiffness are all contributing figures of merit for nanostructure internalization into plant cells.

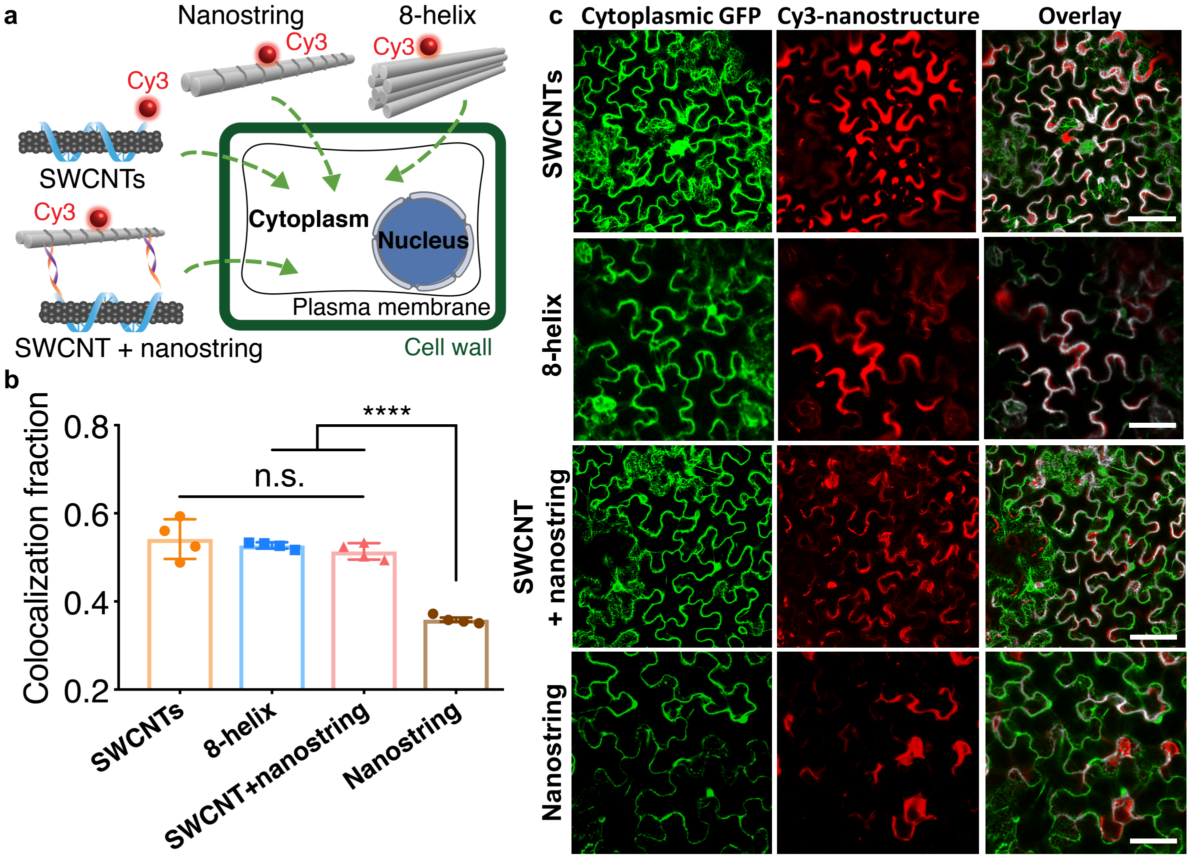

Figure 45. Internalization analysis of nanostructures with different mechanical stiffness into mGFP5 *Nicotiana benthamiana* cells.

a, Schematic depicting the proposed internalization of four different nanostructures post-infiltration into plant cells: SWCNTs wrapped by Cy3 labeled GT15 ssDNA, nanostrings labeled with Cy3 at the nanostring center and hybridized onto SWCNT, Cy3 labelled 8-helix bundles origami and the Cy3 labeled nanostring alone. **b,** Co-localization analysis of Cy3 fluorescence (indicating nanostructure) with the GFP fluorescence (indicating plant cell cytosol) after 12 hours (nanostring and 8-helix bundles) or 6 hours (SWCNTs and SWCNTs + nanostring) post-infiltration into mGFP5 *benthamiana* leaves. P**** < 0.0001 in one-way ANOVA, n.s.: not significant difference. Error bars indicate s.e.m. (n = 4). **c,** Representative post-infiltration confocal images showing different internalization behaviors of different nanostructures shown in part b) to mGFP5 *benthamiana* leaves. Scale bars, 70 µm.

4.5. Calculating Nanostructure Stiffness and Compactness

4.5.1. Calculation of relative nanostructure bending stiffness

The bending stiffness (k_b) of a beam-shaped structure is described by:

$$k_b = \frac{3EI}{L^3}$$

where *E* is Young's modulus (elastic modulus), *L* is the length of the DNA nanostructure, and *I* is the area moment of inertia.

To estimate the moment of inertia, we treat a 1D nanostructure as a bundle of *N* rigidly linked cylindrical rods of radius *r*, where *I* can be calculated in terms of *I*. The moment of inertia of each dsDNA helix with respect to its own center of mass is *i*, and is displaced from the nanostructure's center of mass by a distance *R*. By the parallel axis theorem, the moment of inertia of the dsDNA helix with respect to the nanostructure's center of mass is $i+MR^2$, where *M* is the mass of the helix. Assuming uniform density:

$$i = \frac{1}{2}Mr^2$$

and thus

$$I = N(i + MR^2) = N\left(i + 2i\frac{R^2}{r^2}\right)$$

with relative stiffness (Table 6):

$$\frac{k_b(nanostructure)}{k_b(dsDNA)} = \frac{I}{i} \times \left(\frac{L(dsDNA)}{L(nanostructure)}\right)^3 = N\left(1 + 2\frac{R^2}{r^2}\right) \times \left(\frac{L(dsDNA)}{L(nanostructure)}\right)^3$$

4.5.2. Structural conformation and mechanical stiffness simulation

The structural shape and mechanical compliance of siRNA, HT monomer, and nanostring were modeled using the finite element model with CanDo (cando-dna-origami.org) to predict the structural shape and mechanical flexibility of the DNA nanostructures. The nanostructures were modeled as homogeneous elastic rods with isotropic bending stiffness. The structural and mechanical parameters of two-node beam finite elements composing each rod are as:

- B-form DNA helix is modeled as a worm-like chain.
- Axial length per base pair: 0.34 nm;
- Helical diameter: 2.25 nm;
- Base pairs per turn: 10.5;
- Bending stiffness: 230 pN·nm^2;
- Stretching modulus: 1100 pN;
- Torsional stiffness: 460 pN·nm^2.

The backbone bending and torsional stiffness are reduced by 100-fold when there are nicks in the DNA double helix, and thus single-stranded DNA present as sticky ends or loops are modeled as entropic springs using a modified freely jointed chain model. Interhelical crossovers are treated as rigid component with zero length.

The structural conformation and mechanical stiffness of DNA nanostructures at ground-state solution are performed by normal mode analysis with CanDo. The thermal fluctuations are quantified using computing root-mean-square fluctuations (RMSF) of base pairs computed at a temperature of 298 K. Here, RMSF measures the magnitude of motion of base pairs and exhibit flexibility of DNA nanostructures.

4.5.3. Calculation of nanostructure compactness

The compactness of a 3D structure relates the enclosing surface area (A) with the volume (V) and can be defined by the ratio area$^{1.5}$/volume, which is dimensionless and can be minimized by a sphere.

The compactness of 3D structure: $C_{structure} = A^{1.5}/V$

For a sphere:

$$A_{sphere} = 4\pi r^2$$

$$V_{sphere} = \frac{4}{3}\pi r^3$$

The compactness of sphere: $C_{sphere} = {A_{sphere}}^{1.5}/V_{sphere} = 3\sqrt{4\pi}$

which is the minimum compactness of a solid since the sphere encloses maximum volume for a constant surface area.

The regular compactness is defined as: $C = C_{sphere}/C_{structure}$

C_{sphere} is the calculated value of a sphere, and $C_{structure}$ is the calculated value of the sphere DNA nanostructures.

4.6. siRNA-Mediated Gene Silencing Efficiency of DNA Nanostructures

In this section, we examined whether DNA nanostructures could be loaded with a functional biological cargo, siRNA, to accomplish gene silencing in plants. RNA interference is a phenomenon in which double stranded RNA (dsRNA) induces gene silencing, and has expedited discoveries in genomics and therapeutics[136]. A key conserved feature of RNAi in plants is processing of dsRNA into siRNAs by the activity of Dicer-like enzymes. siRNAs are subsequently incorporated into an RNA-induced silencing complex (RISC), resulting in sequence-specific blocking of mRNA translation. RNAi has emerged as a powerful strategy to engineer disease resistance against pests and pathogens in plants and has facilitated plant biosynthetic pathway mapping.

To ascertain whether DNA nanostructures can deliver siRNA and achieve gene silencing in plants, we targeted the silencing of a GFP gene in transgenic mGFP5 *Nb*, which exhibits strong constitutive GFP expression from the nuclear genome. We designed a 21-bp siRNA sequence that inhibits GFP expression in a variety of monocot and dicot plants[166], and hybridized this duplex oligonucleotide to a complementary strand programmed into the site-specific loci on the DNA nanostructures. Native polyacrylamide gel electrophoresis (PAGE) or agarose gel electrophoresis analysis (Fig. 46) was performed to validate conjugation of siRNA to each DNA nanostructure.

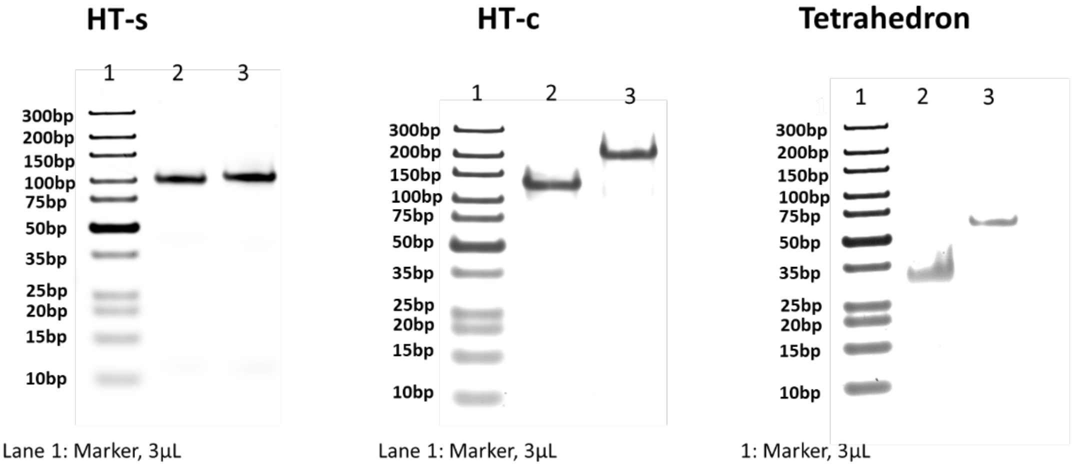

Lane 1: Marker, 3µL
Lane 2: HT-s, 1µM, 5µL
Lane 3: HT-s + siRNA, 1µM, 5µL

Lane 1: Marker, 3µL
Lane 2: HT-c, 1µM, 5µL
Lane 3: HT-c+ siRNA, 1µM, 5µL

1: Marker, 3µL
2: tetrahedron, 1µM, 3µL
3: lane 2 tetrahedron + 1 siRNA, 1µM

Figure 46. Validation of HT-s, HT-c, and tetrahedron attachment of siRNA.
10% Native-PAGE gels to verify attachment of siRNA to HT monomer and tetrahedron at different loci.

Furthermore, we confirmed that loading on DNA nanostructures protects the siRNA from degradation inside the cells compared to free siRNA (Fig. 47), and that the DNA nanostructures remain stable in various biological media for at least 12 hours (Fig. 48), motivating their use in plant tissues.

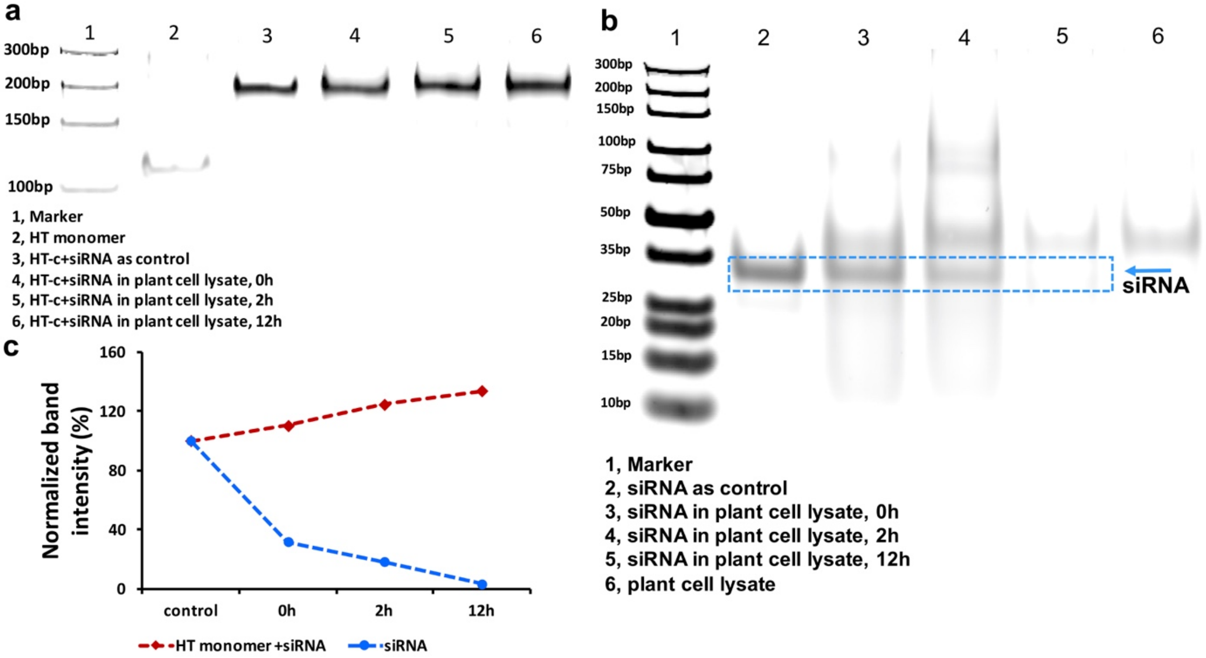

Figure 48. DNA nanostructures protect siRNA from nuclease degradation in plant cell lysate.
a, 10% Native-PAGE gel showing of siRNA attached to HT monomer and exposed to plant cell lysate, showing protection from degradation. **b,** siRNA alone is completely degraded 12 hours following exposure to plant cell lysate. **c,** Normalized band intensity analysis of the gels in part a) and b) where 100% band intensity is defined as the siRNA without the plant cell lysate. Upward deviations from 100% are due to nonspecific protein adsorption to nanostructures and slightly increasing the band width and optical density.

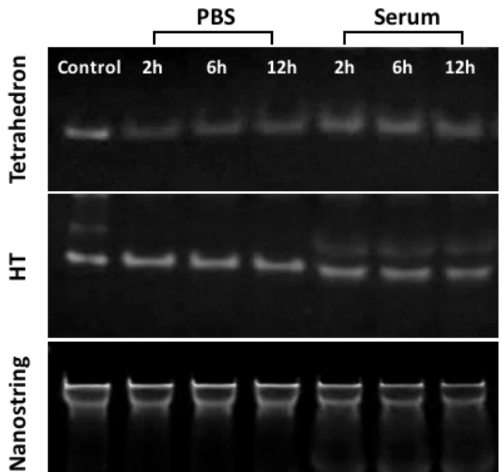

Figure 47. DNA nanostructure stability in PBS and serum.
10% Native PAGE gels show stability DNA nanostructures remain stable in different media over 12 hours of incubation.

Following siRNA loading, each nanostructure with its linked active siRNA duplex(es) was introduced into the leaves of mGFP5 *Nb via* infiltration to the leaf abaxial side for GFP gene silencing experiments, with an siRNA concentration of 100 nM (Fig. 49). Confocal microscopy was performed to image GFP expression in infiltrated leaves, and western blotting was utilized as a second method to confirm and quantify GFP expression changes in the infiltrated leaf tissues. As shown in representative confocal images in Figure 49b, untreated control leaves or leaves treated with free siRNA alone showed strong GFP fluorescence (low or no gene silencing), as expected, due to constitutive expression of GFP in the transgenic plant. Conversely, leaves infiltrated with siRNA-linked DNA nanostructures showed varying degrees of reduced GFP fluorescence 3-days post-infiltration. Specifically, as shown in Figure 49c, leaves infiltrated with siRNA functionalized nanostrings showed a ~29% ± 4.6% decrease of GFP fluorescence compared to the untreated leaf. Leaves infiltrated with the HT monomer showed a 41% ± 5.4 % or 47% ± 4.7% reduction in GFP fluorescence for constructs in which the siRNA was linked at the center or side of the nanostructure, respectively. Lastly, leaves infiltrated with siRNA conjugated to the tetrahedron showed a 42% ± 6.5 %, decrease in GFP fluorescence intensity compared to untreated leaves (Fig. 49c). Notably, all leaves infiltrated with siRNA functionalized DNA nanostructures exhibited a significantly larger fluorescence decrease compared to leaves infiltrated with free siRNA, suggesting that DNA nanostructures can serve as a nucleotide delivery tool in plant systems.

We note that the degree of nanostructure internalization (Fig. 45) is proportional to the silencing efficiency achieved with each nanostructure (Fig. 49), suggesting that nanostructure internalization into the plant cell determines its ability to induce siRNA-based gene silencing. Interestingly, we observe higher (47% ± 4.7 %) gene silencing efficiency when siRNA is linked to the side of the HT monomer (HT-s, aspect ratio 5:1), compared to a lower (41% ± 5.4 %) silencing efficiency when siRNA is instead linked to the center of the HT monomer (HT-c, aspect ratio 1:1). These results are congruent with prior studies suggesting that higher aspect ratio nanostructures facilitate nanoparticle entry into cells[126]. However, the nanostring, which has the highest aspect ratio (20:1), surprisingly shows the lowest silencing efficiency (29% ± 4.6%) and internalization efficiency (35.8% ± 0.9 %), corroborating our above findings that nanostructure shape is not the only parameter affecting internalization into plant cells. In particular, above internalization assays show nanostring internalization into plant cells *only* if the nanostring is first conjugated to a high stiffness nanostructure such as a SWCNT, confirming that nanostructure stiffness is an important parameter for both nanostructure internalization and gene silencing efficiency.

To further confirm siRNA-induced gene silencing, GFP expression in each plant leaf was quantified by western blotting 3 days post-infiltration with the siRNA-linked nanostructure. As shown in Figure 49d, the HT monomer and tetrahedron nanostructures linked with siRNA show a significant decrease in GFP compared to untreated leaves: 37% ± 4.3 % GFP decrease for HT-c, 49% ± 3.8 % decrease for HT-s, and 40% ± 1.9% decrease for the tetrahedron. Interestingly, the siRNA conjugated to the end of the HT monomer nanostructure showed the best silencing efficiency and the most GFP decrease, which was significantly higher than when the siRNA was instead conjugated to a locus on the *center* of the HT monomer. Moreover, we observed no statistically significant silencing by the siRNA loaded nanostring compared to siRNA alone.

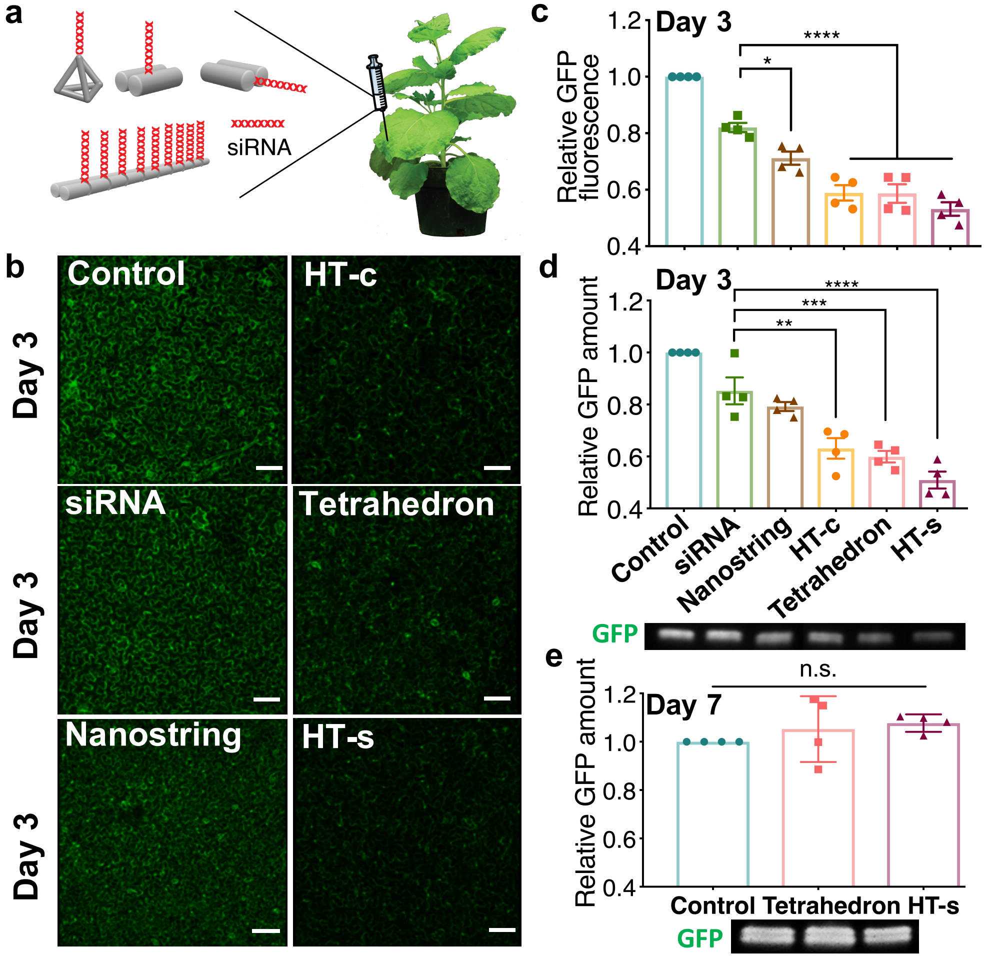

Figure 49. Transient gene silencing with siRNA tethered on DNA nanostructures.

GFP silencing efficiency of siRNA-linked nanostructures quantified by confocal imaging and western blotting. **a,** Infiltration of siRNA linked DNA nanostructures into mGFP5 *Nicotiana benthamiana* leaves. **b,** Representative confocal images of leaves infiltrated with siRNA-nanostructures 3-days post-infiltration, with non-treated control leaves. Scale bars, 100 µm. **c,** Fluorescence intensity analysis of confocal images. *P = 0.0151 and ****P < 0.0001 in one-way ANOVA. **d,** Representative western blot gel and statistical analysis of GFP extracted from nanostructure treated leaves 2-days post-infiltration. ** P = 0.0013, *** P = 0.0003 and **** P < 0.0001 in one-way ANOVA. **e,** Representative western blot gel of GFP extracted from leaves treated with siRNA linked to tetrahedron or HT-s nanostructures 7-days post-infiltration. Control vs. tetrahedron = not significant (p = 0.5806), Control vs. HT-s = not significant (p = 0.3444). All error bars indicate s.e.m. (n = 4).

We also tested the transience of the nanostructure-enabled siRNA mediated gene silencing. Confocal imaging shows that GFP fluorescence for all siRNA-loaded DNA nanostructure treated leaves recovers to pre-infiltration or non-infiltration (control) levels by 7-days post-infiltration (Fig. 50). Transience of siRNA-mediated gene silencing was also verified by quantifying GFP expression with quantitative western blot analysis. As shown in Figure 49e, the amount of GFP expressed in the leaves infiltrated with the HT-s monomer and tetrahedron nanostructures, which had induced the largest GFP silencing at day 3, returned to baseline protein expression levels by day 7.

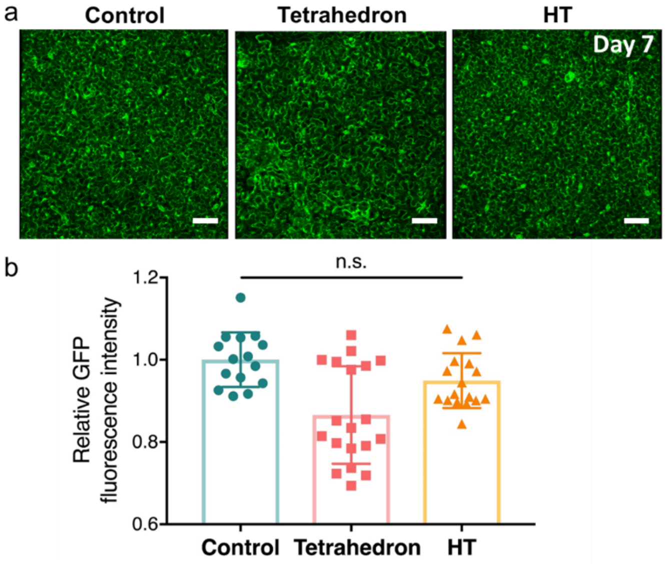

Figure 50. DNA nanostructure induced GFP silencing is transient.

a, Representative confocal images of mGFP5 *benthamiana* leaves 7-days post-infiltration with PBS, siRNA-tetrahedron nanostructures, or siRNA-HT momomer nanostructures, showing GFP fluorescence recovery. Scale bars, 100 µm. **b,** Quantitative fluorescence intensity analysis of confocal images. n.s.=non-significant (s.d. n = 15).

4.7. Cost Calculation and Considerations for DNA Nanostructures

Notably, DNA nanostructures and their relevant chemistries for gene silencing are significantly cheaper (less than a dollar per infiltration) compared to biolistic RNA delivery, and hence could be scaled-up for large scale experiments, or periodically re-applied to sustain the silencing if needed.

DNA nanostructures are relatively inexpensive when compared to other methods of siRNA delivery (for example gene gun). We calculated the cost of one infiltration (100 nM, 100 µl) for silencing with different nanostructures used in this study to estimate the cost and scalability of our DNA nanostructure platform (Table 7). We show that the total cost of one silencing experiment with tetrahedron, HT monomer, and nanostring is less than one US dollar ($0.53, $0.58 and $0.65, respectively), which is comparatively affordable and is amenable for scale-up if needed. However, we show that the cost is significantly higher for the 8-helix bundle origami for one silencing experiment ($50) due to the high cost of DNA materials to form the 8-helix bundle structure.

Table 7: Calculation of the cost of one infiltration of RNA loaded DNA nanostructures

Structures	DNA ($)	RNA ($)	Buffers ($)	Consumables ($)	Total ($)
Tetrahedron	0.024	0.291	0.01	0.2	0.525
HT monomer	0.077	0.291	0.01	0.2	0.578
Nanostring	0.148	0.291	0.01	0.2	0.649
8-helix bundles*	42.02	0.291	0.015	8.2**	50.52

* experiments not done, just for cost comparison

** higher consumable cost due to spin filtration required to purify the 8-helix bundle origami

4.8. siRNA Attachment Locus on Nanostructures Affects Endogenous Gene Silencing Pathways

siRNA mediated gene silencing in plants is a well-known sequence-specific gene regulation mechanism. However, RNA silencing can undergo different gene silencing pathways. Specifically, post-transcriptional gene silencing employs microRNA and siRNA pathways for mRNA cleavage or translation repression. We tested the siRNA silencing mechanism of DNA nanostructures (Fig. 51a). Because degradation of transcriptional mRNA is the typical mechanism for gene silencing with exogenously introduced siRNA, we quantified changes in GFP mRNA with qPCR. GFP mRNA of mGFP5 *Nb* leaf tissues infiltrated with siRNA-linked nanostructures were quantified with qPCR 2-days post-infiltration. Interestingly, as shown in Figure 51b, only siRNA alone and siRNA tethered to the tetrahedron showed a significant (22.3% ± 2.2 % and 50.3% ± 4.9 %, respectively) reduction in GFP mRNA. In contrast, the siRNA tethered to HT monomer or nanostring nanostructures showed a significant *increase* in GFP mRNA of 59.1%± 6.5 % for the side-linked monomer HT-s, 45.2% ±1.9 % for the center-linked monomer HT-c, and 35.1% ± 3.2 % for the nanostring. We further confirmed that the DNA nanostructure alone (HT monomer without siRNA) does not induce a change in leaf GFP mRNA levels (Fig. 52).

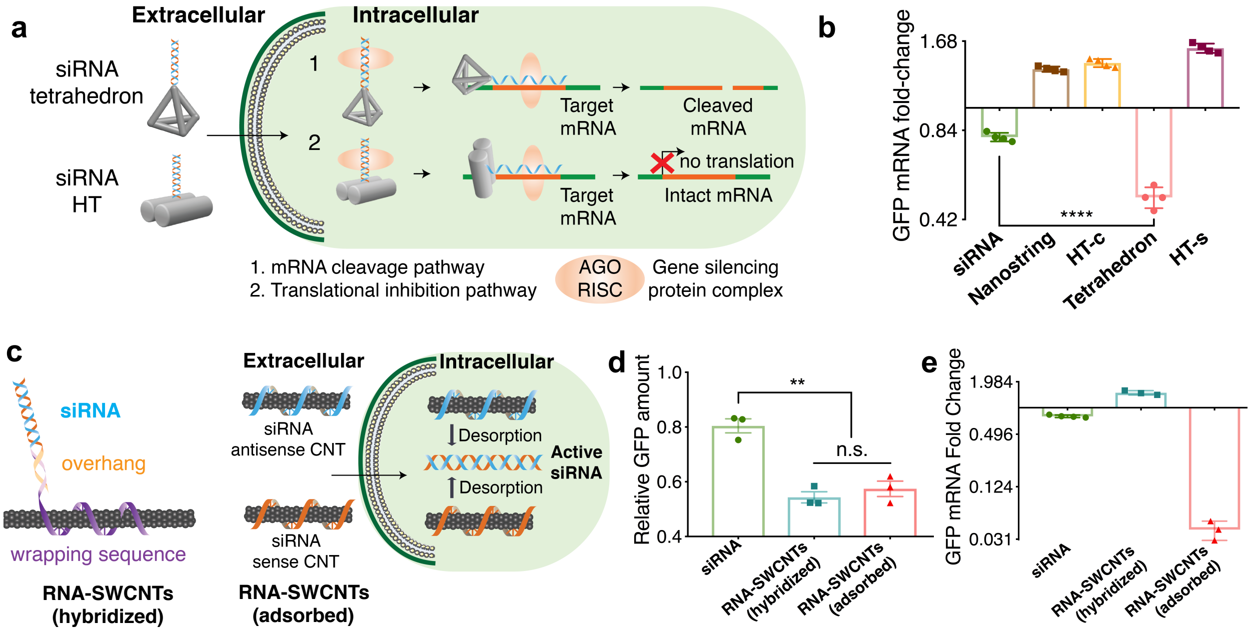

Figure 51. Gene silencing pathways for siRNA-linked nanostructures.

a, Proposed silencing pathways induced by siRNA-conjugated to DNA nanostructures. **b,** qPCR of leaves infiltrated with free siRNA, siRNA-nanostring, HT-c, tetrahedron, or HT-s nanostructures 2-days post-infiltration. P **** < 0.0001 in one-way ANOVA. Error bars indicate s.e.m. (n = 4). **c,** Hybridization or adsorption-based siRNA loading on SWCNTs. **d,** GFP extracted from siRNA-SWCNT treated leaves 2-days post-infiltration as measured with western blotting. **P = 0.0041, n.s.: non-significant in one-way ANOVA. Error bars indicate s.e.m. (n = 3). **e,** qPCR of leaves infiltrated with free siRNA, hybridized RNA-SWCNTs, and adsorbed RNA-SWCNTs 2-days post-infiltration, error bars indicate s.e.m. (n = 3).

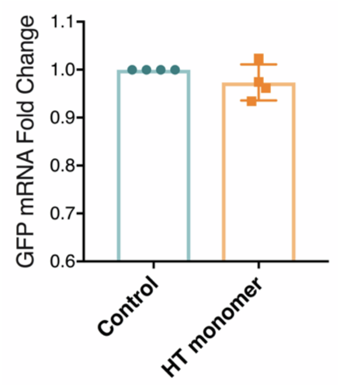

Figure 52. DNA nanostructure-induced silencing requires siRNA loading.

qPCR of leaves infiltrated with HT monomer alone (no siRNA loading) 2-days post-infiltration shows no mRNA change, as expected. Error bars indicate s.e.m. (n = 4).

The above results suggest that siRNAs conjugated to different DNA nanostructures employ different silencing pathways. Tetrahedron-mediated gene silencing appears to undergo an mRNA-targeted degradation pathway as does free siRNA, while siRNAs linked to either locus on the HT monomer may undergo translation inhibition based on the observed increase and accumulation in mRNA (Fig. 51a). Of note, the observed trend of increasing GFP mRNA was consistent with the silencing efficiency trends of the three nanostructures: the side-linked monomer (HT-s) showed the largest mRNA increase and also the largest GPF decrease as measured by western blotting and confocal microscopy. We thus hypothesize that steric and conformational hindrance of the siRNA, determined by the siRNA attachment locus, affects the resulting gene silencing pathway. Specifically, we find that siRNA tethered to the 1D nanostructures (HT, nanostring) have greater steric hindrance than when tethered to the apex of the 3D tetrahedron nanostructure.

To further probe the effect of siRNA linking geometry on gene silencing and to test the above hypothesis, we probed GFP-targeted siRNA silencing efficiency under two different siRNA linking geometries. Because SWCNT have been previously shown to internalize into plant cells without external aid[167], and it is possible to control the attachment geometry with SWCNTs, we attached siRNA to the surface of a 1D SWCNT with two different attachment configurations: siRNA was either tethered to the surface of a 1D SWCNT (RNA-SWCNTs hybridized) with greater steric hindrance resembling the case of the HT monomer, or reversibly loaded on the SWCNT in a releasable manner (RNA-SWCNTs adsorbed), exhibiting less or no conformational hindrance and thus resembling the case of the tetrahedron (Fig. 51c). Both constructs were introduced into mGFP5 *Nb* leaves and assessed for GFP silencing efficiency. Both siRNA attachment configurations show similar levels of GFP decrease as quantified by western blotting 2-days post-infiltration (Fig. 51d and 53): siRNA hybridized to SWCNT decreased GFP expression by 54.3% ± 1.7 %, and siRNA absorbed onto but releasable from the 1D SWCNT decreased GFP expression by 48% ± 4.8 %. However, qPCR assessment reveals that GFP mRNA *increases* by 48.4% ± 8.5 % if the siRNA is hybridized to the SWCNT, whereas the GFP mRNA *decreases* by 92% ± 1.0 % if the siRNA is releasable from the

SWCNT surface (Figure 51e). These results suggest both the silencing efficiency and silencing pathway are affected by the siRNA loading geometry on the nanostructure carrier and the availability of siRNA to the requisite endogenous gene silencing proteins.

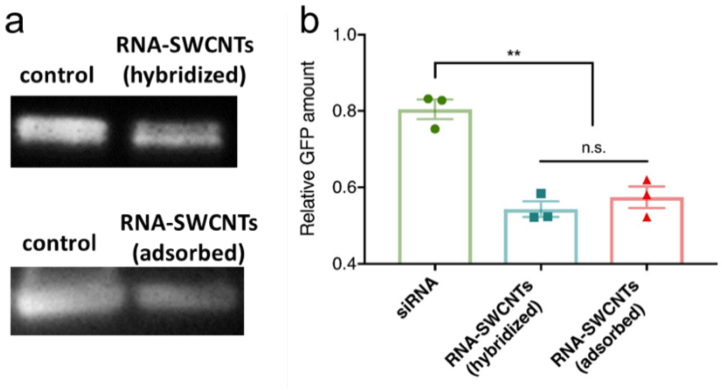

Figure 53. siRNA attachment configurations to SWCNT do not affect GFP protein silencing levels.

a, Representative western blot gel and analysis showing GFP extracted from free siRNA, siRNA attached SWCNTs through hybridization, or siRNA adsorbed to SWCNT 2-days post-infiltration to mGFP5 *benthamiana*. **b,** Statistical analysis of the results showing GFP proteins extracted from different SWCNT-treated leaves 2-days post-infiltration. P** = 0.0041 in one-way ANOVA. Error bars indicate s.e.m. (n = 3).

4.9. DNA Nanostructure Toxicity Analysis

DNA nanostructures have been broadly employed for intracellular delivery in mammalian cells due to their unique programmability, and their inherent biocompatibility compared to inorganic nanomaterials[168]. Most prior work comes to a consensus that DNA based nanostructures do not exhibit toxicity towards mammalian systems[169]. Since DNA nanostructures have not been used in plant systems to-date, we assessed whether DNA nanostructures are biocompatible in plants. Specifically, we chose to monitor the expression of the NbrbohB gene. Following infiltration of *Nb* leaves with either PBS buffer, HT monomer, tetrahedron, or nanostring nanostructures, mRNA of NbrbohB was measured and normalized with respect to the EF1 gene. Leaves infiltrated with either of the DNA nanostructures does not result in NbrbohB gene upregulation compared to adjacent areas within the same leaf treated only with PBS buffer (Fig. 54). Furthermore, the structural integrity of the plant cells is unperturbed by introduction of the various DNA nanostructures. The analyses suggest that DNA nanostructures do not induce a stress response in plants and are a biocompatible mode of siRNA delivery to plant cells.

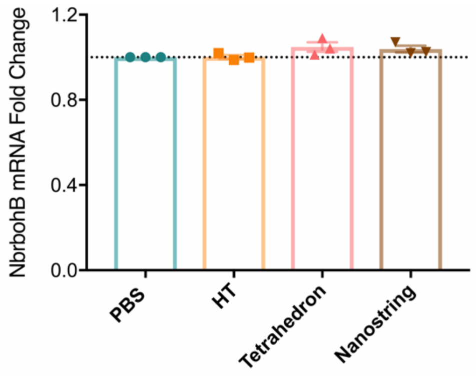

Figure 54. Plant stress gene NbrbohB is not upregulated by DNA nanostructures.

qPCR of NbrbohB, a known stress gene, shows nanostructures used to deliver siRNA do not induce a stress response when infiltrated into *Nicotiana benthamiana* leaves. Error bars indicate s.e.m. (n = 3).

4.10. Discussion

DNA nanostructures have been extensively studied in animal systems for cell internalization, intracellular delivery, and for downstream diagnostic and therapeutic applications owing to their unique sequence-structure programmability and inherent biocompatibility. Prior work has focused on studying DNA nanostructure internalization in mammalian cells, and has revealed that nanostructure size, shape, charge, and stiffness or compactness can influence the cellular internalization and uptake pathway. Analogous work in plant systems is lacking, where a few studies have reported the biolistic or non-mechanical uptake, translocation, or localization of engineered nanoparticles (carbon nanotubes[167], SiO_2[106], quantum dots, TiO_2 NPs) to plants[170], while DNA nanostructure use in plants remains unexplored. Orthogonally, gene silencing through the introduction of siRNA has become a broadly-adopted tool to inactivate gene expression, to probe biosynthetic pathways, and to serve as exogenous regulators of developmental and physiological phenotypes in plants.

In this chapter, I demonstrate that DNA nanostructures can effectively be designed to internalize into plant cells through infiltration, and that siRNA can be controllably tethered to specific loci on the DNA nanostructures for effective gene silencing in *Nicotiana benthamiana* leaves. We show that siRNA delivered by DNA nanostructures silences a transgene more effectively than siRNA delivered alone. We further find that the structural and mechanical properties (size, shape, compactness, and stiffness) of DNA nanostructures, and siRNA conjugation loci, affect not only nanostructure internalization into plant cells, but also subsequent gene silencing efficiency and gene silencing pathway. Once intracellular, siRNAs are processed by nucleases for assembly into the RNA-induced silencing complex (RISC). The RISC complexes with a single-strand of the siRNA duplex and guides the RISC complex to its complementary mRNA target where it will cleave, and thus inactivate, the target mRNA, effectively silencing the downstream protein product. Several forms of RISC that differ in size and composition have been reported[171], and are presumed to undergo mechanistic variations in their silencing pathways[172].

In this work, we find that the likely gene silencing mechanisms undertaken by siRNA linked to DNA nanostructures depend on the siRNA attachment locus and steric availability of the attached siRNA. Interestingly, siRNA tethered to small 3D nanostructures show gene silencing both at the transcript (mRNA) and protein levels, whereby siRNA attached to 1D nanostructures shows gene silencing at the protein level but shows an increase in mRNA transcript levels. This phenomenon of increased mRNA implies a possible silencing pathway and mechanism for siRNA delivered with HT or nanostring DNA nanostructures, in which translational inhibition of GFP expression is preferred over direct mRNA cleavage. We hypothesize that protein translation inhibition leads to continuous production and accumulation of repressed mRNAs, as we observe through qPCR of leaves treated with select nanostructure carriers. Specifically, we hypothesize that the steric accessibility of siRNA conjugated to different DNA nanostructures by endogenous silencing proteins plays a dominant role in determining the silencing mechanism, whereby formation of the RISC protein complex that leads to mRNA cleavage may be hindered by the proximity of a nanostructure scaffold for 1D nanostructures, but absent for small 3D nanostructures.

In summary, DNA nanostructures can serve as effective scaffolds and nanoscale vehicles for siRNA delivery to plants for efficient gene silencing. This work establishes DNA nanostructures as a programmable toolset for the delivery of exogenous biomolecules such as siRNA to plants and establishes guidelines for the design of DNA nanostructures for effective uptake into plant cells for various applications in plant biotechnology.

4.11. Materials and Methods

Chemicals and materials. Super purified HiPCO SWCNTs (Lot # HS28-037) were purchased from NanoIntegris and used for all SWCNT-based experiments. The following chemicals were purchased from Sigma-Aldrich: sodium chloride, potassium chloride, magnesium chloride hexahydrate, bovine serum albumin (heat shock fraction). Single stranded RNA and DNA oligonucleotides were purchased from and purified by Integrated DNA Technologies, Inc. (IDT); DNA oligonucleotides labeled with biotin or Cy3 were purified by HPLC and dissolved in Milli-Q water before use. The concentration of each strand was estimated by measuring the UV absorbance at 260 nm using a UV-3600 Plus UV-Vis-NIR Spectrophotometer (Shimadzu Scientific Instruments, Columbia, U.S.A.). Streptavidin was purchased from Sigma-Aldrich Co. LLC. UltraPure DNase/RNase-free distilled water from Invitrogen was used for qPCR experiments, and EMD Millipore Milli-Q water was used for all other experiments.

Plant growth. Transgenic mGFP5 *Nicotiana benthamiana* (obtained from the Staskawicz Lab, UC Berkeley), tobacco, arugula, and watercress seeds were germinated and kept in SunGro Sunshine LC1 Grower soil mixture for four weeks before use. Plants were allowed to mature to 3-4 weeks of age within the chamber before experimental use.

Infiltration of leaves with nanomaterials (SWCNTs and DNA nanostructures). 4-week-old mGFP5 *Nicotiana benthamiana* plants were punctured on the abaxial surface of the leaf lamina with a razor, and 100 μL of DNA nanostructure solutions were infiltrated through the puncture with a 1 mL needleless syringe. Post-infiltration, leaves were left in plant pots and analyzed after above-mentioned periods of time (6 or 12 hours, 2-3-days or 7-

days post-infiltration) to quantify nanostructure internalization or GFP gene silencing efficiency. Nanostructure internalization efficiencies (calculated with colocalization analysis), and gene silencing efficiency (calculated with GFP fluorescence intensity analysis, qPCR, and western blotting) were subsequently performed as described below.

Non-denaturing polyacrylamide gel electrophoresis (PAGE). 1 μM, of a 5 μL volume of each assembled sample was loaded onto a 10% PAGE (19:1 acrylamide/bisacrylamide in 1×TAE/Mg^{2+} buffer). Gels were run at 100 V (constant voltage) for two hours with an electrophoresis apparatus (Bio-rad, United States). Next, gels were stained with 1× SYBR® Gold nucleic acid dye (Thermo Fisher Scientific, United States) and scanned with a Typhoon FLA 9500 instrument (GE Healthcare life Sciences, United States of America).

AFM characterization. 2-3 μL of the DNA nanostructures (Tetrahedron, HT monomer and nanostring) sample was deposited on a freshly cleaved mica surface and left to adsorb on the surface for 3 minutes. For AFM imaging, the mica surface was slowly rinsed with water three times (each time with 10 μL water) to remove salt. Next, the mica surface was dried with a mild air stream by an ear-washing bulb and was imaged with a MultiMode 8 AFM with NanoScope V Controller (Bruker, Inc.) under tapping mode in air. All AFM images were analyzed by NanoScope Analysis v1.50.

Biotin-streptavidin binding assays. The strand H1-biotin was purchased and synthesized by IDT with biotinylation at the 5′ end. After the biotin labeled TH monomer or nanostrings were constructed as described before, a stoichiometric amount of streptavidin in 1×TAE/Mg^{2+} buffer was added, and the final molar ratio of streptavidin to biotin-nanofilament was 10:1. The mixture was left at room temperature for 5 min and then characterized by AFM as described above.

Self-assembly of DNA tetrahedral nanostructure. The corresponding oligonucleotides of A, B, C, D (see Table 4 for detailed sequences) were stoichiometrically mixed in 1×TM buffer (20 mM Tris, 50 mM $MgCl_2$, pH 8.0), then assembled through annealing with a PCR machine (Veriti™ 96-Well Thermal Cycler, Thermo Fisher, United States) at 95˚C for 10 min, followed by cooling down to 4˚C in 30 s. In detail, A-7, B-7, C-7 and D-7 assembled to form tetrahedron-7; A-26, B-26, C-26 and D-26 assembled to form tetrahedron-26; A-37-1, A-37-2, B-37-1, B-37-2, C-37-1, C-37-2, D-37-1 and D-37-2 assembled to form tetrahedron-37. For the tetrahedron with 15 nucleotide (nt) overhangs for siRNA conjugation, the A-15 stand was used instead of the A-7 strand. For the Cy-3 labeled tetrahedron, A-7-Cy3, A26-Cy3 and A-37-1-Cy3 were used instead during the annealing process.

Self-assembly of hairpin-tile (HT) monomer and 1D nanostring nanostructures. The oligonucleotides of H1, H2, H3, and H4 (see Table 4 for detailed sequences) were stoichiometrically mixed in a 1×TAE/Mg^{2+} buffer containing 40 mM Tris base, 20 mM acetic acid, 2 mM EDTA, and 12.5 mM magnesium acetate (pH 8.0). Next, the DNA strand solution was slowly cooled down from 95˚C to 20˚C over 24 hours in a water bath insulated in a Styrofoam box. To co-polymerize the 1D nanostrings, 1 μM of HT monomers A (H1, H2, H3, and H4) and B (H5, H6, H7, and H8) at equimolar concentrations were mixed with initiator strand I in a 1:0.1 ratio. The mixtures were further incubated at 20˚C for 1 h and were then characterized by AFM. For the Cy3-labeled HT monomer and nanostring, Cy3-H1 was used instead of strand H1. For the HT monomer and nanostring with 15-nt overhangs with siRNA conjugation at the center, the H1-15-RNA stand was used instead of the H1 strand. For HT monomer with 15-nt overhangs with siRNA conjugation at the side, H2-15-RNA stand was used instead of the H2 strand. For nanostring with 15-nt overhangs for SWCNTs conjugation, the H5-15-CNT stand was used instead of the H5 strand.

Hybridization of DNA nanostructures with double stranded siRNA. The duplex siRNA with 15-nt overhang was synthesized by mixing two completely complementary oligonucleotides (sense-15 and antisense strands in Table 4) in 1×TAE/Mg^{2+} buffer with further incubation for 1 h at 20˚C. Next, DNA nanostructures with overhangs were hybridized with the pre-formed siRNA duplex in PBS (137 mM NaCl, 2.7 mM KCl, 10 mM Na_2HPO_4, 2 mM KH_2PO_4, pH 7.4) at 37˚C for 30 minutes with a final concentration of 100 nM, allowing conjugation of siRNA to the DNA nanostructures. AFM characterization of nanostructure hybridization locus was performed by labeling each nanostructure locus with a biotin at the 5′ end of the core strand. Following co-incubation of the biotinylated nanostructure with streptavidin, AFM imaging was performed.

Preparation of SWCNTs with 15-nt overhang wrapped with DNA $(GT)_{15}$ -15 strand. We designed and prepared the GT_{15}-15 wrapped SWCNTs where the 15-nt overhangs were complementary to the 15-nt overhangs on the locus of each nanostring monomer, such that the SWCNT and nanostring would hybridize to each other (see detailed sequences in Table 4 and detailed protocols in methods below). To conjugate the SWCNT to the nanostring, the $(GT)_{15}$-15 strand was first dissolved at a concentration of 20 mg/mL in PBS buffer. 1 mg HiPCO SWCNTs was added to 400 μL of this DNA solution, followed by probe-tip sonication with a 3-mm tip at 50% amplitude (~7 W) for 20 min in an ice bath. The resulting solution was next centrifuged at 16,100g for 1 h to remove unsuspended SWCNT. Unbound (free) DNA was removed *via* spin-filtering (Amicon, 100 K) at 1,000g for 6 minutes (5 times) and the concentration of $(GT)_{15}$-15 wrapped SWCNTs was determined with a UV-Vis-nIR spectrometer where SWCNT concentration was calculated in mg/L (absorbance at 632 nm/extinction coefficient of 0.036).

Conjugation of nanostrings with $(GT)_{15}$-15 SWCNTs. Nanostrings with 15-nt hybridization overhangs which were fully complementary with the overhang of $(GT)_{15}$-15 were mixed with the filtered DNA wrapped SWCNTs in 0.5×TAE/Mg^{2+} buffer and incubated at 37˚C for 30 minutes. The conjugate was characterized with AFM by next adding streptavidin to bind to and indicate the biotin labeling position along the nanostring. To better differentiate the nanostring from the SWCNTs, same biotin-specific streptavidin strategy was employed for AFM characterization of the SWCNT-nanostring conjugate. As shown in AFM images, we observe discrete patterns of anchored streptavidin molecules on the surface of SWCNTs, which allowed direct visualization of the successful conjugation.

Quantitative GFP fluorescence intensity analysis of gene silencing. Infiltrated plant leaves were prepared for confocal imaging 3-days post-infiltration with corresponding nanomaterials by cutting a small leaf section of the infiltrated leaf tissue and inserting the tissue section between a glass slide and cover slip of #1 thickness. 20 µL of water was added between the glass slide and cover slip to keep the leaves hydrated during imaging. A Zeiss LSM 710 confocal microscope was used to image the plant tissue with 488 nm laser excitation and with a GFP filter cube. GFP fluorescence images were obtained at 10x magnification. Confocal imaging data was analyzed to quantify GFP expression across samples. For each sample, 4 biological replicates (4 infiltrations into 4 different plants) were performed, and for each biological replicate, 15 technical replicates (15 non-overlapping confocal field of views from each leaf) were collected. Each field of view was analyzed with custom ImageJ analysis to quantify the GFP fluorescence intensity value for that field of view, and all 15 field of views were then averaged to obtain a mean fluorescence intensity value for that sample. The same protocol was repeated for all 4 biological replicates (4 different plants) per sample, and averaged again for a final fluorescence intensity value, which correlates with the GFP fluorescence intensity of the sample.

Quantitative PCR (qPCR) experiments and data analysis. Two-step qPCR was performed to quantify GFP gene silencing in transgenic mGFP5 *Nicotiana benthamiana* plants with the following commercially-available kits: RNeasy plant mini kit (QIAGEN) for total RNA extraction from leaves, iScript cDNA synthesis kit (Bio-Rad) to reverse transcribe total RNA into cDNA, and PowerUp SYBR green master mix (Applied Biosystems) for qPCR. The target gene in our qPCR was mGFP5 (GFP transgene inserted into *Nicotiana benthamiana*), and EF1 (elongation factor 1) was chosen as the housekeeping (reference) gene. Primers (see detailed sequences in Table 4) for these genes (fGFP, rGFP, fEF1 and rEF1) were ordered from IDT and used without further purification. An annealing temperature of 60˚C was used for qPCR, which was run for 40 cycles. qPCR data was analyzed by the ddCt method to obtain the normalized GFP gene expression-fold change with respect to the EF1 housekeeping gene and control sample. For each sample, qPCR was performed as 3 technical replicates (3 reactions from the same isolated RNA batch), and the entire experiment consisting of independent infiltrations and RNA extractions from different plants was repeated 4 times (4 biological replicates).

Quantitative Western Blot experiments and data analysis. Infiltrated plant leaves were harvested after 72 h and ground in liquid nitrogen to get dry frozen powders. The frozen powders were then transferred to a tube with pre-prepared lysis buffer containing 10 mM Tris/HCl (pH 7.5), 150 mM NaCl, 1 mM EDTA, 0.1% NP-40, 5% glycerol, and 1% cocktail. After lysing at 4˚C overnight, the tube was centrifuged at 10,000 rpm for 20 minutes and the supernatant containing whole proteins was collected to a new tube. After quantification of the total extracted proteins by a Pierce 660 nm Protein Assay (Thermofisher, Prod# 22660), 0.5 µg of normalized total proteins from each sample were analyzed by 12% SDS–PAGE and blotted to a PVDF membrane. The membrane was then blocked for 1 hour using 7.5% BSA in PBST (PBS containing 0.1% Tween20) buffer and rinsed 3 times in PBST buffer, followed by overnight incubation at 4°C with the primary GFP antibody as required (1:2000 dilution, Abcam, ab290). After extensive washing, the corresponding protein bands were probed with a goat anti-rabbit horseradish peroxidase-conjugated antibody (1:5000 dilution, Abcam, ab205718) for 30 min. After 3 washes, the membrane was then developed by incubation with chemiluminescence (Amersham ECL prime kit) plus and imaged by ChemiDoc™ XRS+ System (BIORAD). The intensity of GFP bands were quantified with ImageJ software. To correct for variability in protein expression across different plants and leaves, the GFP extracted from each leaf sample was normalized by the total protein recovered from that leaf tissue.

Quantitative co-localization analysis of Cy3 labeled nanomaterials with GFP. Transgenic mGFP5 *Nicotiana benthamiana* plant leaves were infiltrated with 50 µL Cy3-labeled nanostructures to a final nanostructure concentration of 200 nM and prepared for confocal imaging (12h for DNA materials, and 6h for carbon nanotube related materials) following infiltration. Specifically, one of the single stranded DNA overhangs on the corresponding DNA nanostructure was labeled by Cy3: the H1 strand in HT monomer and nanostring, and one of the four or eight vertices of the tetrahedron. SWCNTs were wrapped with Cy3 labeled GT_{15} ssDNA, and the SWCNT-nanostring hybrid was prepared *via* Cy3 labeling of the nanostring at the nanostring center, which was subsequently conjugated with SWCNT. All three Cy3-labeled structures were infiltrated into mGFP5 *benthamiana* leaves. A small leaf section of the infiltrated leaf tissue was cut and inserted between a glass slide and cover slip of #1 thickness. 20 µL of water was added between the glass slide and cover slip to keep the leaf sections hydrated during imaging. A Zeiss LSM 710 confocal microscope was used to image the plant tissue with two channels: 488 nm laser excitation with a GFP filter cube and 514 nm laser excitation with a Cy3 filter cube. The images were obtained with air-immersion of the objective at 20x magnification. Confocal imaging data were then analyzed to quantify the colocalization fraction between GFP channel and the Cy3 channel across all samples (image J). For each sample, 4 biological replicates (4 infiltrations into 4 different plants) were performed, and for each biological replicate, 15 technical replicates (15 non-overlapping confocal field of views from each leaf) were collected. Each field of view was analyzed with custom ImageJ analysis software to quantify the colocalization percentage value for that field of view, and all 15 field of views were then averaged to obtain a mean value for that sample. The same protocol was repeated for all 4 biological replicates per sample, and averaged again for a final colocalization value, which correlates with the percent colocalization between the Cy3 and GFP channels for each sample.

Protoplast isolation from *Nicotiana benthamiana* leaves. Protoplasts were isolated from *Nicotiana benthamiana* leaves as described by Yoo *et al.*[128] with some modifications. Briefly, thinly cut leaf strips were immersed in 20 mL of enzyme solution (consisting of cellulase and macerozyme), vacuum infiltrated for an hour in the dark using a desiccator, and further incubated at 37˚C for 3 hours in the dark without stirring. Undigested leaf tissue was removed by filtration with a 75 μm nylon mesh, and the flow-through was centrifuged at 200 g for 3 min to pellet the protoplasts in a round bottom tube. Pelleted protoplasts were resuspended in 0.4 M mannitol solution (containing 15 mM $MgCl_2$ and 4 mM MES) with a pH of 5.7, which has similar osmolarity and pH to the protoplasts. Isolated protoplasts can be kept viable on ice for over 24 h; however, we used only freshly isolated protoplasts for all studies.

Nanostructure internalization by protoplasts. 200 μL of the $3\text{x}10^5$ cells/mL protoplast suspension was mixed with 200 nM Cy3-tagged HT monomer nanostructures. The samples were tapped lightly every 15 minutes to encourage mixing and prevent protoplasts from settling at the bottom of the tube. Samples were incubated overnight at room temperature in the dark. The supernatant containing excess free nanostructures was removed without disturbing the protoplast pellet. The protoplasts were immediately resuspended in 200 μL of MMg solution. 200 μL of the protoplast suspension was transferred to a poly-L-lysine coated microwell dish and the protoplasts were allowed to settle at room temperature for 1 hour. Immediately before imaging, protoplasts were stained with 1 μg/mL DAPI for 5 minutes and all images were captured with a fluorescence microscopy using bright-field, Cy3 and DAPI channels.

CHAPTER 5. CONCLUDING REMARKS AND FUTURE DIRECTIONS

Plant synthetic biology and bioengineering has numerous applications in agriculture, as well as the pharmaceutical and energy industries. In agriculture, genetic engineering of plants can be employed to create crops that are resistant to herbicides, insects, diseases, and drought. The ability to introduce transgenes into plant cells also provides the opportunity to improve the nutrient profile of a crop. In the pharmaceutical industry, genetically engineered plants could be used to synthesize valuable small-molecule drugs. Genetically modified plants could also make biofuel production more efficient, which would provide a major benefit for the energy industry and sustainability efforts.

A crucial first step of plant genetic engineering, regardless of the application, is to deliver genetic material and/or proteins into the plant cells and desired subcellular locations inside the cells. Ever since the first transgenic plants were created in the 1980s using the traditional delivery method of *Agrobacterium tumefaciens*, researchers have endeavored to develop and advance new cargo delivery systems for plants, which unfortunately lags behind the developments for animal systems, given the rigid and multilayered cell wall barrier in plant systems. Currently, few delivery tools exist that can transfer biomolecules into plant cells and their subcellular compartments, each with limitations.

Agrobacterium-mediated delivery is the most commonly used tool for gene delivery into plants. However, *Agrobacterium* can only perform gene delivery for a narrow range of plant species, cannot be used for DNA-free editing or for transformation of the chloroplast or mitochondrial genomes, and yields random DNA integration into the plant genome. The other commonly used tool for plant transformation is biolistic particle delivery (also known as gene gun), in which gold microparticles are delivered to plant tissues with a high-pressure gene gun. Biolistics can deliver biomolecules into a wider range of plant species and into plastid genomes but faces limitations of low-level and sporadic expression, random DNA integration, plant tissue damage under high bombardment pressures and exposure to vacuum and requires use of a substantial amount of DNA. Furthermore, gene gun bombardment is a technique that requires specialized facilities and costly materials that limit its widespread use. The lack of versatile, high-throughput tools for biomolecule delivery into plant cells through the rigid and multi-layered cell wall and double lipid bilayer envelopes of organelles represents a significant bottleneck to plant genetic engineering that may be facilitated by nanoparticle technology.

The biomolecule delivery problem in plants is largely due to the presence of the cell wall, which, with a measured size exclusion limit of 5-20 nm, poses the dominant barrier to the delivery of exogenous biomolecules. The plant cell, nuclear, and organelle lipid membranes present a much larger size exclusion limit of approximately 300-500 nm and are additional barriers that must be traversed for genetic transformation of the nuclear or plastid genomes. It is likely that the size similarity of micrometer-sized plant plastids and biolistic gold and MSN microparticles make it difficult to deliver DNA biolistically without destruction of organelles (Fig. 55). Therefore, nanomaterials delivered to plants in a force-independent manner hold great promise to serve as a delivery toolset of key molecular biology cargoes – DNA, RNA, and proteins – to advance genetic engineering of plants and their plastids.

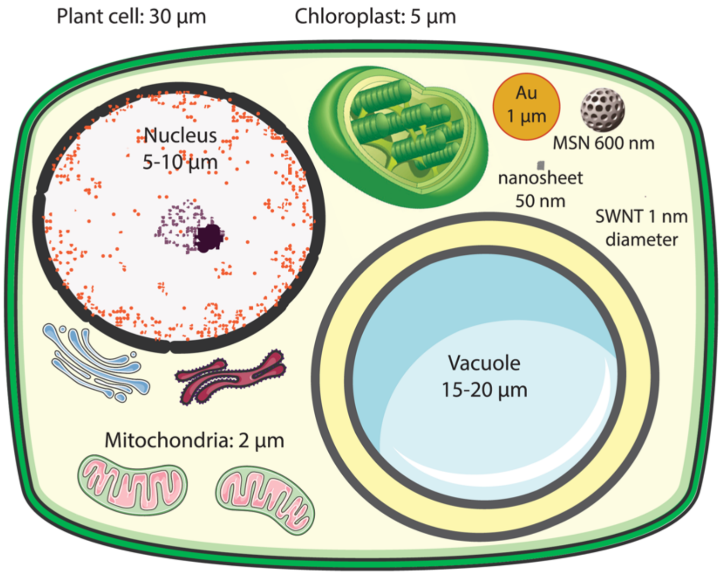

Figure 55. Size of micro- and nanoparticles compared to a plant cell and organelles.

The plant cell nucleus, chloroplast, and mitochondrion are the transformable elements of the cell. Schematics of gold microparticles used for gene gun transformations, and mesoporous silica nanoparticles (MSN), clay nanosheets, and carbon nanotubes (CNT) drawn approximately to scale. The size exclusion limit is ~500 nm for the plant cell and organelle membranes and ~5-20 nm for the plant cell wall.

Nanomaterials are defined as materials with at least one dimension below 100 nm and have unique and tunable physical and chemical properties, which leverage their ability to interact with biological matter with exquisite control and precision. We can classify the nanomaterials used for plant delivery applications under three groups: i) nanomaterials delivered by external aid, ii) nanomaterials delivered *ex planta* (*in vitro)* without external aid, and iii) nanomaterials delivered *in planta* (*in vivo*) without external aid. These nanomaterials are discussed in detail in the introduction section of this dissertation (Chapter 1), with examples of i) gold-capped MSNs, poly-l-lysine coated starch NPs, magnetic gold NPs, DMAEM polymer NPs and magnetic iron oxide NPs, ii) PAMAM dendrimers, calcium phosphate NPs and organically functionalized CNTs, and iii) organically functionalized MSNs, PAMAM dendrimers and polymer functionalized CNTs (Fig. 56).

The usage of nanomaterials for plant delivery applications provided many unique advantages so far. First advantage is the ability to permeate the cell wall and lipid membranes in plant tissues such as leaves, roots, embryo and calli. Second, nanoparticles can also permeate organelle membranes for delivery into nucleus, chloroplast and mitochondria in plant cells, which is not routinely possible with any traditional delivery method. Third, nanoparticles can deliver a diverse set of biological cargoes, such as small molecules, fertilizers, DNA, RNA, proteins and ribonucleoproteins that expand plant genetic engineering applications. Fourth, nanoparticles protect some of these cargoes from nuclease and protease degradation, hence increasing the efficiency of the treatment and decreasing the required dose to achieve high efficiencies. Fifth, nanoparticles can enable targeted delivery and controlled release of cargoes inside the plant cells and organelles. The spatiotemporal control of cargo delivery and release is important for many applications where it is desired to limit the activity of biomolecules to only certain regions at given specific times. Lastly, certain nanoparticles, such as the single-walled carbon nanotubes, are intrinsically fluorescent, which enables the easy imaging and tracking of cargo loaded nanoparticles deep in plant tissues.

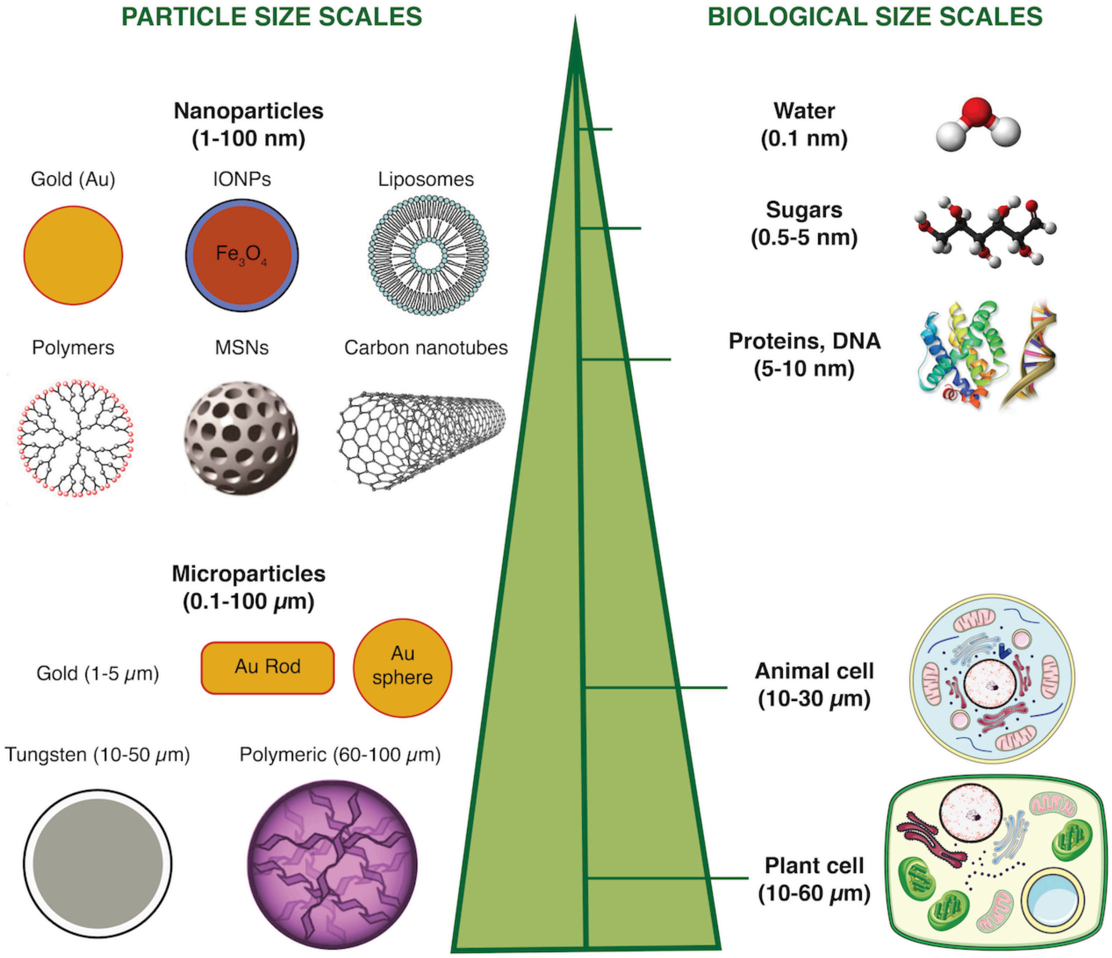

Figure 56. Nano- and microparticles used in plant and animal cargo delivery applications.
Schematic of nanoparticle and microparticle sizes relative to biological matter and plant cells. Nanoparticles have comparable sizes with small molecules in the cells, such as sugars, DNA and proteins, whereas microparticles have comparable sizes with plant and animal organelles and in certain cases they have comparable sizes with the cells themselves, which limit their usage as delivery vehicles.

In this dissertation, I discussed the development and application of carbon nanotubes as emerging method of biomolecule delivery to plants that achieves unprecedented advantages, and that will facilitate plant genetic engineering to reach its full potential. In summary, Chapter 2 details the development, characterization and impact of polymer-functionalized CNTs to deliver and express reporter plasmid DNA in mature and intact plant leaf cells with high efficiency, without transgenic DNA integration and without toxicity. Chapter 3 discusses the usage of pristine single walled carbon nanotubes for the delivery of small interfering RNA for efficient gene knock-down in plants to study plant genotype-phenotype interactions and to boost the transient synthesis of important molecules in plant leaves. Chapter 4 studies the effect of important nanoparticle parameters on plant cell entry and efficient gene silencing using programmable DNA nanostructures with an overarching aim of enabling rational nanoparticle design for plant delivery applications. These studies pave the way for future usage of nanoparticles, specifically carbon nanotubes, for plant transient expression/silencing applications as well as plant genetic engineering applications using next-generation nuclease-based gene editing technologies, such as the previously discussed CRISPR/Cas.

Genetic engineering of plants has greatly accelerated scientific progress and paved the way for crop variants with improved growth characteristics, disease and pest resistance, environmental stress tolerance, and enhanced nutritional value. In parallel, advances in site-specific genome editing technologies have optimized the precision with which genetic engineering of organisms can be accomplished. However, conventional methods of plant genetic engineering and genome editing are limited in scope. This is primarily due to the cell wall that imposes a barrier to efficient delivery of biomolecules, which could potentially be overcome by nanoparticles. *Agrobacterium* is a preferred method for plant genetic transformation but is only effective in a limited range of host species and is an automatic trigger for regulatory oversight in the United States. Biolistic particle delivery and PEG-transfection are effective, host-independent transformation methods, but difficulties in regenerating healthy plant tissue and low-efficiency editing are severe drawbacks to their broad-scale and high-throughput implementation. NPs have recently emerged as a novel method of targeted biomolecule delivery in mammalian cells, especially for clinical applications. However, exploration of nanocarriers for biomolecule delivery in plants remains a nascent field, with much potential for the future of plant biotechnology and genome editing. To my knowledge, the field of plant bioengineering has yet to fully demonstrate a reliable strategy for nanoparticle-mediated passive biomolecule delivery to plants.

Our preliminary studies show that nanoparticles with proper surface chemistry and physical properties analogous to those developed for animal systems are capable of delivering biomolecules to plants *in vivo* and *in vitro* with improvements over conventional methods. To realize the full scientific and humanitarian potential in genetic engineering of both model and crop species, especially with the advent of nuclease-based genome editing, a promising focus will be to optimize nanoparticles as efficient and ubiquitous delivery vessels of diverse biomolecules, tunable across cargo types, species, and tissues, for both transient and stable genetic engineering. However, because germline transformation is currently limited to only one model plant species (*Arabidopsis*), even a ubiquitous delivery strategy for precise genome editing would be limited by the success of regenerating progeny from somatic tissue. A remarkable, yet conceivable, future accomplishment of nanoparticle delivery in plants could be enablement of unprecedented, highly parallel genetic studies that elucidate the precedents for success in tissue regeneration, and the direct manipulation of germline plant cells.

Several future directions of this project are to:

1. Deliver biomolecular cargoes that will enable genome editing, such as CRISPR/Cas9 plasmids encoding for the Cas9 protein and the guide RNA sequence, or Cas9 ribonucleoproteins to show the efficacy of carbon nanotube-mediated gene editing in plant systems. For this purpose, plant genes that will give resistance to diseases or climate changes can be initially targeted.
2. Extend the usage of carbon nanotube-mediated delivery to additional tissues that will enable the creation of gene edited and improved plants. Initially, tissues that will remove the need for plant regeneration in tissue culture should be targeted, such as the plant reproductive organs (*i.e.* flowers and pollen). If not successful, next plant shoot apical meristems or calli may be targeted. Another approach to obtain gene edited plants and also eliminate certain steps of the regeneration is to use the recent technology of somatic embryogenesis by transiently expressing the morphogenic regulators and CRISPR parts in plant somatic tissues using the developed carbon nanotube platform.
3. Use the carbon nanotube delivery platforms in non-model plants, in which the plant transformation is highly challenged and/or impossible with current methods. These plants include certain grass species, sorghum, cassava, yams, legumes, banana, grapes, among many others. Usage of carbon nanotubes will especially be impactful in vegetatively-propagated plants, as the DNA integration-free nanoparticle platform removes the need of transgene segregation for edited crops to reach the markets, which is not possible for vegetatively-propagated plants.

Several outstanding questions in the field of nanoparticle-mediated plant genetic engineering are:

1. Are there nanoparticle varieties yet to be discovered for efficient biomolecule delivery in plants, or do we lack knowledge of, or control over, optimal nanoparticle modifications for applications in plant systems?
2. Can we narrow the current design space to a single nanoparticle type with tunable functionalization for passive delivery in plants, regardless of cargo type, plant species, and tissue variety?
3. How might we gain a better mechanistic understanding of nanoparticle internalization into plant cells, and how can we harness this knowledge towards rational design of nanoparticles for a range of biological delivery applications?
4. Will challenges in biomolecule delivery and progeny regeneration always remain decoupled, or will nanoparticle delivery enable significant increase in throughput and efficiency of genetic studies on plant regenerative biology and stable transformation?
5. While genome editing by induced nonhomologous end-joining does not invoke regulatory oversight in many countries, how will genome edits introduced by homology-directed repair (where integration of a repair template is necessary) be classified from a legislative standpoint?
6. How can scientists, the public, and regulatory bodies create a space for open communication to address the risks of introducing crop variants to the environment, while continuing to enable scientific progress and commercialization of sustainable and resilient crop variants?

In conclusion, nanoparticles have shown immense improvement and potential so far for enabling the next-generation of plant genetic engineering that can provide food security for a growing global population under changing climate, and that can facilitate our global sustainability efforts, once the outstanding questions and challenges are tackled by plant scientists and engineers.

REFERENCES

1 Summit, W. F. Rome declaration on world food security and world food summit plan of action. Italy: FAO (1996).

2 Khush, G. S. IR varieties and their impact. (Int. Rice Res. Inst., 2005).

3 Sasaki, A. et al. A mutant gibberellin-synthesis gene in rice. Nature 416, 701-702 (2002).

4 Kim, B. et al. Defining the genome structure of Tongil rice, an important cultivar in the Korean"Green Revolution". Rice 7, 1-9 (2014).

5 Shi, J. et al. ARGOS 8 variants generated by CRISPR-Cas9 improve maize grain yield under field drought stress conditions. Plant biotechnology journal 15, 207-216 (2017).

6 Dong, O. X. et al. Marker-free carotenoid-enriched rice generated through targeted gene insertion using CRISPR-Cas9. Nature Communications 11, 1-10 (2020).

7 Sun, Y. et al. Engineering herbicide-resistant rice plants through CRISPR/Cas9-mediated homologous recombination of acetolactate synthase. Molecular plant 9, 628-631 (2016).

8 Wang, F. et al. Enhanced rice blast resistance by CRISPR/Cas9-targeted mutagenesis of the ERF transcription factor gene OsERF922. PloS one 11 (2016).

9 Arora, L. & Narula, A. Gene editing and crop improvement using CRISPR-Cas9 system. Frontiers in plant science 8, 1932 (2017).

10 Saha, D. et al. Genomic insights into HSFs as candidate genes for high-temperature stress adaptation and gene editing with minimal off-target effects in flax. Scientific reports 9, 1-18 (2019).

11 Iqbal, M. N. & Ashraf, A. Recombinant Protein Production in Plants: Biofactories for Therapeutics. International Journal of Molecular Microbiology 1, 38-39 (2018).

12 Rozov, S. & Deineko, E. Strategies for optimizing recombinant protein synthesis in plant cells: classical approaches and new directions. Molecular Biology 53, 157-175 (2019).

13 Yau, Y.-Y. & Easterling, M. in Biofuels: Greenhouse Gas Mitigation and Global Warming. 107-140 (Springer, 2018).

14 Kim, Y.-G., Cha, J. & Chandrasegaran, S. Hybrid restriction enzymes: zinc finger fusions to Fok I cleavage domain. Proceedings of the National Academy of Sciences 93, 1156-1160 (1996).

15 Jinek, M. et al. A programmable dual-RNA–guided DNA endonuclease in adaptive bacterial immunity. science 337, 816-821 (2012).

16 Boch, J. et al. Breaking the code of DNA binding specificity of TAL-type III effectors. Science 326, 1509-1512 (2009).

17 Azencott, H. R., Peter, G. F. & Prausnitz, M. R. Influence of the cell wall on intracellular delivery to algal cells by electroporation and sonication. Ultrasound in medicine & biology 33, 1805-1817 (2007).

18 Bevan, M. Binary Agrobacterium vectors for plant transformation. Nucleic Acids Res 12, 8711-8721 (1984).

19 Klein, T. M., Wolf, E., Wu, R. & Sanford, J. High-velocity microprojectiles for delivering nucleic acids into living cells. Nature 327, 70-73 (1987).

20 Woo, J. W. et al. DNA-free genome editing in plants with preassembled CRISPR-Cas9 ribonucleoproteins. Nat Biotechnol 33, 1162-1164 (2015).

21 Svitashev, S., Schwartz, C., Lenderts, B., Young, J. K. & Cigan, A. M. Genome editing in maize directed by CRISPR–Cas9 ribonucleoprotein complexes. Nature communications 7, 1-7 (2016).

22 Li, J.-F. et al. Multiplex and homologous recombination–mediated genome editing in Arabidopsis and Nicotiana benthamiana using guide RNA and Cas9. Nat Biotechnol 31, 688-691 (2013).

23 Ali, Z. et al. Efficient virus-mediated genome editing in plants using the CRISPR/Cas9 system. Molecular plant 8, 1288-1291 (2015).

24 Thorat, A. S., Sonone, N. A., Choudhari, V. V., Devarumath, R. M. & Babu, K. H. Plant regeneration from cell suspension culture in Saccharum officinarum L. and ascertaining of genetic fidelity through RAPD and ISSR markers. 3 Biotech 7, 16 (2017).

25 Nyaboga, E., Tripathi, J. N., Manoharan, R. & Tripathi, L. Agrobacterium-mediated genetic transformation of yam (Dioscorea rotundata): an important tool for functional study of genes and crop improvement. Frontiers in plant science 5, 463 (2014).

26 Gelvin, S. B. Integration of Agrobacterium T-DNA into the plant genome. Annual review of genetics 51, 195-217 (2017).

27 Gleba, Y., Klimyuk, V. & Marillonnet, S. Magnifection—a new platform for expressing recombinant vaccines in plants. Vaccine 23, 2042-2048 (2005).

28 Stoddard, T., Baltes, N. J. & Luo, S. (Google Patents, 2016).

29 Vijayaraghavan, K. & Ashokkumar, T. Plant-mediated biosynthesis of metallic nanoparticles: a review of literature, factors affecting synthesis, characterization techniques and applications. Journal of environmental chemical engineering 5, 4866-4883 (2017).

30 Baker, S., Volova, T., Prudnikova, S. V., Satish, S. & Prasad, N. Nanoagroparticles emerging trends and future prospect in modern agriculture system. Environmental toxicology and pharmacology 53, 10-17 (2017).

31 Zuverza-Mena, N. et al. Exposure of engineered nanomaterials to plants: Insights into the physiological and biochemical responses-A review. Plant Physiology and Biochemistry 110, 236-264 (2017).
32 Tripathi, D. K. et al. An overview on manufactured nanoparticles in plants: uptake, translocation, accumulation and phytotoxicity. Plant Physiology and Biochemistry 110, 2-12 (2017).
33 Hussain, H. I., Yi, Z., Rookes, J. E., Kong, L. X. & Cahill, D. M. Mesoporous silica nanoparticles as a biomolecule delivery vehicle in plants. Journal of Nanoparticle Research 15, 1676, doi:10.1007/s11051-013-1676-4 (2013).
34 Liu, Q. et al. Carbon nanotubes as molecular transporters for walled plant cells. Nano letters 9, 1007-1010 (2009).
35 Koo, Y. et al. Fluorescence reports intact quantum dot uptake into roots and translocation to leaves of Arabidopsis thaliana and subsequent ingestion by insect herbivores. Environmental science & technology 49, 626-632 (2015).
36 Kurepa, J. et al. Uptake and distribution of ultrasmall anatase TiO2 Alizarin red S nanoconjugates in Arabidopsis thaliana. Nano letters 10, 2296-2302 (2010).
37 Naqvi, S. et al. Calcium phosphate nanoparticle mediated genetic transformation in plants. Journal of Materials Chemistry 22, 3500-3507 (2012).
38 Antonelli, N. & Stadler, J. Genomic DNA can be used with cationic methods for highly efficient transformation of maize protoplasts. Theoretical and applied genetics 80, 395-401 (1990).
39 Ragelle, H. et al. Chitosan nanoparticles for siRNA delivery: optimizing formulation to increase stability and efficiency. Journal of Controlled Release 176, 54-63 (2014).
40 Zuris, J. A. et al. Cationic lipid-mediated delivery of proteins enables efficient protein-based genome editing in vitro and in vivo. Nat Biotechnol 33, 73 (2015).
41 Pantarotto, D. et al. Functionalized carbon nanotubes for plasmid DNA gene delivery. Angewandte Chemie International Edition 43, 5242-5246 (2004).
42 Demirer, G. S. et al. High aspect ratio nanomaterials enable delivery of functional genetic material without DNA integration in mature plants. Nature Nanotechnology, doi:10.1038/s41565-019-0382-5 (2019).
43 Kam, N. W. S., Liu, Z. & Dai, H. Functionalization of carbon nanotubes via cleavable disulfide bonds for efficient intracellular delivery of siRNA and potent gene silencing. Journal of the American Chemical Society 127, 12492-12493 (2005).
44 Kneuer, C. et al. A nonviral DNA delivery system based on surface modified silica-nanoparticles can efficiently transfect cells in vitro. Bioconjugate Chemistry 11, 926-932 (2000).

45 Torney, F., Trewyn, B. G., Lin, V. S.-Y. & Wang, K. Mesoporous silica nanoparticles deliver DNA and chemicals into plants. Nature nanotechnology 2, 295-300 (2007).

46 Chen, A. M. et al. Co-delivery of doxorubicin and Bcl-2 siRNA by mesoporous silica nanoparticles enhances the efficacy of chemotherapy in multidrug-resistant cancer cells. Small 5, 2673-2677 (2009).

47 Martin-Ortigosa, S. et al. Mesoporous silica nanoparticle-mediated intracellular Cre protein delivery for maize genome editing via loxP site excision. Plant physiology 164, 537-547 (2014).

48 Boussif, O. et al. A versatile vector for gene and oligonucleotide transfer into cells in culture and in vivo: polyethylenimine. Proceedings of the National Academy of Sciences 92, 7297-7301 (1995).

49 Negrutiu, I., Shillito, R., Potrykus, I., Biasini, G. & Sala, F. Hybrid genes in the analysis of transformation conditions. Plant Molecular Biology 8, 363-373 (1987).

50 Aigner, A. et al. Delivery of unmodified bioactive ribozymes by an RNA-stabilizing polyethylenimine (LMW-PEI) efficiently down-regulates gene expression. Gene therapy 9, 1700-1707 (2002).

51 Silva, A. T., Nguyen, A., Ye, C., Verchot, J. & Moon, J. H. Conjugated polymer nanoparticles for effective siRNA delivery to tobacco BY-2 protoplasts. BMC Plant Biology 10, 291, doi:10.1186/1471-2229-10-291 (2010).

52 Sgolastra, F. et al. Sequence segregation improves non-covalent protein delivery. Journal of Controlled Release 254, 131-136 (2017).

53 Mizutani, O., Masaki, K., Gomi, K. & Iefuji, H. Modified Cre-loxP recombination in Aspergillus oryzae by direct introduction of Cre recombinase for marker gene rescue. Appl. Environ. Microbiol. 78, 4126-4133 (2012).

54 Sun, W. et al. Self-Assembled DNA Nanoclews for the Efficient Delivery of CRISPR–Cas9 for Genome Editing. Angewandte Chemie International Edition 54, 12029-12033, doi:doi:10.1002/anie.201506030 (2015).

55 Sandhu, K. K., McIntosh, C. M., Simard, J. M., Smith, S. W. & Rotello, V. M. Gold nanoparticle-mediated transfection of mammalian cells. Bioconjugate chemistry 13, 3-6 (2002).

56 Zhao, X. et al. Pollen magnetofection for genetic modification with magnetic nanoparticles as gene carriers. Nature plants 3, 956-964 (2017).

57 Lee, J. H. et al. All-in-one target-cell-specific magnetic nanoparticles for simultaneous molecular imaging and siRNA delivery. Angewandte Chemie International Edition 48, 4174-4179 (2009).

58 Mout, R. et al. General strategy for direct cytosolic protein delivery via protein–nanoparticle co-engineering. ACS nano 11, 6416-6421 (2017).

59 Lee, K. et al. Nanoparticle delivery of Cas9 ribonucleoprotein and donor DNA in vivo induces homology-directed DNA repair. Nature Biomedical Engineering 1, 889-901, doi:10.1038/s41551-017-0137-2 (2017).

60 Wang, P., Lombi, E., Zhao, F.-J. & Kopittke, P. M. Nanotechnology: a new opportunity in plant sciences. Trends in plant science 21, 699-712 (2016).

61 Schwab, F. et al. Barriers, pathways and processes for uptake, translocation and accumulation of nanomaterials in plants–Critical review. Nanotoxicology 10, 257-278 (2016).

62 Fan, L., Li, R., Pan, J., Ding, Z. & Lin, J. Endocytosis and its regulation in plants. Trends in Plant Science 20, 388-397 (2015).

63 Albanese, A., Tang, P. S. & Chan, W. C. The effect of nanoparticle size, shape, and surface chemistry on biological systems. Annual review of biomedical engineering 14, 1-16 (2012).

64 Zhu, Z.-J. et al. Effect of surface charge on the uptake and distribution of gold nanoparticles in four plant species. Environmental science & technology 46, 12391-12398 (2012).

65 Gratton, S. E. et al. The effect of particle design on cellular internalization pathways. Proceedings of the National Academy of Sciences 105, 11613-11618 (2008).

66 Serag, M. F., Kaji, N., Habuchi, S., Bianco, A. & Baba, Y. Nanobiotechnology meets plant cell biology: carbon nanotubes as organelle targeting nanocarriers. Rsc Adv 3, 4856-4862 (2013).

67 Serag, M. F. et al. Trafficking and subcellular localization of multiwalled carbon nanotubes in plant cells. ACS nano 5, 493-499 (2011).

68 Caracciolo, G., Farokhzad, O. C. & Mahmoudi, M. Biological identity of nanoparticles in vivo: clinical implications of the protein corona. Trends in biotechnology 35, 257-264 (2017).

69 Selby, L. I., Cortez-Jugo, C. M., Such, G. K. & Johnston, A. P. Nanoescapology: progress toward understanding the endosomal escape of polymeric nanoparticles. Wiley Interdisciplinary Reviews: Nanomedicine and Nanobiotechnology 9, e1452 (2017).

70 Chang, F.-P. et al. A simple plant gene delivery system using mesoporous silica nanoparticles as carriers. Journal of Materials Chemistry B 1, 5279-5287, doi:10.1039/C3TB20529K (2013).

71 Lallana, E., Sousa-Herves, A., Fernandez-Trillo, F., Riguera, R. & Fernandez-Megia, E. Click chemistry for drug delivery nanosystems. Pharmaceutical research 29, 1-34 (2012).

72 Slowing, I. I., Vivero-Escoto, J. L., Wu, C.-W. & Lin, V. S.-Y. Mesoporous silica nanoparticles as controlled release drug delivery and gene transfection carriers. Advanced drug delivery reviews 60, 1278-1288 (2008).

73 Liu, J. et al. Preparation of fluorescence starch-nanoparticle and its application as plant transgenic vehicle. Journal of Central South University of Technology 15, 768-773, doi:10.1007/s11771-008-0142-4 (2008).

74 Hao, Y. et al. Magnetic gold nanoparticles as a vehicle for fluorescein isothiocyanate and DNA delivery into plant cells. Botany 91, 457-466 (2013).

75 Finiuk, N. et al. Investigation of novel oligoelectrolyte polymer carriers for their capacity of DNA delivery into plant cells. Plant Cell, Tissue and Organ Culture (PCTOC) 131, 27-39 (2017).

76 Pasupathy, K., Lin, S., Hu, Q., Luo, H. & Ke, P. C. Direct plant gene delivery with a poly (amidoamine) dendrimer. Biotechnology Journal: Healthcare Nutrition Technology 3, 1078-1082 (2008).

77 Burlaka, O., Pirko, Y. V., Yemets, A. & Blume, Y. B. Plant genetic transformation using carbon nanotubes for DNA delivery. Cytology and genetics 49, 349-357 (2015).

78 Jiang, L. et al. Systemic gene silencing in plants triggered by fluorescent nanoparticle-delivered double-stranded RNA. Nanoscale 6, 9965-9969 (2014).

79 Birnbaum, K. D. & Alvarado, A. S. Slicing across kingdoms: regeneration in plants and animals. Cell 132, 697-710 (2008).

80 Bortesi, L. & Fischer, R. The CRISPR/Cas9 system for plant genome editing and beyond. Biotechnol Adv 33, 41-52 (2015).

81 Feng, Z. et al. Multigeneration analysis reveals the inheritance, specificity, and patterns of CRISPR/Cas-induced gene modifications in Arabidopsis. Proceedings of the National Academy of Sciences 111, 4632-4637 (2014).

82 Jiang, W., Yang, B. & Weeks, D. P. Efficient CRISPR/Cas9-mediated gene editing in Arabidopsis thaliana and inheritance of modified genes in the T2 and T3 generations. PloS one 9 (2014).

83 Briefs, I. (2017).

84 Camacho, A., Van Deynze, A., Chi-Ham, C. & Bennett, A. B. Genetically engineered crops that fly under the US regulatory radar. Nat Biotechnol 32, 1087-1091 (2014).

85 EU-Commission. Directive 2001/18/EC of the European Parliament and of the Council of 12 March 2001 on the deliberate release into the environment of genetically modified organisms and repealing Council Directive 90/220. EEC (2001).

86 Waltz, E. Nature Publishing Group (2018).

87 Liu, C., Zhang, L., Liu, H. & Cheng, K. Delivery strategies of the CRISPR-Cas9 gene-editing system for therapeutic applications. Journal of controlled release 266, 17-26 (2017).

88 Daniell, H., Datta, R., Varma, S., Gray, S. & Lee, S.-B. Containment of herbicide resistance through genetic engineering of the chloroplast genome. Nat Biotech 16, 345-348 (1998).

89 Liu, Y. et al. A gene cluster encoding lectin receptor kinases confers broad-spectrum and durable insect resistance in rice. Nat Biotech 33, 301-305, doi:10.1038/nbt.3069 (2015).

90 Li, T., Liu, B., Spalding, M. H., Weeks, D. P. & Yang, B. High-efficiency TALEN-based gene editing produces disease-resistant rice. Nat Biotech 30, 390-392, doi:10.1038/nbt.2199 (2012).

91 Zhang, G. et al. Overexpression of the soybean GmERF3 gene, an AP2/ERF type transcription factor for increased tolerances to salt, drought, and diseases in transgenic tobacco. Journal of Experimental Botany 60, 3781-3796, doi:10.1093/jxb/erp214 (2009).

92 Chen, Q. & Lai, H. Gene delivery into plant cells for recombinant protein production. Biomed Res Int 2015, 932161, doi:10.1155/2015/932161 (2015).

93 Himmel, M. E. et al. Biomass Recalcitrance: Engineering Plants and Enzymes for Biofuels Production. Science 315, 804 (2007).

94 Tufekcioglu, A., Raich, J., Isenhart, T. & Schultz, R. Biomass, carbon and nitrogen dynamics of multi-species riparian buffers within an agricultural watershed in Iowa, USA. Agroforestry Systems 57, 187-198 (2003).

95 Altpeter, F. et al. Advancing crop transformation in the era of genome editing. The Plant Cell 28, 1510-1520 (2016).

96 Herrera-Estrella, L., Depicker, A., Van Montagu, M. & Schell, J. Expression of chimaeric genes transferred into plant cells using a Ti-plasmid-derived vector. Nature 303, 209-213 (1983).

97 Baltes, N. J., Gil-Humanes, J. & Voytas, D. F. Genome Engineering and Agriculture: Opportunities and Challenges. Progress in Molecular Biology and Translational Science (2017).

98 Caranta, C. Recent advances in plant virology. (Horizon Scientific Press, 2011).

99 Gleba, Y., Klimyuk, V. & Marillonnet, S. Viral vectors for the expression of proteins in plants. Current opinion in biotechnology 18, 134-141 (2007).

100 Song, S., Hao, Y., Yang, X., Patra, P. & Chen, J. Using gold nanoparticles as delivery vehicles for targeted delivery of chemotherapy drug fludarabine phosphate to treat hematological cancers. Journal of nanoscience and nanotechnology 16, 2582-2586 (2016).

101 Mizrachi, A. et al. Tumour-specific PI3K inhibition via nanoparticle-targeted delivery in head and neck squamous cell carcinoma. Nature Communications 8, 14292 (2017).

102 Demirer, G. S. & Landry, M. P. Delivering Genes to Plants. CHEMICAL ENGINEERING PROGRESS 113, 40-45 (2017).

103 Martin-Ortigosa, S. et al. Parameters Affecting the Efficient Delivery of Mesoporous Silica Nanoparticle Materials and Gold Nanorods into Plant Tissues by the Biolistic Method. Small 8, 413-422, doi:doi:10.1002/smll.201101294 (2012).

104 Zhang, H. et al. DNA nanostructures coordinate gene silencing in mature plants. Proceedings of the National Academy of Sciences 116, 7543-7548 (2019).

105 Asad, S. & Arshad, M. in Properties and Applications of Silicon Carbide (InTech, 2011).

106 Mitter, N. et al. Clay nanosheets for topical delivery of RNAi for sustained protection against plant viruses. Nature Plants 3, 16207, doi:10.1038/nplants.2016.207 (2017).

107 Wong, M. H. et al. Lipid exchange envelope penetration (LEEP) of nanoparticles for plant engineering: A universal localization mechanism. Nano letters 16, 1161-1172 (2016).

108 Giraldo, J. P. et al. Plant nanobionics approach to augment photosynthesis and biochemical sensing. Nature materials 13, 400-408 (2014).

109 Wu, Y., Phillips, J. A., Liu, H., Yang, R. & Tan, W. Carbon nanotubes protect DNA strands during cellular delivery. ACS nano 2, 2023-2028 (2008).

110 Zheng, M. et al. DNA-assisted dispersion and separation of carbon nanotubes. Nature materials 2, 338 (2003).

111 Wang, H. et al. High-yield sorting of small-diameter carbon nanotubes for solar cells and transistors. ACS nano 8, 2609-2617 (2014).

112 Serag, M. F. et al. Trafficking and subcellular localization of multiwalled carbon nanotubes in plant cells. ACS nano 5, 493-499 (2010).

113 Wong, M. H. et al. Nitroaromatic detection and infrared communication from wild-type plants using plant nanobionics. Nature materials 16, 264-272 (2017).

114 Choi, J. H. & Strano, M. S. Solvatochromism in single-walled carbon nanotubes. Applied Physics Letters 90, 223114 (2007).

115 Tinland, B. The integration of T-DNA into plant genomes. Trends in Plant Science 1, 178-184, doi:https://doi.org/10.1016/1360-1385(96)10020-0 (1996).

116 Collier, R. et al. Accurate measurement of transgene copy number in crop plants using droplet digital PCR. The Plant Journal 90, 1014-1025 (2017).

117 Yoshioka, H. et al. Nicotiana benthamiana gp91phox homologs NbrbohA and NbrbohB participate in H2O2 accumulation and resistance to Phytophthora infestans. The Plant Cell 15, 706-718 (2003).

118 Hicks, K. O., Fleming, Y., Siim, B. G., Koch, C. J. & Wilson, W. R. Extravascular diffusion of tirapazamine: effect of metabolic consumption assessed using the multicellular layer model. International Journal of Radiation Oncology* Biology* Physics 42, 641-649 (1998).

119 Wei, C., Srivastava, D. & Cho, K. Thermal expansion and diffusion coefficients of carbon nanotube-polymer composites. Nano Letters 2, 647-650 (2002).

120 Lew, T. T. S. et al. Rational Design Principles for the Transport and Subcellular Distribution of Nanomaterials into Plant Protoplasts. Small, 1802086 (2018).

121 Schaumberg, K. A. et al. Quantitative characterization of genetic parts and circuits for plant synthetic biology. Nature methods 13, 94 (2016).

122 Alidori, S. et al. Deploying RNA and DNA with functionalized carbon nanotubes. The Journal of Physical Chemistry C 117, 5982-5992 (2013).

123 Volkov, A. & Coppens, P. Calculation of electrostatic interaction energies in molecular dimers from atomic multipole moments obtained by different methods of electron density partitioning. Journal of computational chemistry 25, 921-934 (2004).

124 Sullivan, A. M. et al. Mapping and dynamics of regulatory DNA and transcription factor networks in A. thaliana. Cell reports 8, 2015-2030 (2014).

125 Lau, W. & Sattely, E. S. Six enzymes from mayapple that complete the biosynthetic pathway to the etoposide aglycone. Science 349, 1224-1228 (2015).

126 Cunningham, F. J., Goh, N. S., Demirer, G. S., Matos, J. L. & Landry, M. P. Nanoparticle-Mediated Delivery towards Advancing Plant Genetic Engineering. Trends in Biotechnology, doi:https://doi.org/10.1016/j.tibtech.2018.03.009 (2018).

127 Del Bonis-O'Donnell, J. T. et al. Engineering Molecular Recognition with Bio-mimetic Polymers on Single Walled Carbon Nanotubes. JoVE (Journal of Visualized Experiments), e55030 (2017).

128 Yoo, S.-D., Cho, Y.-H. & Sheen, J. Arabidopsis mesophyll protoplasts: a versatile cell system for transient gene expression analysis. Nature protocols 2, 1565 (2007).

129 Yang, M., Gao, Y., Li, H. & Adronov, A. Functionalization of multiwalled carbon nanotubes with polyamide 6 by anionic ring-opening polymerization. Carbon 45, 2327-2333 (2007).

130 Beyene, A. G., Demirer, G. S. & Landry, M. P. Nanoparticle-Templated Molecular Recognition Platforms for Detection of Biological Analytes. Current protocols in chemical biology, 197-223 (2016).

131 Ma, L. et al. Enhanced Li–S batteries using amine-functionalized carbon nanotubes in the cathode. ACS nano 10, 1050-1059 (2015).

132 Schmittgen, T. D. & Livak, K. J. Analyzing real-time PCR data by the comparative CT method. Nature protocols 3, 1101 (2008).

133 Casacuberta, J. M. et al. Biotechnological uses of RNAi in plants: risk assessment considerations. Trends in Biotechnology 33, 145-147, doi:https://doi.org/10.1016/j.tibtech.2014.12.003 (2015).

134 Dhaka, N. & Sharma, R. MicroRNAs as targets for engineering biofuel feedstock Sorghum. Indian Journal of Plant Physiology 22, 484-492 (2017).

135 Sukenik, S. C. et al. Transient Recombinant Protein Production in Glycoengineered Nicotiana benthamiana Cell Suspension Culture. International journal of molecular sciences 19, 1205 (2018).

136 Small, I. RNAi for revealing and engineering plant gene functions. Current Opinion in Biotechnology 18, 148-153, doi: https://doi.org/10.1016/j.copbio.2007.01.012 (2007).

137 Duan, C.-G., Wang, C.-H. & Guo, H.-S. Application of RNA silencing to plant disease resistance. Silence 3, 5 (2012).

138 Burch-Smith, T. M., Anderson, J. C., Martin, G. B. & Dinesh-Kumar, S. P. Applications and advantages of virus-induced gene silencing for gene function studies in plants. The Plant Journal 39, 734-746, doi:10.1111/j.1365-313X.2004.02158.x (2004).

139 Anand, A. & Jones, T. J. in Agrobacterium Biology: From Basic Science to Biotechnology (ed Stanton B. Gelvin) 489-507 (Springer International Publishing, 2018).

140 Tang, W. et al. Post-transcriptional gene silencing induced by short interfering RNAs in cultured transgenic plant cells. Genomics, proteomics & bioinformatics 2, 97-108 (2004).

141 Johnson, R. R., Johnson, A. C. & Klein, M. L. Probing the structure of DNA−carbon nanotube hybrids with molecular dynamics. Nano letters 8, 69-75 (2008).

142 Das, A. et al. Binding of nucleobases with single-walled carbon nanotubes: Theory and experiment. Chemical Physics Letters 453, 266-273 (2008).

143 Salvador-Morales, C. et al. Complement activation and protein adsorption by carbon nanotubes. Molecular immunology 43, 193-201 (2006).

144 Pinals, R. L., Yang, D., Lui, A., Cao, W. & Landry, M. P. Corona exchange dynamics on carbon nanotubes by multiplexed fluorescence monitoring. Journal of the American Chemical Society (2019).

145 Shen, J.-W., Wu, T., Wang, Q. & Kang, Y. Induced stepwise conformational change of human serum albumin on carbon nanotube surfaces. Biomaterials 29, 3847-3855 (2008).

146 Yang, Z., Wang, Z., Tian, X., Xiu, P. & Zhou, R. Amino acid analogues bind to carbon nanotube via π-π interactions: comparison of molecular mechanical and quantum mechanical calculations. The Journal of chemical physics 136, 01B607 (2012).

147 Beyene, A. G. et al. Ultralarge modulation of fluorescence by neuromodulators in carbon nanotubes functionalized with self-assembled oligonucleotide rings. Nano letters 18, 6995-7003 (2018).

148 Kuriyan, J., Konforti, B. & Wemmer, D. The molecules of life: Physical and chemical principles. (Garland Science, 2012).

149 Lu, N. et al. Adsorption of human serum albumin on functionalized single-walled carbon nanotubes reduced cytotoxicity. Chemico-biological interactions 295, 64-72 (2018).

150 Brocchieri, L. & Karlin, S. Protein length in eukaryotic and prokaryotic proteomes. Nucleic Acids Res 33, 3390-3400 (2005).

151 Schultink, A., Qi, T., Lee, A., Steinbrenner, A. D. & Staskawicz, B. J. T. P. J. Roq1 mediates recognition of the Xanthomonas and Pseudomonas effector proteins XopQ and HopQ1. 92, 787-795 (2017).

152 Yuan, H. et al. Single walled carbon nanotubes exhibit dual-phase regulation to exposed Arabidopsis mesophyll cells. Nanoscale Res Lett 6, 44 (2011).

153 Goodman, C. M., McCusker, C. D., Yilmaz, T. & Rotello, V. M. Toxicity of Gold Nanoparticles Functionalized with Cationic and Anionic Side Chains. Bioconjugate Chemistry 15, 897-900, doi:10.1021/bc049951i (2004).

154 Qi, Y. et al. Increasing frequencies of site-specific mutagenesis and gene targeting in Arabidopsis by manipulating DNA repair pathways. Genome research, gr. 145557.145112 (2013).

155 Kruss, S. et al. Neurotransmitter detection using corona phase molecular recognition on fluorescent single-walled carbon nanotube sensors. Journal of the American Chemical Society 136, 713-724 (2014).

156 Binns, A. N. Agrobacterium-mediated gene delivery and the biology of hostrange limitations. Physiologia Plantarum 79, 135-139 (1990).

157 Altpeter, F. et al. Advancing crop transformation in the era of genome editing. The Plant Cell, 1510-1520 (2016).

158 Demirer, G. S. et al. High Aspect Ratio Nanomaterials Enable Biomolecule Delivery and Transgene Expression or Silencing in Mature Plants. bioRxiv, doi:10.1101/179549 (2018).

159 Watson, J. D. & Crick, F. H. Molecular structure of nucleic acids; a structure for deoxyribose nucleic acid. Nature 171, 737-738 (1953).

160 Stefano, G., Renna, L. & Brandizzi, F. Plant Cell Vacuoles: Staining and Fluorescent Probes. Methods Mol Biol 1789, 55-63, doi:10.1007/978-1-4939-7856-4_5 (2018).

161 Horn, M. A., Heinstein, P. F. & Low, P. S. Receptor-Mediated Endocytosis in Plant-Cells. Plant Cell 1, 1003-1009 (1989).

162 Bastings, M. M. C. et al. Modulation of the Cellular Uptake of DNA Origami through Control over Mass and Shape. Nano Letters 18, 3557-3564, doi:10.1021/acs.nanolett.8b00660 (2018).

163 Pan, K., Bricker, W. P., Ratanalert, S. & Bathe, M. Structure and conformational dynamics of scaffolded DNA origami nanoparticles. Nucleic Acids Res 45, 6284-6298 (2017).

164 Pfitzner, E. et al. Rigid DNA beams for high-resolution single-molecule mechanics. Angewandte Chemie International Edition 52, 7766-7771 (2013).

165 Smith, S. B., Cui, Y. J. & Bustamante, C. Overstretching B-DNA: The elastic response of individual double-stranded and single-stranded DNA molecules. Science 271, 795-799, doi:DOI 10.1126/science.271.5250.795 (1996).

166 Tang, W. et al. Post-transcriptional gene silencing induced by short interfering RNAs in cultured transgenic plant cells. Genomics Proteomics Bioinformatics 2, 97-108 (2004).

167 Demirer, G. S. et al. Carbon Nanocarriers Deliver siRNA to Intact Plant Cells for Efficient Gene Knockdown. bioRxiv, 564427, doi:10.1101/564427 (2019).

168 Li, J., Fan, C., Pei, H., Shi, J. & Huang, Q. Smart Drug Delivery Nanocarriers with Self-Assembled DNA Nanostructures. Advanced Materials 25, 4386-4396, doi:doi:10.1002/adma.201300875 (2013).

169 Li, J., Fan, C., Pei, H., Shi, J. & Huang, Q. Smart drug delivery nanocarriers with self-assembled DNA nanostructures. Advanced materials 25, 4386-4396 (2013).

170 Pérez-de-Luque, A. Interaction of Nanomaterials with Plants: What Do We Need for Real Applications in Agriculture? Frontiers in Environmental Science 5, doi:10.3389/fenvs.2017.00012 (2017).

171 Ali, I., Husnain, T. & Riazuddin, S. RNA interference: the story of gene silencing in plants and humans. Biotechnol Adv 26, 202-209 (2008).

172 Molnar, A., Melnyk, C. & Baulcombe, D. C. Silencing signals in plants: a long journey for small RNAs. Genome Biol 12, doi:ARTN 215 10.1186/gb-2011-12-1-215 (2011).